

Gas and Dust in Molecular Clouds: Density, Temperature and Velocity Structure

A dissertation presented

by

Scott Lawrence Schnee

to

The Department of Astronomy

in partial fulfillment of the requirements

for the degree of

Doctor of Philosophy

in the subject of

Astronomy

Harvard University

Cambridge, Massachusetts

July 2006

© 2006 — Scott Lawrence Schnee

All rights reserved.

Gas and Dust in Molecular Clouds: Density, Temperature and Velocity Structure

Dissertation Advisor: Professor Alyssa Goodman

Scott Lawrence Schnee

Abstract

We have optimized a method for deriving the line-of-sight averaged dust temperature and column density by combining 60 and 100 μm IRAS emission maps and near-infrared extinction maps. We apply this method to map tens of square degrees of the Perseus, Ophiuchus and Serpens molecular clouds. These maps are some of the first results from the ongoing COordinated Molecular Probe Line Extinction and Thermal Emission Survey of Star-Forming Regions. While the emission-derived extinctions are globally accurate, we warn that they are not accurate on scales of $\sim 5'$. Based on our analysis of a simulation of a turbulent molecular cloud similar to Perseus and Ophiuchus, we show that most of the point-to-point scatter in emission vs absorption-derived column density can be attributed to the flawed assumption of isothermal dust along each line of sight in Perseus. In Ophiuchus there is additional scatter above that which can be explained by the isothermal assumption alone. Our results imply that variations in dust emission properties within a molecular cloud are not necessarily a major source of uncertainty in column density measurements. We demonstrate that longer wavelength emission maps are less biased than maps made toward the peak of the dust emission spectrum.

Using data at 450, 850 and 1200 μm , we map the dust temperature and column density of the starless core TMC-1C. From these data we derive a density profile that is generally consistent with that of a Bonnor-Ebert sphere, and a temperature profile that is consistent with that expected of an externally heated core. In addition, we are able to constrain the emissivity spectral index of the dust in TMC-1C. We analyze the effects of noise and calibration uncertainties on the derived properties from sets of three and four emission maps.

We have observed TMC-1C in a variety of high and low density tracers with the IRAM 30m telescope and constructed gas column density maps. Every molecular species shows evidence of depletion, and the linewidths are roughly constant, consistent with it being a coherent core. The velocity field is ordered, but is inconsistent with previous claims of rotation.

Contents

Abstract	iii
Acknowledgments	ix
Dedication	x
1 Introduction	1
2 COMPLETE Dust Emission Maps	7
2.1 Introduction	8
2.2 Data and Calibration	9
2.2.1 IRAS/IRIS	9
2.2.2 Optical and NIR Extinction Maps	9
2.3 Basic Formulae	12
2.4 Derivation Of Constants	13
2.5 Results and Discussion	14
2.5.1 Assumption of Thermal Equilibrium	14
2.5.2 Assumption of Uniform Dust Properties	15
2.5.3 Temperature and Column Density Maps	15
2.5.4 Temperature and Extinction Distributions	16
2.5.5 Emissivity Spectral Index	25
2.6 Summary	26
3 Column Density in Molecular Clouds	29

3.1	Introduction	30
3.2	The Model Cloud	30
3.2.1	Density Structure	31
3.2.2	Radiative transfer	31
3.2.3	Dust properties	31
3.3	Derived Color Temperature and Column Density	32
3.4	Results	33
3.4.1	Dependence on Wavelength	33
3.4.2	Variable Dust Properties	37
3.4.3	Emission from Very Small Grains	37
3.4.4	Comparison with Observations	40
3.5	Summary	41
4	TMC-1C Seen at 450 and 850 Microns	43
4.1	Introduction	44
4.2	Observations	45
4.2.1	Continuum	45
4.2.2	Spectral Line	45
4.3	Dust Properties	48
4.3.1	Assumed Parameters	48
4.3.2	Derivation of Temperature	48
4.3.3	Calculation of Extinction	49
4.3.4	Derivation of the Emissivity Spectral Index	51
4.3.5	Calculation of Mass	51
4.3.6	Temperature and Density Profiles	54
4.4	Virial Mass and Infall	60
4.4.1	Calculation of the Virial Mass	60

4.4.2	N_2H^+ Self-Absorption	65
4.5	Discussion	67
4.5.1	450 and 850 μm Emission Maps	67
4.5.2	Temperature Distribution	67
4.5.3	Dependence on β	67
4.5.4	Dust Emissivity	68
4.5.5	Emissivity Spectral Index	68
4.5.6	Mass Estimates With and Without Maps at Multiple Wavelengths	69
4.5.7	Observed and Model Profiles	71
4.6	Summary	75
4.6.1	450 and 850 μm data	75
4.6.2	Low Temperature	75
4.6.3	High Mass	75
4.6.4	The Effect of Varying Beta	76
4.6.5	Infall Motions Detected	76
4.6.6	Star Formation Model	76
5	TMC-1C Seen at 450, 850 and 1200 Microns	79
5.1	Introduction	80
5.2	Observations	80
5.2.1	SCUBA	80
5.2.2	MAMBO	81
5.3	Solving for physical parameters	82
5.4	Error Analysis	83
5.4.1	Illustrative Examples	84
5.4.2	Deriving the Physical Parameters	84
5.4.3	Fixing One Parameter	87

5.4.4	A Model Core	91
5.5	Dust Emission in TMC-1C	93
5.5.1	Morphology	93
5.5.2	Derived Parameters	93
5.5.3	Comparison With Previous Results	95
5.6	Summary	97
6	Chemistry and Velocity Gradients in TMC-1C	101
6.1	Introduction	101
6.2	Observations	102
6.2.1	Continuum	102
6.2.2	Spectral Line	103
6.3	Results and Analysis	103
6.3.1	Column Densities	103
6.3.2	Molecular Depletion	107
6.3.3	Line Widths	114
6.3.4	Velocity Gradients	116
6.4	Summary	120
7	Conclusions	123
7.1	Summary	123
7.2	Future Work	126
	References	127

Acknowledgments

I would like to thank my advisor, Alyssa Goodman, for all of the help that she has given me throughout my time in graduate school. Alyssa convinced me to come to Harvard, supported me academically and emotionally during my time here, and worked hard to help me in my job search. I am forever indebted to her.

The combined efforts of my collaborators and members of the COMPLETE team have made the work in this thesis possible. In this regard Tom Bethell, Jens Kauffmann and Naomi Ridge deserve special recognition. Paola Caselli has been a co-advisor to me for the past year and our resident expert astrochemist; her presence in Cambridge this year has been invaluable.

There are many scientists that have provided necessary encouragement and expertise along the way. I owe many thanks to David Helfand and Jacqueline van Gorkom for guiding me along the proper path in college and showing me what it means to be an astronomer. Phil Myers has always found time for me when I needed help with projects and proposals. My thesis and research exam committee members have provided direction and constructive criticism to my research, and I thank them for their assistance.

The Harvard astronomy graduate students have provided me with friendship, support and scientific discussion. I couldn't have hoped for a better group to work with, and I am thankful for having gotten the chance to know them. In particular, I would like to recognize Steve Furlanetto, Jenny Greene, Dan Marrone, Eliza Miller-Ricci, Brant Robertson, and Peter Sollins for keeping me sane and in good spirits during my six years at Harvard.

My roommates have provided me with the perfect environment to balance work and fun. Becca Eyre, Derek Greenfield, David Gude, Aly Shamji and Chris Wagner have ensured that I have looked forward to each day.

Finally, I want to thank my parents and brother for their unending confidence and love. I wouldn't be the person that I am today without my family.

– SLS

Dedicated to Joanne, Robert and Steven Schnee

Chapter 1

Introduction

Although most of the mass in a molecular cloud (MC) is in the form of molecular hydrogen, H_2 is largely invisible under quiescent interstellar conditions. Instead, observations of emission and absorption from dust and rotational lines from molecular species such as CO and its isotopologues are typically used as proxies to determine the properties of molecular clouds. Recent studies have shown that dense ($n > 10^4 \text{ cm}^{-3}$) cores, the immediate precursors to stars, exist preferentially in the small percentage of molecular clouds with high column density, and that cores are strongly clustered (Enoch et al. 2006; Johnstone et al. 2004). In order to understand why dense cores form in certain regions and not others, how long cores can survive without either collapsing or dispersing, and a host of other star formation related issues, astronomers need to be able to determine such basic properties of molecular clouds as the temperature and density distributions and the internal motions of the gas and dust.

Unfortunately, each method of tracing the mass in a molecular cloud is subject to its own set of biases and uncertainties. For instance, the emission from CO and its isotopologues is unsuitable for studying the denser regions within a molecular cloud because the emission is often optically thick and because CO is removed from the gas phase as it sticks to dust grains at temperatures below $\sim 20 \text{ K}$ (Langer et al. 1989). Thus, CO is unable to trace the densest and coldest regions in a MC, which from the perspective of star formation are the most interesting areas to observe. Furthermore, one needs to assume some canonical ratio between the abundance of CO and H_2 , which is uncertain within a factor of ~ 2 (van Dishoeck et al. 1992), and the gas is generally assumed to be in local thermodynamic equilibrium, which depending on the density and cloud structure may not be a valid assumption.

Studies of dust emission and absorption suffer from a different set of systematic

uncertainties, largely because there is significant uncertainty as to what “dust” is composed of. Dust is composed of carbonaceous, silicate, and/or metallic grains (Draine 2003), but the actual mixture and structure are not well established. The shape of grains may be spherical, spheroidal, fractal, or may look like disks or needles (Ossenkopf & Henning 1994). Grains probably vary in size between a few tenths of a nanometer to a few microns (Mathis et al. 1977; Li & Draine 2001). The surfaces of dust grains are likely to be polluted by the depletion of molecules from the gas phase and the formation of icy mantles in cold, dense regions (Ossenkopf & Henning 1994). Each of these dust parameters affect the emissivity/opacity of the dust at all wavelengths, and the ratio of dust to gas is likely to vary between various environments (Burstein & Heiles 1978).

Each observational technique has its advantages. Studying MCs by mapping the CO (or other trace molecules) distribution yields kinematic information in the form of line-of-sight velocities, which dust studies can not reveal. Mapping column density by reddening in the near-infrared or optical star counts is probably the most precise method of determining column density because it is not sensitive to variations in temperature along the line of sight. Maps of continuum emission from dust grains can help determine the temperature structure of MCs, and are able to probe changes in the dust size distribution and exposure to the interstellar radiation field.

Different methods for mapping the temperature and column density of molecular clouds, or portions of them, have been combined by many authors. For instance, Langer et al. (1989) have mapped the dust and gas emission in the Barnard 5 region of Perseus with ^{12}CO , ^{13}CO and C^{18}O emission and continuum emission at the four IRAS bands at 12, 25, 60 and 100 μm . They find that ^{12}CO emission is highly saturated, but the other isotopologues of CO are optically thin, and that the ^{13}CO emission is correlated with the 100 μm opacity. However, they find that the dust emission underestimates the true column density by a factor of 15, which they attribute to the stochastic heating to high temperatures of small dust grains, resulting in higher derived equilibrium dust temperatures and lower column densities.

A similar study using IRAS observations and CO emission from the ρ Oph region was conducted by Jarrett et al. (1989), who make the first attempt to use an extinction map to test the validity of dust emission as a tracer of column density. Their observations conclude that there are at least two populations of dust grains at very different temperatures, and that determinations of dust temperature and column density are complicated by line-of-sight variations in the dust temperature created by limb brightening and embedded sources. Jarrett et al. (1989) find that the column density predicted from dust emission is lower than that expected from

CO emission by a factor of 20, consistent with the results of Langer et al. (1989).

These studies and others led to the conclusion that far-infrared emission comes from a variety of types of dust grains (Desert et al. 1990). Emission below $\sim 15 \mu\text{m}$ can be attributed to PAH molecules and very small dust grains that have highly time variable temperatures. Between ~ 15 and $\sim 100 \mu\text{m}$ the emission comes from a combination of the very small grains and larger dust grains in thermal equilibrium with their surroundings. These big grains are thought to be responsible for all of the emission longward of $100 \mu\text{m}$.

Because the emission from big grains in thermal equilibrium is more likely to trace the mass in molecular clouds than the other grain components, efforts have been made to isolate their contribution to IRAS maps at 60 and $100 \mu\text{m}$ e.g. (Abergel et al. 1994; Cambr sy et al. 2001). Other surveys have simply mapped molecular clouds above $100 \mu\text{m}$, where all of the emission is expected to originate from the big grains, e.g. (Lagache et al. 1998; Schlegel et al. 1998; del Burgo et al. 2003; Dupac et al. 2003). Many of these studies have shown that the big grain emission can be approximated as coming from two temperature components, one a few degrees below 15 K, and the other a few degrees above. Furthermore, they have found that the dust emissivity may differ between the two populations, and that the emissivity spectral index of the dust may be temperature dependent (Dupac et al. 2003).

Maps of starless cores and protostars are typically made with similar techniques to those of molecular clouds, but at higher resolution. A few cores, such as Coalsack 2, B68, B335 and IC 5146, have their column densities determined by near-infrared reddening (Jones et al. 1984; Alves et al. 2001; Harvey et al. 2001; Lada et al. 1999), but many cores have column densities that are too high to measure near-infrared color excesses, or simply do not have sufficient background stars to serve as column density probes. Observations of dust emission from cores are often made between ~ 350 and $\sim 1300 \mu\text{m}$ by bolometer arrays, which have larger bandwidths than heterodyne receivers and have resolution on the order of $10''$. Submillimeter and millimeter surveys of cores often reveal density distributions that flatten towards the core center, and scale approximately as r^{-2} towards the edge of the core, consistent with predictions of ambipolar diffusion and Bonnor-Ebert models, e.g. (Ward-Thompson et al. 1994, 1999; Shirley et al. 2000; Johnstone et al. 2000). However, the conclusions from bolometer maps all make assumptions about the temperature distribution of the core, its three dimensional structure, and the emission properties of dust. None of these parameters is necessarily well-constrained by observations at one, two or even three wavelengths (see Chapter 5).

The interpretation of spectral line maps of starless cores is complicated by the intricate chemistry that takes place at the high densities and low temperatures present in the centers of these objects. Although CO is the most abundant trace molecule in the ISM, it is nearly absent from the interiors of starless cores because of freeze-out onto the surfaces of dust grains, e.g. (Kramer et al. 1999; Caselli et al. 1999; Tafalla et al. 2004). Other molecules such as N_2H^+ and NH_3 are destroyed by CO, and therefore only exist in those regions where the CO is removed from the gas phase. Spectral line maps of both high and low density tracers, used together, are thus able to reveal information about the interiors and envelopes of starless cores. Surveys of cores using spectral line maps have shown that there is significant non-thermal motions, often attributed to turbulence, and that magnetic fields may play a critical role in cloud support (Myers & Goodman 1988a,b). The line width within a core is roughly constant with radius at a value lower than that of the cloud in which it resides, and in this sense many cores are “coherent” (Barranco & Goodman 1998; Goodman et al. 1998). Many cores are seen to have velocity gradients indicating possible rotation, but this rotational energy is insufficient to be an important support mechanism against gravitational collapse (Goodman et al. 1993). Nevertheless, the rotation is important in determining the fragmentation of the core during its possible future collapse phase (Boss & Myhill 1995; di G. Sigalotti & Klapp 1996). In addition, some starless cores are seen to have the signature of infall, though this infall is generally sub-sonic and not a true free-fall collapse (Tafalla et al. 1998; Lee et al. 1999, 2001, 2004).

One goal of the COMPLETE (COordinated Molecular Probe Line Extinction and Thermal Emission) Survey of Star Forming Regions is to provide a multiwavelength database covering tens of square degrees of molecular clouds that will allow astronomers to combine the advantages of each method for determining the global properties of MCs. COMPLETE has mapped the Perseus and Ophiuchus molecular clouds in ^{12}CO (1-0) and ^{13}CO (1-0), made column density and dust temperature maps from 60 and 100 μm IRAS data, and constructed extinction maps from the near-infrared colors of stars behind the MCs (Ridge et al. 2006b). On the scale of a single dense core, in TMC-1C we have made dust continuum maps of the central $10' \times 10'$ at 450, 850 and 1200 μm , as well as spectral line maps from a variety of high and low density molecular tracers. By combining these datasets in this thesis, I have been able to use the strengths of each data type to learn about the physical state of dense cores and molecular clouds, while also demonstrating the limitations of each method and how to minimize the effects of the limitations.

In Chapter 2, we describe an optimized method for deriving the dust temperature (T_d) and column density (N_H) from IRAS emission maps and optical

and near-infrared extinction maps. We show that the $60\ \mu\text{m}$ flux comes from at least two sources, large grains in thermal equilibrium and very small grains that are stochastically heated. If the very small grain population is ignored, then the equilibrium dust temperatures are systematically overestimated and the column density predicted from dust emission will be underestimated. Furthermore, the conversion between $100\ \mu\text{m}$ optical depth and extinction varies globally between the Perseus, Ophiuchus and Serpens molecular clouds and, to a lesser extent, within different portions of one molecular cloud, suggesting that the emissivity and opacity of dust is not constant between regions. Although on the scale of an entire molecular cloud the column density distribution predicted from dust emission can be brought into agreement with the extinction-derived column density, on a point by point basis the scatter between the two methods is several tens of percent.

In Chapter 3, we simulate an externally heated molecular cloud and compare the column density derived from pairs of emission maps to the true column density in order to isolate the effect of assuming that all of the dust along each line of sight through a MC is isothermal. We show that the column density derived from longer ($> 100\ \mu\text{m}$) wavelength emission maps is less compromised by the isothermal assumption than the column density derived from maps at shorter wavelengths, which systematically overestimate T_d and underestimate N_H in regions of higher true column density. The magnitude of the scatter between the emission-derived column and the true column in the simulation is equal to the scatter observed in Perseus between the IRAS-derived N_H and the extinction-based N_H , which suggests that variations in dust emission and absorption properties are not the dominant source of error in our COMPLETE column density estimates.

In Chapter 4, we use dust continuum maps at 450 and $850\ \mu\text{m}$ to make column density and dust temperature maps of the starless core TMC-1C. We show that the temperature of the core is lower than is often assumed for similar cores, and as a result, the mass that we derive for TMC-1C is larger than would have been predicted had we only made observations at one wavelength. We use self-absorbed $\text{N}_2\text{H}^+(1-0)$ lines to derive a sub-sonic infall velocity in TMC-1C and a virial mass that is significantly smaller than the dust-derived mass. By comparing the infall velocity and density profiles of TMC-1C to those predicted by several popular star-formation models, we show that a contracting Bonnor-Ebert sphere is the best-fit analytic model.

In Chapter 5, we use dust continuum maps at 450 , 850 and $1200\ \mu\text{m}$ to map the column density and dust temperature and derive a constant value for the dust emissivity spectral index in the starless core TMC-1C. We run Monte Carlo simulations to show the effect of uncertainties on the derived T_d and N_H when using

three maps at different wavelengths to fit the two parameters, and show that by observing a fourth emission map at a different wavelength, even with substantial noise and calibration uncertainties, should finally allow the practical derivation of accurate maps of T_d , N_H and β . At signal to noise levels currently achievable, maps at three wavelengths are not sufficient to estimate these three parameters accurately.

In Chapter 6, we use the dust emission maps from Chapter 5 along with IRAM 30m observations of several high and low density tracers to study the physical state of TMC-1C. We show that every molecule, to some degree, shows evidence of depletion, though the isotopologues of CO and CS are more strongly affected than N_2H^+ . The linewidths of CO are significantly higher than those seen in N_2H^+ suggesting that CO probes a different region of the core than does N_2H^+ , which presumably exists in a more quiescent and colder inner region of TMC-1C. We show that although the velocity field in TMC-1C is ordered and structured, it does not show the signature of solid body or differential rotation.

Finally, in Chapter 7, I present my conclusions and some promising directions for future research, including additional numerical simulations and observations with future instruments and telescopes.

Chapter 2

A COMPLETE Look at the Use of IRAS Emission Maps to Estimate Extinction and Dust Temperature

Scott Schnee, Naomi Ridge, Alyssa Goodman & Jason Li
The Astrophysical Journal, Volume 634, Issue 1, pp. 442-450

Abstract

We have created new dust temperature and column density maps of Perseus, Ophiuchus and Serpens using 60 and 100 μm data from the IRIS recalibration of IRAS data. We describe an optimized method for finding the dust temperature, emissivity spectral index, and optical depth using optical and NIR extinction maps. The creation of these temperature and extinction maps (covering tens of square degrees of molecular clouds) is one of the first results from the ongoing COordinated Molecular Probe Line Extinction Thermal Emission (COMPLETE) Survey of Star Forming regions. However, while the extinctions derived from the IRIS emission maps are globally accurate, we warn that FIR emission is not a good proxy for extinction on the scale of one pixel ($\sim 5'$).

In addition to describing the global dust properties of these clouds, we have found two particularly interesting features in the column density and temperature maps. In the Ophiuchus dark cloud complex, the new dust temperature map shows a little known warm (25 K) dust ring with 2 pc diameter. This shell is approximately centered on the B star ρ -Ophiuchus, 1° north of the well-studied ρ -Oph star-forming

cluster. In Perseus, the column density map shows a 10 pc diameter ring, a feature not apparent in the filamentary chain of clouds seen in molecular gas. These rings are further discussed in detail in companion papers to this one.

2.1 Introduction

The goal of the COMPLETE Survey is to use a carefully chosen set of observing techniques to fully sample the density, temperature and velocity structure of three of the five large star-forming complexes observed in the NASA-sponsored Spitzer Legacy Survey “From Molecular Cores to Planet-forming Disks” (c2d) described in Evans et al. (2003).

The c2d Survey, started in late 2003, is producing high-resolution infrared spectroscopy, and near- through far-infrared images of each of its 5 pc scale target complexes. COMPLETE is providing fully-sampled millimeter spectral-line, extinction, and thermal emission maps for the same regions, at arcminute resolution or better (Goodman 2004; Ridge et al. 2006b). Phase II of COMPLETE, begun recently, provides higher-resolution observations using the same suite of techniques for a large subset of the high-density cores evident at lower resolution.

In this paper we present new temperature and extinction maps of the Perseus, Serpens and Ophiuchus star-forming regions, produced from 60 and 100 μm flux-density maps obtained from IRIS (Improved Reprocessing of the *IRAS* Survey), and normalized using optical/NIR extinction maps Ridge et al. (2006b); Cambr  sy (1999). Previous all-sky thermal dust emission maps by Schlegel et al. (1998) [SFD] include these regions. However, the SFD maps were based on low-resolution temperature data and optimized for low extinction regions. It has been established that the SFD maps lose accuracy at $A_V > 0.5 \text{ mag}$ (Arce & Goodman 1999a; Cambr  sy et al. 2005), so they are not adequate for mapping column density in the high-extinction areas targeted in the COMPLETE survey. We show here that reanalysis of the IRAS data can yield column density and color temperature maps that are more accurate at high and low levels of extinction on the large scale, though their use on the scale of the data ($\sim 5'$) is more limited.

In Section 2.2 we describe the IRIS flux measurements and NIR/optical-based extinction maps. In Sections 2.3 and 2.4 we present and explain the equations used to determine the dust optical depth and conversion to visual extinction, and the parameters needed in those equations. In Section 2.5 we compare the results of our analysis technique to those from other extinction tracers. The results are

summarized in Section 2.6.

2.2 Data and Calibration

2.2.1 IRAS/IRIS

IRIS¹ images of flux-density at 60 and 100 μm were obtained for each of our three target regions from the IRIS website (Miville-Deschênes & Lagache 2005). Image details are given in Table 2.1. The maps have units of MJy sr^{-1} , are made with gnomonic projection and have spatial resolution smoothed to $4.3'$ at 100 μm .

IRIS data offer excellent correction for the effects of zodiacal dust and striping in the images and also provide improved gain and offset calibration. Earlier releases of the IRAS data did not have the appropriate zero point calibration, which can have serious consequences on the derived dust temperature and column density (Arce & Goodman 1999b). To test the zero point calibration of the IRIS data, we allowed two free parameters in the fit (one each for the 60 and 100 micron zero points) to convert IRIS fluxes to visual extinction (see Section 2.4). We find that values of the free parameters are consistent with zero, and thus provide independent evidence that the zero point calibrations of the IRIS data at 60 and 100 μm are correct.

2.2.2 Optical and NIR Extinction Maps

Here we describe the NIR and optical extinction maps used to recalibrate the IRIS maps presented in this paper. We have obtained extinction maps of Serpens and Ophiuchus from Cambr sy (1999), which are based on an optical star counting method with variable resolution (but we regrid these maps to the constant resolution of the IRIS images). The optical photometry data used by Cambr sy come from the USNO-PMM catalogue (Monet 1996). Extinction maps of Perseus and Ophiuchus have been constructed from the 2MASS point source catalog as part of COMPLETE (Ridge et al. 2006b) using the “NICER” algorithm, which is a revised version of the NICE method described in Lada et al. (1994) and Lombardi & Alves (2001). NICE and NICER combine direct measurements of near-infrared color excess and certain techniques of star counting to derive mean extinctions and map the dust

¹IRIS comprises a machine-readable atlas of the sky in the four IRAS bands at 12, 25, 60, and 100 μm

column density distribution through a cloud (Lombardi & Alves 2001). The 2MASS survey provides the NIR J , H and K_s colors of background stars that have been reddened by the molecular cloud. With these measured colors, and knowledge of the intrinsic colors of these stars (measured in a nearby, non-reddened control field), the amount of obscuring material along the line of sight to each star can be determined. In NICER, the extinction values are calculated for a fixed resolution, which means uncertainties vary from pixel to pixel. Maps of uncertainty for the regions considered are shown in Ridge et al. (2006b).

In the Ophiuchus molecular cloud, we have both 2MASS/NICER and optical star counting based extinction maps. It is important to note that the two methods *do not* give equivalent extinctions. A plot of the optical vs NIR extinctions is shown in Figure 2.1. A linear fit to the data shows that the slope of the line relating the two quantities is very close to unity (as expected), *but* there is an offset of roughly 0.71 magnitudes of visual extinction, with the 2MASS derived data points being systematically higher than the optically derived extinctions. The 1σ scatter on the least squares fit between the two methods is 0.7 magnitudes in A_V . Because these methods produce such different results, care must be taken when using any one extinction map as a model to determine dust properties as described in Section 2.3. In Ophiuchus, where we have both optical and NIR extinction maps, we run the global fitting algorithm for each data set separately, and report both sets of results in Table 2.2.

In Perseus we only have a NIR based extinction map, and in Serpens we only have an optically derived extinction map, so no intercomparison of the calibration methods is possible for these clouds. We expect that the 2MASS derived extinctions are more accurate than the star counting method of Cambr  sy, although in both cases the zero point calibration can be difficult to assess. The optical star counting method chooses the average minimum value in the map as the “zero level” of extinction (Cambr  sy 1999), and the NICER method uses the average minimum H-K color to determine the minimum extinction in the map. Both methods rely on the minimum in their map actually corresponding to zero extinction, which if untrue, will cause both methods to underestimate the true extinction. In Ophiuchus, because the NICER algorithm gives higher extinctions, it is likely that the optical star counting algorithm has underestimated the true extinction by approximately 0.71 magnitudes. Our decision to trust the NIR based extinctions over the star counting extinctions is supported by discussion with Drs. Cambr  sy and Alves (private communication). To account for the 0.71 mag offset, we have added 0.71 magnitudes to the extinction values derived by Cambr  sy (1999) in our optically calibrated calculations for Ophiuchus in Sections 2.3 and 2.4.

Table 2.1. IRIS Image Details

Region	Center RA (degrees)	Center Dec (degrees)	Image Size (degrees)
Perseus	54.30	31.85	6.6×4.5
Perseus Ring	54.91	31.87	1.8×1.8
B5	56.90	32.85	0.8×0.8
IC348	55.94	31.99	1.0×1.0
NGC1333	52.16	31.35	1.0×1.0
Ophiuchus	247.95	-24.00	6.9×6.8
Serpens	277.00	0.50	3.0×3.0

Note. — All positions are given in equatorial J2000 equinox coordinates.

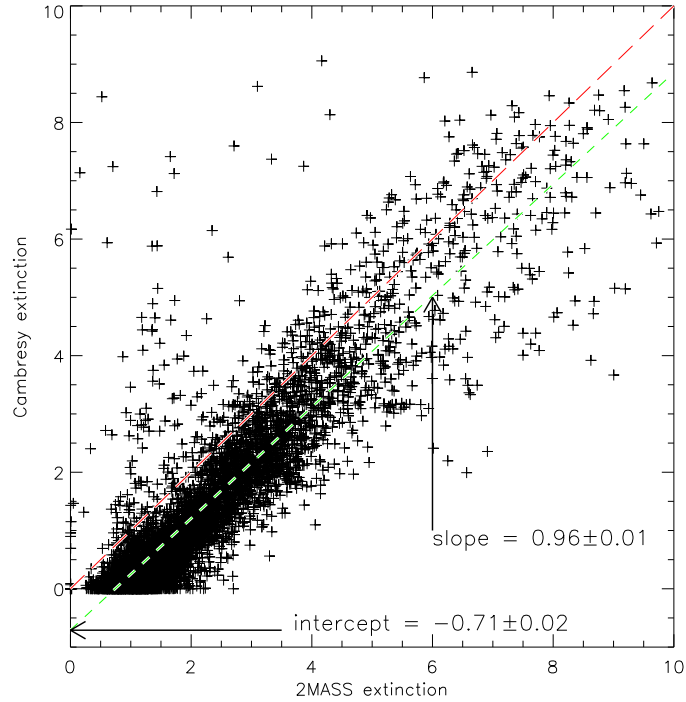


Figure 2.1.— Scatter plot of the Ophiuchus optical star counting (Cambresy 1999) and NIR color excess method (Ridge et al. 2006b) extinctions in Ophiuchus. The green line (short dashes) is the best fit line to the data sets, with the equation shown at bottom of the image. The red (1:1) line (long dashes) is there only to guide the eye. Nearly 60 percent of the data points have 2MASS extinctions less than 2 magnitudes.

We expect the Serpens extinction map to suffer from the same “zero level” problem as the Ophiuchus optical extinction map, and therefore include a free parameter in the fit between the optical extinction map and the IRIS emission maps to account for this possibility. We find the best fit occurs between the emission based extinction map and the optical star count based extinction map when the latter map has a constant value of 2.4 magnitudes of visual extinction added to each pixel.

2.3 Basic Formulae

The basic method that we use to calculate the dust color temperature and column density from the IRAS 60 and 100 μm flux densities is similar to Wood et al. (1994) and Arce & Goodman (1999b). The temperature is determined by the ratio of the 60 and 100 μm flux densities. The column density of dust can be derived from either measured flux and the derived color temperature of the dust. The calculation of temperature and column density depend on the values of three parameters: two constants that determine the emissivity spectral index, and the conversion from 100 μm optical depth to visual extinction. We are able to solve for these parameters explicitly because we have an independent estimate of visual extinction, as will be explained in Section 2.4.

The dust temperature T_d in each pixel of a FIR image can be obtained by assuming that the dust in a single beam is isothermal and that the observed ratio of 60 to 100 μm emission is due to blackbody radiation from dust grains at T_d , modified by a power-law emissivity spectral index. The flux density of emission at a wavelength λ_i , is given by

$$F_i = \left[\frac{2hc}{\lambda_i^3 (e^{hc/(\lambda_i k T_d)} - 1)} \right] N_d \alpha \lambda_i^{-\beta} \Omega_i, \quad (2.1)$$

where N_d represents column density of dust grains, α is a constant that relates the flux to the optical depth of the dust, β is the emissivity spectral index, and Ω_i is the solid angle subtended at λ_i by the detector.

Following Dupac et al. (2003), we use the equation,

$$\beta = \frac{1}{\delta + \omega T_d} \quad (2.2)$$

to describe the observed inverse relationship between temperature and the emissivity spectral index. The parameters (δ and ω) are derived separately for each cloud and subregion considered in this paper.

With the assumptions that the dust emission is optically thin at 60 and 100 μm and that $\Omega_{60} \simeq \Omega_{100}$ (true for IRIS images), we can write the ratio, R , of the flux densities at 60 and 100 μm as

$$R = 0.6^{-(3+\beta)} \frac{e^{144/T_d} - 1}{e^{240/T_d} - 1}. \quad (2.3)$$

Once the appropriate value of β is known, one can use Equation 2.3 to derive T_d . The value of β depends on such dust grain properties as composition, size, and compactness. For reference, a pure blackbody would have $\beta = 0$, amorphous layerlattice matter has $\beta \sim 1$, and metals and crystalline dielectrics have $\beta \sim 2$.

Once the dust temperature has been determined, the 100 μm dust optical depth can be calculated as follows:

$$\tau_{100} = \frac{F_\lambda(100\mu\text{m})}{B_\lambda(100\mu\text{m}, T_d)}, \quad (2.4)$$

where B_λ is the Planck function and $F_\lambda(100\mu\text{m})$ is the 100 μm flux.

The 100 μm optical depth can then be converted to V-band extinction using:

$$A_V = X\tau_{100} \quad (2.5)$$

where X is a parameter relating the thermal emission properties of dust to its optical absorption qualities.

2.4 Derivation Of Constants

We can derive the values of the three parameters (δ , ω and X) from the IRIS emission maps and extinction maps from Cambr sy (1999) and Ridge et al. (2006b). Each optical and NIR extinction map described in Section 2.2.2 is used as a “model” extinction map to fit the IRIS-implied column density map using the three adjustable parameters which are explained in Section 2.3. The IDL task AMOEBA was used to simultaneously fit all three parameters with the downhill simplex method of Nelder & Mead (1965). Each combination of these three parameters is used to determine the dust temperature and column density at each point in the map (using the formulae in Section 2.3). The parameter values determined by this method are those that create a FIR-based extinction map that best matches the NIR color excess or optical star count derived extinction map. This is a statistical point-by-point match, not a spatial match to features in the NIR/optical extinction map. As explained in

Section 2.2.2, we solve for a fourth parameter in Serpens, which is the zero level of the optical extinction map.

Each cloud is considered separately, so the values of δ , ω and X are different for each cloud. Because Ophiuchus has two independent extinction maps, one from optical star counting (adjusted by the 0.71 mag offset) and one from the NIR color excess method, it has two sets of constants derived for it. In this paper we assume that the values of the three parameters are constant within each image, though of course this does not have to be the case. For instance, it may be the case that areas of especially high or low column density do not share the same visual extinction conversion factor, X . Our values for the three parameters for each region fit (four in Serpens) are presented in Table 2.2.

2.5 Results and Discussion

2.5.1 Assumption of Thermal Equilibrium

The derivations of dust temperature and column density from IRIS data rely on the assumption that the dust along each line of sight is in thermal equilibrium. However, the dust models of Desert et al. (1990) show that the emission at 60 and 100 μm have contributions by big dust grains (BGs) and very small dust grains (VSGs). The VSGs are not in thermal equilibrium, and emit mostly in the 60 micron band, while the BGs are the primary contributors at 100 microns and longer. Because of the emission from the VSGs, determining the temperature of the dust from the ratio of 60 and 100 μm fluxes can yield temperatures that are systematically high. An empirical method for determining the color temperature and optical depth of dust using the 60 and 100 micron bands from IRAS is presented in Nagata et al. (2002), but as this method has been calibrated for galaxies and not molecular clouds, we do not employ their method.

In order to remove the contribution of VSGs to the 60 μm flux, we calibrate our temperature maps to those derived by Schlegel et al. (1998) [SFD], which are not corrupted by VSG emission because they used maps at 100 μm and longer to derive their temperatures. We smooth the IRIS images to the resolution of the SFD temperature maps, and calculate the temperature based on 100% of the 100 μm flux and a lesser percentage of the 60 μm flux, assuming that $\beta = 2$ (as assumed by SFD). The fraction of the 60 μm flux was chosen so as to best match our derived temperatures with the SFD temperatures. The remaining 60 μm flux comes from the VSGs. Note that the temperatures we use in our calculations of column density

do not assume that $\beta = 2$; we use the temperature dependent form of β described in Section 2.3. However, the 60 μm flux used in Section 2.3 is adjusted by this determination. By comparison to the SFD temperature maps, we find that the average VSG contribution to the 60 μm flux is 74%, 72% and 85% in Perseus, Ophiuchus and Serpens, respectively.

2.5.2 Assumption of Uniform Dust Properties

The equations in this paper rely on the assumption that the dust along each line of sight is characterized by a single temperature, emissivity spectral index and emissivity. This is a simplification that our method requires, though we recognize that real molecular clouds are much more complicated.

In their FIR study of interstellar cold dust in the galaxy, Lagache et al. (1998) have found that there are at least two temperature components to the dust population. They find that the warmer component, associated with diffuse dust, has a temperature around 17.5 K, while the colder component, associated with dense regions in the ISM, has a temperature around 15 K. The molecular clouds we study here are expected to have a range of temperatures along some lines of sight that is even wider than seen in Lagache et al. (1998) because the FIRAS data used in this study has a beam size of 7° , which is larger than the size of the maps for each cloud studied in this paper. The color temperature that we derive from our isothermal assumption is therefore biased, as is the optical depth. This problem is especially relevant in Serpens, which is only a few degrees above the galactic center, so there are certainly multiple environments integrated into each IRAS beam. A method for determining the amount of 100 μm flux associated with the cold component of the BGs in a molecular cloud is explained in Abergel et al. (1994), Boulanger et al. (1998) and Laureijs et al. (1991). Nevertheless, Jarrett et al. (1989) find in Ophiuchus that there is a very tight linear correlation between FIR optical depth (determined in much the same way as presented here) and visual extinction for $A_V \leq 5$, so we trust that the errors introduced by our method are not prohibitively large.

2.5.3 Temperature and Column Density Maps

The dust color temperature and column density maps derived from our parameter fits and IRIS data are among the first publicly available data products distributed by the COMPLETE team. Temperature and extinction maps of Perseus, Ophiuchus

and Serpens derived from the IRIS data are shown in Figures 2.2, 2.3 and 2.4. FITS files of these maps can be downloaded from the COMPLETE web page².

In Perseus, there is a striking ring of emission that is centered on a region of warm material. This ring has been discussed by Andersson et al. (2000), Pauls & Schwartz (1989) and Fiedler et al. (1994) and is discussed in more detail in a companion paper to this one (Ridge et al. 2006a). The Perseus ring does not stand out in the NICER extinction map as visibly as in the IRIS column density map because it is not a true column density feature. It is difficult to determine from emission maps alone if individual features are the result of changing dust properties or column density enhancements.

A warm dust ring is evident in Ophiuchus in the temperature map, centered at the position 16:25:35, -23:26:50 (J2000). This ring was reported by Bernard et al. (1993) in a discussion of the far-infrared emission from Ophiuchus and Chameleon, but they did not investigate its nature or possible progenitor. The B star ρ -Ophiuchus and a number of X-ray sources are projected to lie within this shell of heated gas. The Ophiuchus ring will be further discussed in a future paper.

2.5.4 Temperature and Extinction Distributions

In Figure 2.5 we show histograms of the dust temperature in Perseus, Serpens, and Ophiuchus. Each distribution peaks near 17 K, and all except Serpens have a spread of several degrees. The dust temperatures that we derive are, to an extent, calibrated with those derived by Schlegel et al. (1998) (see Section 2.5.1).

It has been shown for Taurus by Arce & Goodman (1999b) that using IRAS 60 and 100 μm flux densities to determine dust column density gives results consistent with other methods, such as the color excess method (e.g. NICE/NICER), star counts (e.g. Cambr sy (1999)), and using an optical (V and R) version of the average color excess method used by Lada et al. (1994). Here we compare the IRIS derived extinction maps of Perseus, Serpens, and Ophiuchus with maps created by some of these other methods.

Our method requires the FIR-derived extinction to best match the NIR or optical-derived extinction, and the global agreement can be seen in Figure 2.6. However, the point-to-point extinction values can be significantly different between the two methods, as shown in Figure 2.7. The large scatter in these extinction

²<http://cfa-www.harvard.edu/COMPLETE>

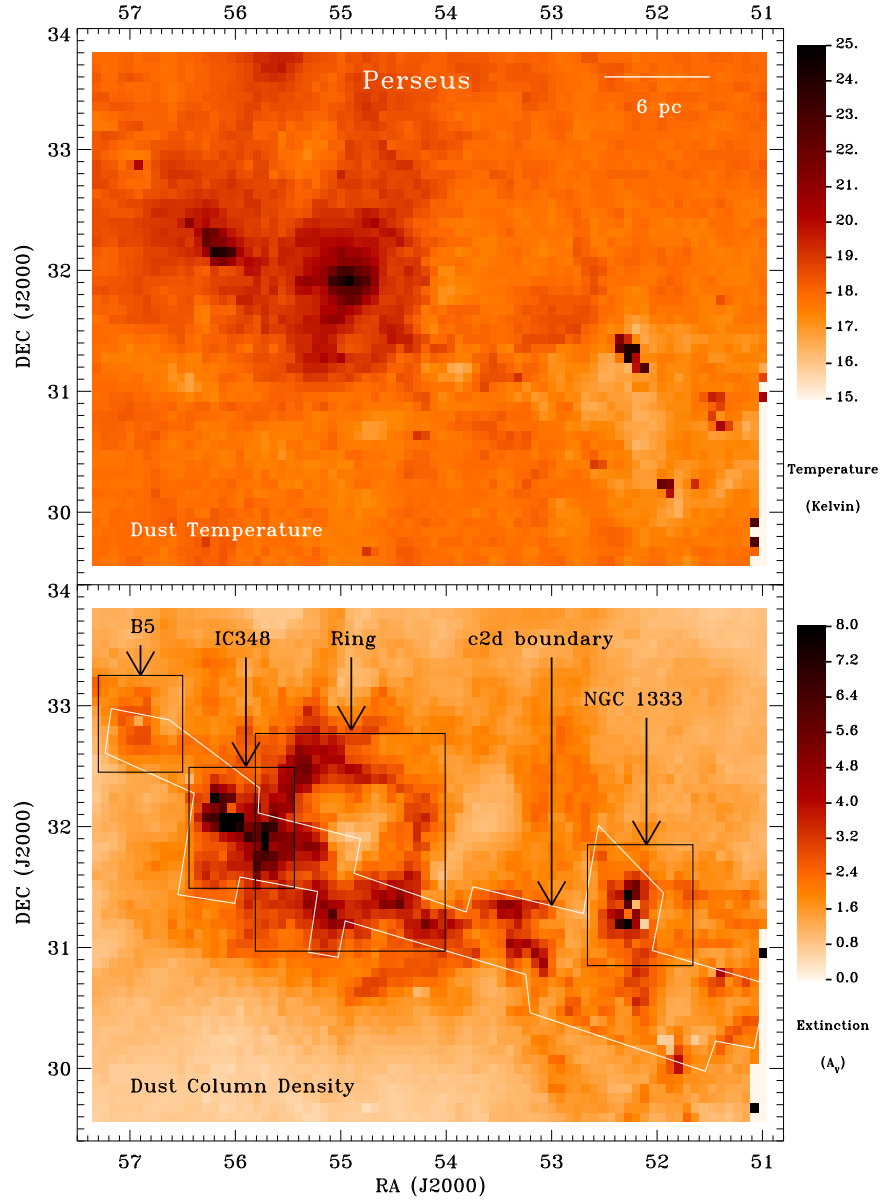


Figure 2.2.— Dust color temperature map (top) and column density map (bottom) of Perseus created from IRIS 60 and 100 μm images. RA and DEC are plotted in decimal degrees.

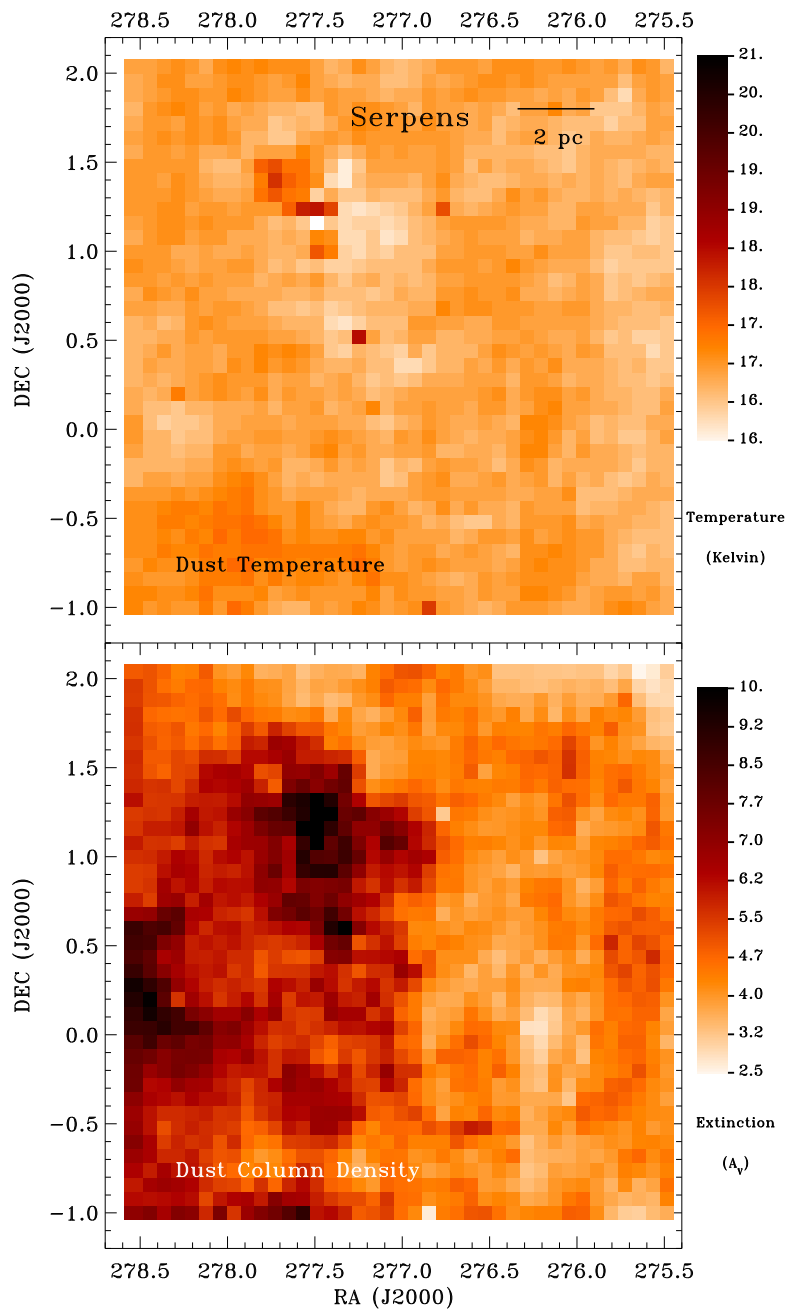


Figure 2.3.— Dust color temperature map (top) and column density map (bottom) of Serpens created from IRIS 60 and 100 μm images.

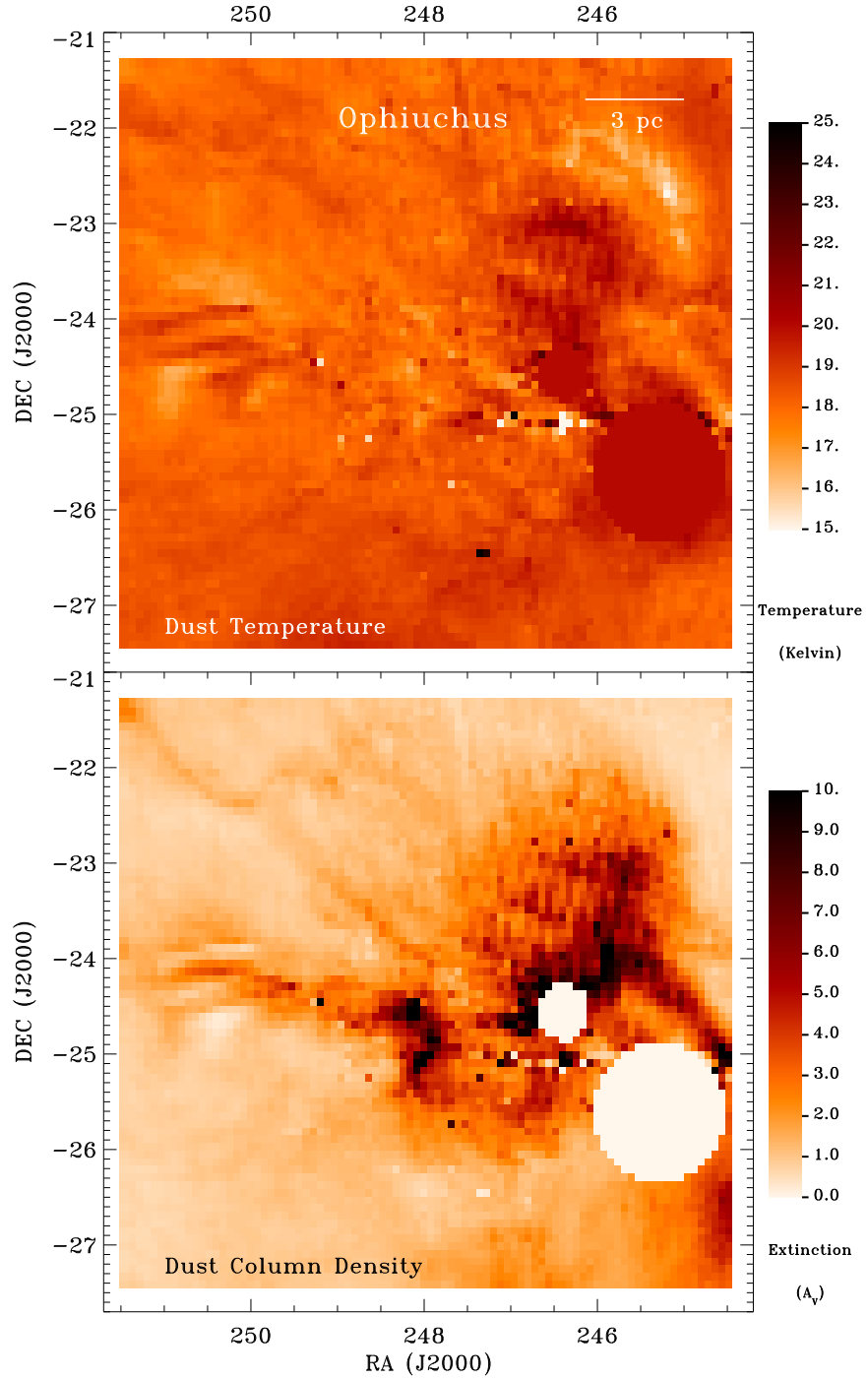


Figure 2.4.— Dust color temperature map (top) and column density map (bottom) of Ophiuchus created from IRIS 60 and 100 μm images. The two white circles have been excluded due to contamination from B stars.

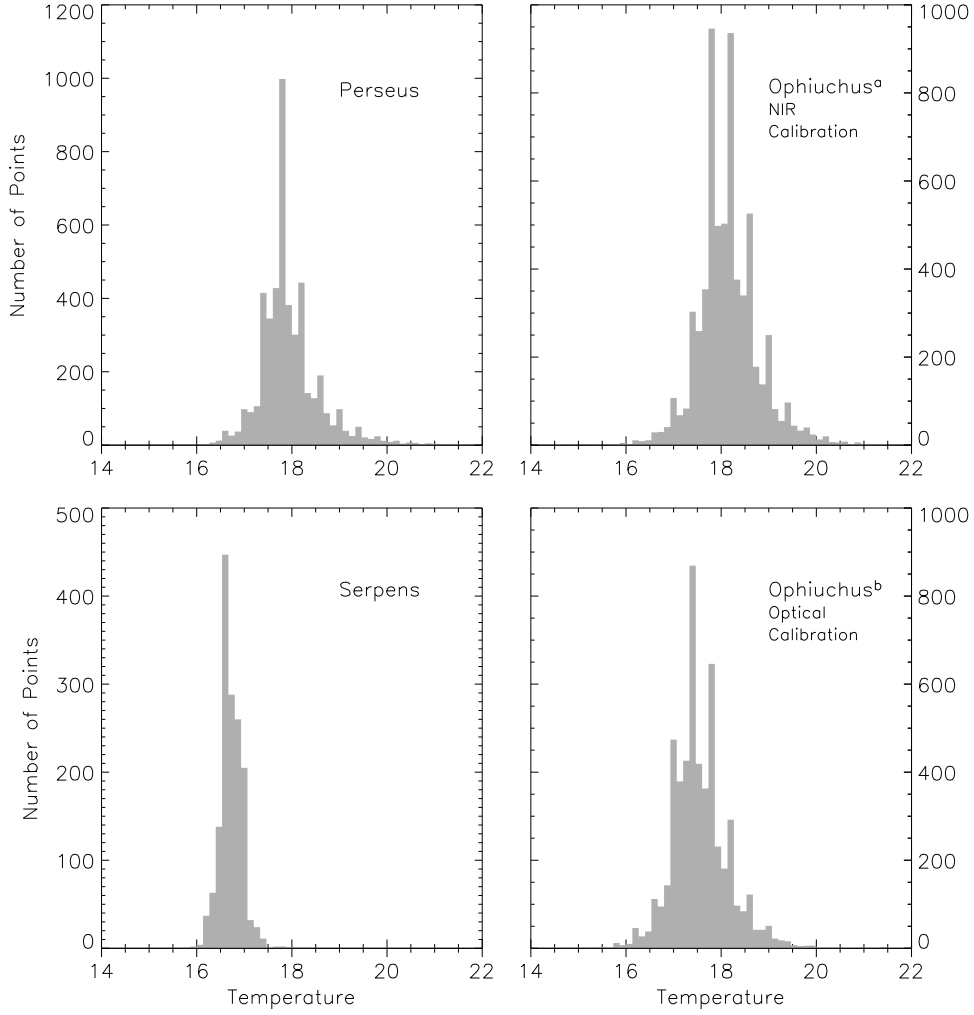


Figure 2.5.— The filled histograms show the temperature derived from the 60/100 μm flux density ratio in Perseus, Serpens and Ophiuchus after the calibration described in Section 2.2. The Ophiuchus^a histogram (top right) is calibrated to the 2MASS extinction map. The Ophiuchus^b histogram (bottom right) is calibrated to the Cambr sy data.

plots ($1\sigma \simeq 1 \text{ mag } A_V$) is likely the result of the various assumptions used in our calculations. For instance, it is unlikely to be the case that all of the dust along a given line of sight can be well characterized by a single temperature or emissivity spectral index, especially along lines of sight through the denser regions of the molecular clouds. It is also likely that the dust optical depth to visual extinction conversion factor (X) is not constant throughout a cloud volume. The flux detected by IRAS comes preferentially from warmer dust, while the extinction maps made from NIR and optical data have no temperature bias, so it is also possible (and in many regions likely) that the dust doing most of the FIR emitting is not the same dust responsible for most of the extinguishing at shorter wavelengths. The scatter for each cloud is shown in Table 2.3.

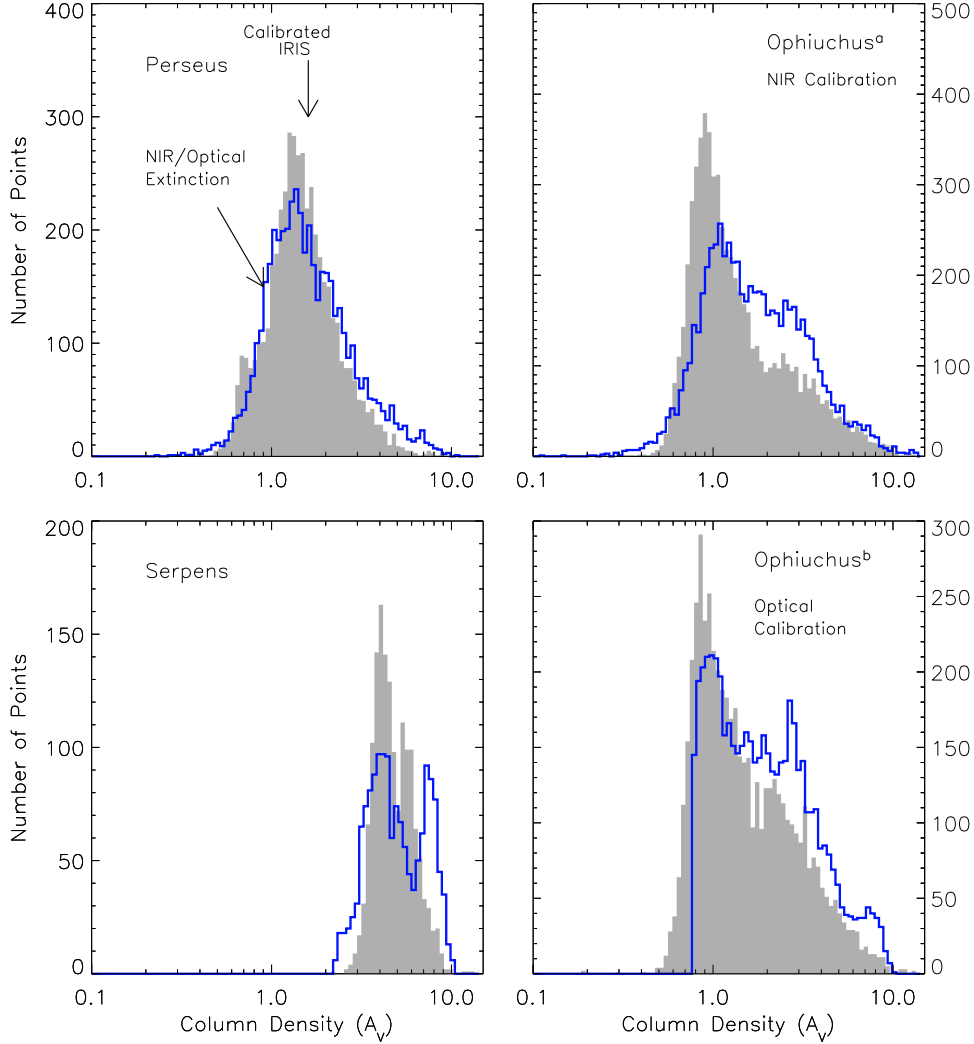


Figure 2.6.— The filled histograms show the extinction derived from the 60/100 μm flux density ratio in Perseus, Serpens and Ophiuchus after the calibration described in Section 2.2. The blue open histogram shows the NIR/optical derived extinction (from Ridge et al. (2006b) and Cambr sy (1999)). The Ophiuchus^a histogram (top right) is calibrated to the 2MASS extinction map. The Ophiuchus^b histogram (bottom right) is calibrated to the Cambr sy data.

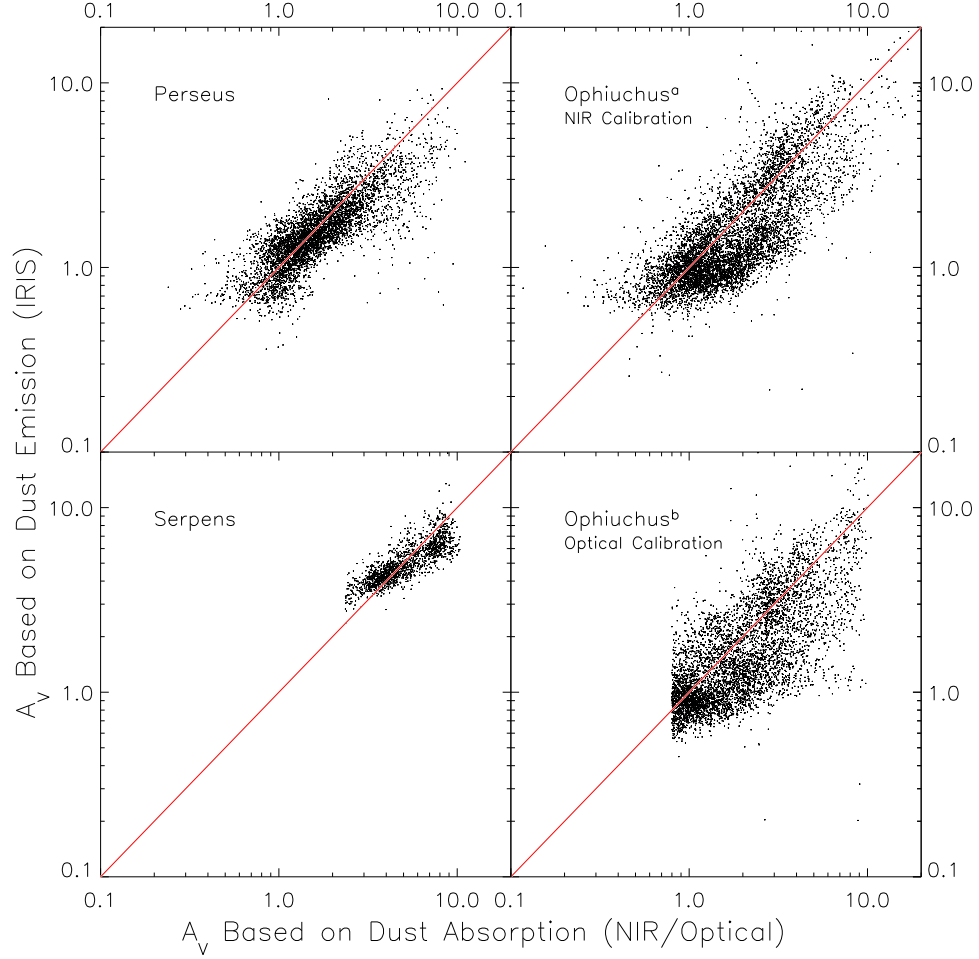


Figure 2.7.— Scatter plot of the corrected IRIS extinction (derived from the 60/100 μm flux density ratio in Perseus, Serpens and Ophiuchus) and the model extinction (from Ridge et al. (2006b) and Cambr sy (1999)). The Ophiuchus^a IRIS extinction (top right) is calibrated to the 2MASS extinction map. The Ophiuchus^b IRIS extinction (bottom right) is recalibrated to the Cambr sy data. Note that the data are shown here in log-log plots for clarity of display, but all the fitting is of linear (not log) quantities. The sharp cutoff in the Ophiuchus^b panel is a result of having added 0.71 magnitudes to the optically derived extinction. The sharp cutoff in the Serpens panel is a result of having added 2.2 magnitudes to the optically derived extinction.

Table 2.2. Best Fit IRAS/dust Parameters

Cloud	δ	ω	X	A_V offset (mag A_V)
Perseus	0.32	0.0180	1100	—
B5	0.38	0.0140	1200	—
IC348	0.33	0.0160	1000	—
NGC1333	0.64	0.0010	1300	—
c2d Area	0.36	0.0140	1200	—
Ring	0.38	0.0150	990	—
Ophiuchus ^a	0.46	0.0016	510	—
Ophiuchus ^b	0.40	0.0006	350	0.71
Serpens	0.35	0.0139	800	2.36

Note. — Best fit values for the parameters used to convert IRIS flux to visual extinction

^aIRAS flux normalized to the 2MASS/NICER extinction

^bIRAS flux normalized to the Cambr sy extinction

As a test to see if the parameters determined for one cloud can be successfully used to describe another, we used the Perseus fits for δ , ω and X for the Ophiuchus 60 and 100 μm IRIS maps and compared the derived extinction to the 2MASS extinction map of Ophiuchus. The median point-to-point difference was 0.8 magnitudes of visual extinction, with a standard deviation of 1.9 magnitudes. When the optimized parameters for Ophiuchus are used, the median point-to-point difference is only 0.2 mag, with a scatter of 1.2 mag. We conclude that *the fits for one cloud are unlikely to be appropriate for other clouds*, and therefore caution should be used in attempts to estimate extinction within molecular clouds from IRAS emission maps alone.

We have derived separate values for δ , ω and X for various regions within Perseus to see if the dust properties are significantly different there than in the cloud as a whole. The regions considered were B5, IC348, NGC1333, the emission ring, and the area surveyed by the c2d Spitzer Legacy project. The locations and sizes of the Perseus sub-regions are shown in Table 2.1. The values of δ , ω and X for these sub-regions are shown in Table 2.2 and displayed in Figure 2.2. The value of δ varies by about 10 percent, ω varies by about 20 percent and X varies by 20 percent in these sub-regions of Perseus. NGC1333 varies much more significantly from the other sub-regions of Perseus.

We conclude that the method described here for converting dust emission to visual extinction can be used with confidence to find regions with high or low extinction and to determine the average extinction in large areas (~ 0.25 square degrees). However, the extinction determined in any individual $5'$ pixel *should not be trusted* to represent the true absolute extinction to better than ~ 2.5 magnitudes (2σ) of visual extinction. This is made clear by the significant variability in the emissivity spectral index of dust and the conversion from dust optical depth to visual extinction between clouds and within clouds, as shown in Tables 2.2 and 2.3.

2.5.5 Emissivity Spectral Index

The emissivity spectral index that we use in this paper varies with temperature as shown in Equation 2.2. The values that we find for the parameters δ and ω are shown in Table 2.2. Their values as determined by Dupac et al. (2003) are 0.4 and 0.008 respectively, which comes from a much broader range of environments and many more measurements of the FIR/sub-mm flux. Figure 2.8 shows the emissivity spectral index that we find for each cloud plotted along with the curve from Dupac et al. (2003). The emissivity spectral index is considerably larger in Ophiuchus than in Serpens, which is somewhat higher than β in Perseus. The best-fit curve to the

wider range of environments in Dupac et al. (2003) falls between our Serpens and Ophiuchus curves.

2.6 Summary

We have described a new method that uses NIR color excesses or optical star counts to constrain the conversion of IRIS 60 and 100 μm data into color temperature and column density maps. Our method also derives the dust emissivity spectral index and the conversion from dust 100 μm optical depth to visual extinction. We test the IRIS 60 and 100 μm zero points and confirm that, unlike earlier releases of IRAS data, the IRIS recalibration is properly zero point corrected. We find the the very small grain contribution to the 60 μm flux is significant.

The dust temperature maps of Perseus, Serpens and Ophiuchus available through the COMPLETE website should be the best dust temperature maps of large star forming regions at 5' resolution created to date. The dust temperatures derived here are dependent on the emissivity spectral index of the dust, which is solved globally for each molecular cloud, and recorded in Table 2.2.

Our work here indicates that one can not confidently convert dust 100 μm optical depth to visual extinction without the benefit of having an extinction map made in an alternative manner to use as a model because the conversion constant X varies significantly from cloud to cloud, and even within a cloud (see Table 2.2). Using the values for the dust emissivity spectral index and visual extinction conversion derived for one cloud results in a significant miscalculation of the extinction in other clouds. Even with the NICER and optical star counting extinction maps used here to calibrate the IRAS data, there is significant point-to-point variation between the two estimates (see Figure 2.1). In fact, we have shown that in Ophiuchus the optical star count method employed by Cambr sy (1999) has an offset from the NICER method applied to the 2MASS data set of ~ 0.71 magnitudes in A_V , with a scatter of 0.7 magnitudes, so the issue is not simply one of dealing with the FIR dust properties in molecular clouds.

In addition, we have identified a ring structure in Perseus, which is discussed in Ridge et al. (2006a).

Table 2.3. Scatter between IRAS implied extinction and NIR/optical derived extinction

Cloud	Median Difference (mag A_V)	1σ Scatter Between Methods (mag A_V)	Scatter Between Methods Percent	τ_{100}/A_V 10^{-4} mag^{-1}
Perseus ^a	-0.1	0.9	30	9 ± 3
Ophiuchus ^a	-0.2	1.2	50	17 ± 9
Ophiuchus ^b	-0.2	1.4	50	23 ± 13
Serpens ^b	0.0	1.2	20	12 ± 3

Note. — Median difference between the different ways to estimate extinction within a molecular cloud (IRIS A_V - NIR/optical A_V), and the scatter between the methods (see Section 2.5.4).

^aIRAS flux normalized to the 2MASS/NICER extinction

^bIRAS flux normalized to the Cambr  sy extinction

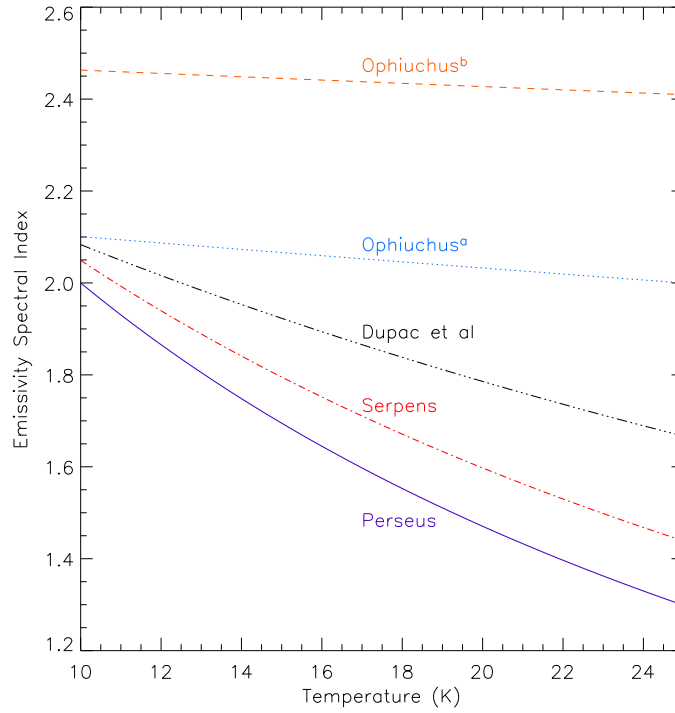


Figure 2.8.— Plot of the emissivity spectral index versus temperature for Perseus, Ophiuchus and Serpens. The Ophiuchus^a curve is for the IRIS data calibrated to the 2MASS extinction map. The Ophiuchus^b curve is calibrated to the Cambr  sy data. The Dupac et al. curve is the best fit curve to a collection of FIR/sub-mm emission regions as presented in Dupac et al. (2003).

Acknowledgements

We would like to thank the referee Laurent Cambr sy for many useful comments. This research has made use of the NASA/ IPAC Infrared Science Archive, which is operated by the Jet Propulsion Laboratory, California Institute of Technology, under contract with the National Aeronautics and Space Administration. This publication makes use of data products from the Two Micron All Sky Survey, which is a joint project of the University of Massachusetts and the Infrared Processing and Analysis Center/California Institute of Technology, funded by the National Aeronautics and Space Administration and the National Science Foundation. This material is based upon work supported under a National Science Foundation Graduate Research Fellowship.

Chapter 3

Estimating the Column Density in Molecular Clouds with Far-Infrared and Submillimeter Emission Maps

Scott Schnee, Tom Bethell & Alyssa Goodman

The Astrophysical Journal, Volume 640, Issue 1, pp. L47-L50

Abstract

We have used a numerical simulation of a turbulent cloud to synthesize maps of the thermal emission from dust at a variety of far-IR and sub-mm wavelengths. The average column density and external radiation field in the simulation is well matched to clouds such as Perseus and Ophiuchus. We use pairs of single-wavelength emission maps to derive the dust color temperature and column density, and we compare the derived column densities with the true column density. We demonstrate that longer wavelength emission maps yield less biased estimates of column density than maps made towards the peak of the dust emission spectrum. We compare the scatter in the derived column density with the observed scatter in Perseus and Ophiuchus. We find that while in Perseus all of the observed scatter in the emission-derived versus the extinction-derived column density can be attributed to the flawed assumption of isothermal dust along each line of sight, in Ophiuchus there is additional scatter above what can be explained by the isothermal assumption. Our results imply that

variations in dust emission properties within a molecular cloud are not necessarily a major source of uncertainty in column density measurements.

3.1 Introduction

In the absence of direct measurements of extinction, the column density of dust in molecular clouds is often traced by dust emission. In many cases the data are maps at two wavelengths in the FIR or sub-mm, and the column density is derived by assuming that dust along each line of sight is isothermal (Wood et al. 1994; Schlegel et al. 1998; Schnee et al. 2005). However, each line of sight through a molecular cloud is likely to intersect regions with various amounts of shielding, and therefore a range of temperatures, so the isothermal assumption may lead to significant errors in the calculation of column density.

In this paper we use a simulation of an externally heated turbulent molecular cloud to produce maps of column density and thermal emission at various FIR and sub-mm wavelengths. We discuss the bias in the emission-derived column density as a function of extinction and wavelength, and we compare the scatter in the emission-based column density estimate with that observed in Schnee et al. (2005) in the Perseus and Ophiuchus molecular clouds. We find that assuming isothermality can account for all of the observed point by point scatter in comparisons of extinction and emission-based column density maps of Perseus without the need to invoke variations in the dust properties within a molecular cloud or variations in the emission from stochastically heated grains. In comparison, the scatter in Ophiuchus is significantly larger than can be accounted for by the error introduced by the isothermal dust assumption alone.

3.2 The Model Cloud

The methods of determining the dust distribution, radiative transfer and dust heating, only briefly described in this Section, are described in more detail in Bethell et al. (2004).

3.2.1 Density Structure

The density structure is created by a three-dimensional simulation of driven MHD turbulence on a cubical grid with 128 cells on a side (Heitsch et al. 2001). Although the original ensemble of simulations was created with widely varying physical parameters (Mach number, plasma beta etc.), the radiative transfer through the resulting structures is largely insensitive to these differences. To simulate Perseus and Ophiuchus we use one such model and scale the density and size of our model cloud so that the column density map has an average $A_V \sim 2$, which is the median A_V in our Perseus and Ophiuchus extinction maps. This choice of model is meant to be illustrative of the broad effects of including ‘realistic’ clumpiness in radiative transfer calculations of molecular clouds. When compared to a uniform density distribution of similar mass the inclusion of clumpiness tends to expose more of the *volume* to the interstellar radiation field (ISRF) while on average the *mass* is both less illuminated and sees bluer light. In the clumpy case there is also little correlation between the intracloud radiation field at a point and its proximity to the cloud edge. Instead, there is a large point-to-point scatter, arising from the details of the clumpiness (Bethell et al. 2004).

3.2.2 Radiative transfer

A Reverse Monte Carlo radiative transfer code (Bethell et al. 2004) is used to calculate the penetration of an external isotropic and homogeneous ISRF, here the ISRF given by Mathis et al. (1983). The reverse Monte Carlo technique enables the user to control the Monte Carlo photon noise in regions which are well shielded, in particular the clumps where most of the mass resides. The re-emission by dust of sub-mm radiation is assumed to be optically thin throughout our cloud.

3.2.3 Dust properties

To calculate self consistently the attenuation of the ISRF by dust, the subsequent equilibrium dust temperature and the FIR emission we use astronomical silicate and graphite grain opacities (Draine & Lee 1984)¹ and a power-law grain size distribution (Mathis et al. 1977). These are chosen to reproduce an extinction curve with $R_V = A_V/E(B - V) = 3.1$. No attempt is made to include very small grains which are heated transiently to high temperatures, nor do we include polycyclic

¹For tabulated optical properties visit the website www.astro.princeton.edu/~draine.

aromatic hydrocarbon emission. Both these populations contribute significantly to the emission at wavelengths shorter than 100 μm .

At far infrared wavelengths ($\lambda > 100\mu\text{m}$) the dust ensemble emission is described by a blackbody spectrum modified by a power law ($S_\lambda \propto B_\lambda(T_d)\lambda^{-\beta}$) with an emissivity spectral index of $\beta = 2$. With the dust ensemble fully prescribed we can calculate the equilibrium grain temperatures of each grain type and grain size at each location. Not only do dust temperatures vary along each line of sight, they also vary amongst grain types and sizes at any point within the cloud.

3.3 Derived Color Temperature and Column Density

The method used to determine the dust temperature and column density from two emission maps is similar to that used in Schnee et al. (2005). The dust temperature (T_d) is determined by the ratio of two flux densities and the column density can be derived from either flux and the derived color temperature of the dust. The pairs of fluxes that we study in this paper are 60 and 100 μm (the longest wavelength IRAS bands), 100 and 240 μm (those used in Schlegel et al. (1998), hereafter SFD98), 100 and 850 μm and 450 and 850 μm (wavelengths observed by SCUBA on the JCMT (Holland et al. 1999)).

To determine the dust color temperature, we use the equation:

$$R = \left(\frac{\lambda_1}{\lambda_2}\right)^{-(5+\beta)} \left(\frac{\exp[hc/\lambda_2 k T_d] - 1}{\exp[hc/\lambda_1 k T_d] - 1}\right) \quad (3.1)$$

where R is the ratio of the fluxes and β is the emissivity spectral index of the dust. We calculate the dust temperature with the assumption that $\beta = 2$, which is true of the dust in our model. Note that in using the ratio of two flux maps to get the color temperature, we are assuming that a single temperature, T_d , can be used to describe all the dust along each line of sight.

The optical depth is determined by the ratio of the flux to the Planck function:

$$\tau_\lambda = \frac{F_\lambda}{B_\lambda(T_d)} \quad (3.2)$$

with the assumption that the dust emission is optically thin.

The optical depth can then be converted to V-band extinction using:

$$A_V = X\tau_\lambda \quad (3.3)$$

where X is a parameter relating the thermal emission properties of dust to its optical absorption qualities. The extinction, A_V , is derived from the column density of dust in our model, using the conversions $N_H/E(B - V) = 5.8 \times 10^{21} \text{ cm}^{-2}$ and $A_V/E(B - V) = 3.1$. We use the IDL procedure AMOEBA to determine the value of X that minimizes the difference between the emission-derived column density and the true column density in the simulation.

3.4 Results

3.4.1 Dependence on Wavelength

The column density of dust derived from pairs of thermal emission maps depends strongly on the two wavelengths considered. Figure 3.1 shows that the 60 and 100 μm derived column density is a linear tracer of the actual column density for $A_V < 1$ mag, but systematically underestimates the true column density for $A_V > 1$ mag. The same trend is seen in the column density derived from the 100 and 240 μm emission maps, though the cutoff extinction above which the column densities are underestimated is $A_V \sim 4$ mag. The column density derived from the 100 and 850 μm maps traces the true column density all the way to 10 mag A_V , as does the column density derived from the 450 and 850 μm emission maps. The errors introduced by the assumption of isothermal dust along each line of sight for each pair of maps is shown in Figure 3.1.

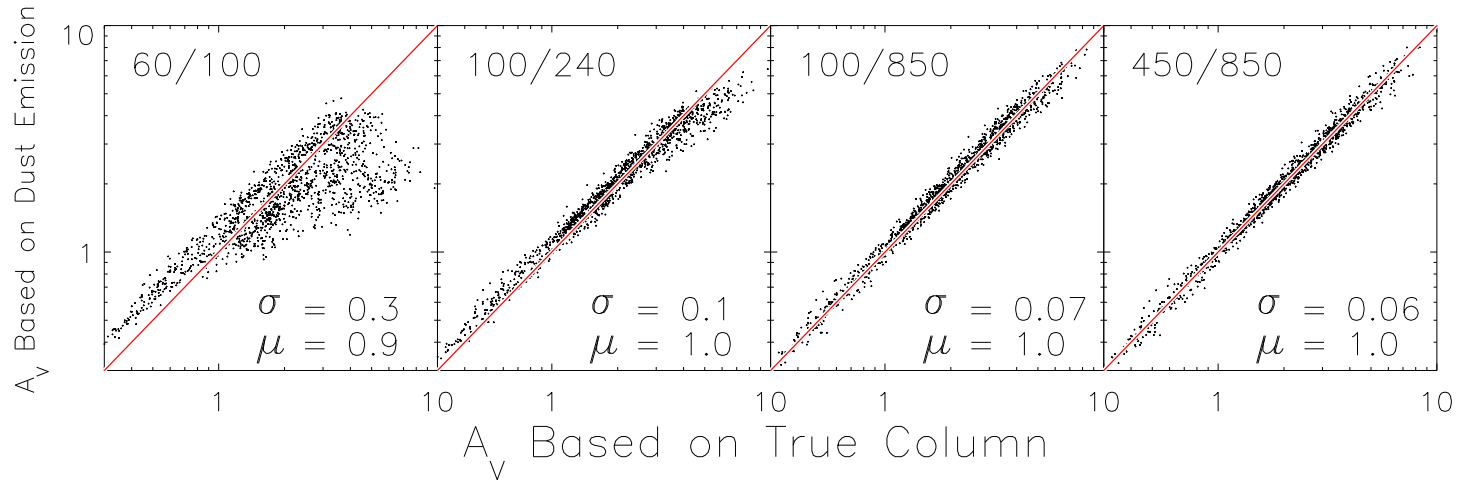


Figure 3.1.— The column density derived from two emission maps plotted against the true column density. The wavelengths used are, from left to right: 60 & 100 μm , 100 & 240 μm , 100 & 850 μm and 450 & 850 μm . The values of X that convert from the FIR optical depth to visual extinction are $\tau_{100} = 775$, $\tau_{100} = 231$, $\tau_{100} = 69$, and $\tau_{450} = 681$. The values of μ and σ refer to the center and width of the Gaussian fit to the distribution of the ratio ($A_{V_{\text{emission}}}/A_{V_{\text{true}}}$).

The underestimation of column density at $A_V > 1$ as derived from the 60 and 100 μm emission maps comes from an overestimate of dust temperature along lines of sight that pass through various environments with different temperatures. The emission is then dominated by the warmer regions, while the column density is dominated by the cooler and denser regions. The derived color temperature is thus more representative of the warmer regions, and the derived optical depth is therefore too low. This effect can be seen clearly in the leftmost panel of Figure 3.1. Because X has been scaled to minimize the difference between the emission and absorption derived column densities, the derived column densities of points below $A_V = 1$ are overestimated. This problem is much less significant when the emission maps are in the Rayleigh-Jeans portion of dust emission spectrum (Bethell et al. 2004), which explains why the two panels on the right side of Figure 3.1 show a much tighter correlation between the derived column density and the true column density than the two panels on the left. Similarly, the longer wavelength emission maps, shown in Figure 3.2, trace the true column density much better than the shorter wavelength maps.

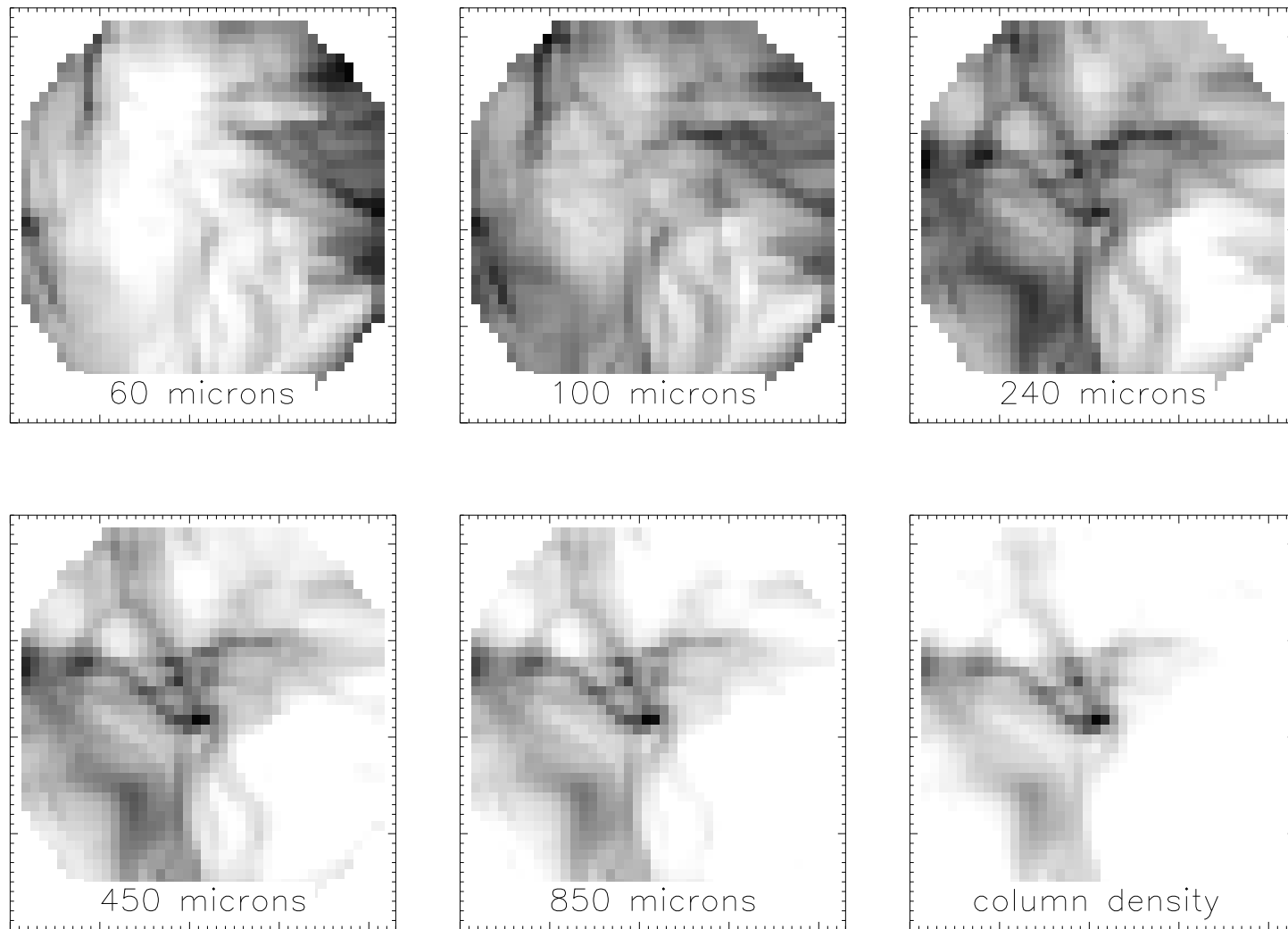


Figure 3.2.— The flux maps at the five wavelengths considered in the paper, plotted along with the true column density. All of the maps are scaled to have the same dynamic range with their maxima black and minima white.

3.4.2 Variable Dust Properties

In order to isolate the effect of the assumption of isothermal dust along each line of sight through a molecular cloud on the emission-derived column density, we have kept the dust properties in our model invariant. However, recent observations have shown that the overall submillimeter emissivity of dust grains varies within a molecular cloud (Stepnik et al. 2003) and that the emissivity spectral index of dust within a molecular cloud also varies (Dupac et al. 2003). The scatter between emission-derived column density and the true column density shown in Figure 3.1 arises solely from the assumption of isothermal dust, and does not include the effects of variable dust emission properties. When the column density is derived from 60 and 100 μm observations, the effect of variable grain properties may not be important, because the assumption of isothermal dust makes deriving the column density from emission maps impractical above $A_V > 1$ while dust properties are not seen to vary significantly below $A_V < 2$ (Stepnik et al. 2003). When the emission maps are longer wavelength (e.g. from DIRBE, PRONAOS or SCUBA), the assumption of isothermal dust is less problematic (as shown in Figure 3.1) and the variable dust properties may become the dominant source of error in the emission-derived column density.

3.4.3 Emission from Very Small Grains

We have shown in Schnee et al. (2005) that the 60 μm emission of molecular clouds comes predominantly from transiently heated very small dust grains (VSG's). In order to derive the dust temperature, we have removed the VSG contribution to the 60 μm IRAS flux. Because we have no way to determine the VSG contribution on a pixel-by-pixel basis, we assume that the percent emission from VSG's at 60 μm is constant everywhere in Perseus and Ophiuchus. We then determine the 60 μm scale factor such that the median temperature in our maps is equal to the median temperature derived by SFD98 for the same area. The SFD98 temperature maps were derived using 100 and 240 μm data and are therefore unbiased by the emission from the VSG's. This procedure is identical to that performed in Schnee et al. (2005). The 60 μm flux from our model was not subjected to such a scaling factor because no VSG contribution to the flux was included.

Though scaling the 60 μm flux by a constant multiplicative factor can give the proper *average* temperature, each line of sight through our observed molecular clouds should ideally be treated with its own scaling factor. The variable VSG contribution to the 60 μm flux can't be removed on a pixel-by-pixel basis because

the SFD98 resolution is too coarse, which introduces errors in the derivation of dust temperature and column density. Applying a constant scale factor to the $60\ \mu\text{m}$ flux does not correct for this error, nor does it introduce additional scatter in Figure 3.3. The derived value of X does depend on this scale factor.

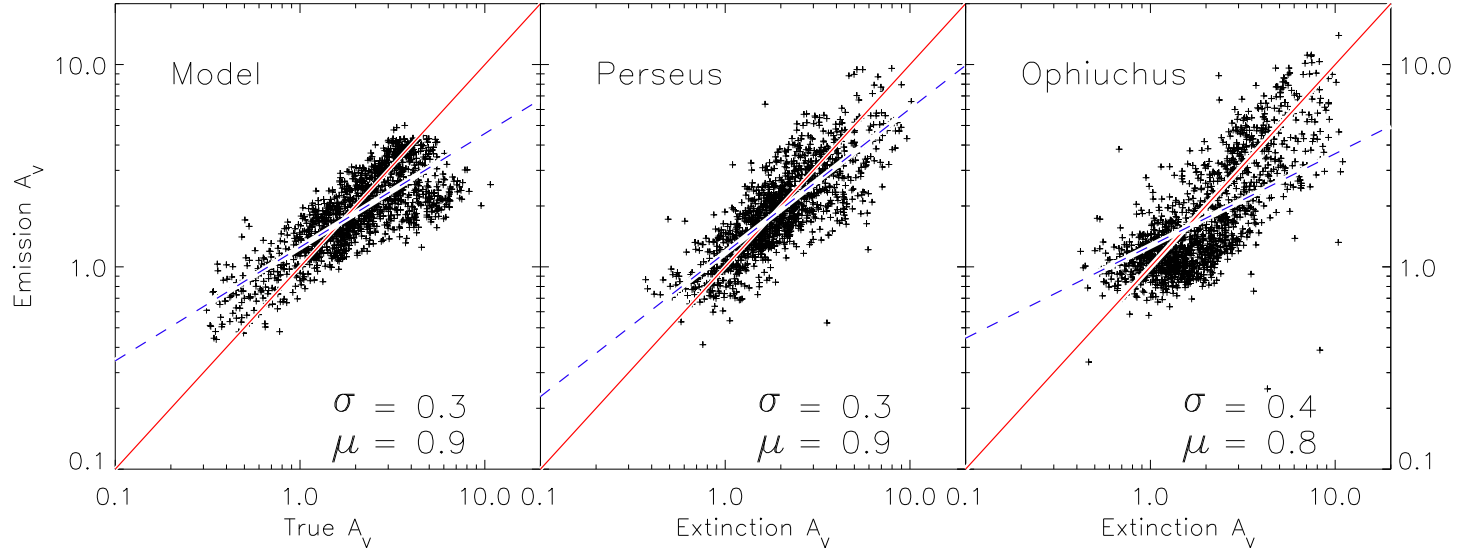


Figure 3.3.— The column density derived from 60 and 100 μm emission maps (assuming $\beta = 2$) plotted against the “true” column density. The model’s true column density has been altered by Gaussian “noise” with a 1σ of 0.2 mag A_V to match the noise in observational estimates of extinction. The middle and right panels come from Schnee et al. (2005), where the extinction is measured from NIR colors of background stars and the 60 and 100 μm flux from the IRAS survey are used to estimate the column density from dust emission. The blue (dashed) line shows the best fit between the emission-derived column density and the “true” column density. The slope of the model fit is 0.53 which is intermediate between the Perseus and Ophiuchus slopes (0.66 and 0.46, respectively). The values of μ and σ refer to the center and width of the Gaussian fit to the distribution of the ratio ($A_{V_{\text{emission}}}/A_{V_{\text{true,extinction}}}$).

If high resolution data at 100 μm and longer wavelengths were available for a molecular cloud, then one could use those maps to avoid having to subtract the VSG contribution to the observed emission. Unfortunately, the dust temperature and column maps produced by SFD98 using existing 100 and 240 μm data are of much lower resolution ($\sim 1^\circ$) than the IRAS maps ($\sim 5'$). Even nearby molecular clouds require the higher resolution provided by IRAS, so we compare our model molecular cloud with the observations of Perseus and Ophiuchus using IRAS emission maps.

3.4.4 Comparison with Observations

In real molecular clouds the best estimate of column density often comes from the measured NIR colors of background stars and is calculated from the reddening caused by the intervening dust. Column density maps made this way have a fundamental uncertainty because the background stars have a spread in their intrinsic NIR colors, and because the stars included in each pixel of the column density map sample slightly different lines of sight through the molecular cloud. The level of uncertainty is approximately 0.2 mag A_V , and it is independent of column density (Ridge et al. 2006b).

In order to compare our simulation to observations, we have added normally-distributed noise (with $1\sigma = 0.2$ mag) to the simulated column density. Assuming $\beta = 2$, we then derived the value of X that best matches the emission-derived column density (from the 60 and 100 μm maps) to the new “true” column density. The result is shown in Figure 3.3.

The left panel of Figure 3.3 appears similar to the Perseus and Ophiuchus extinction scatter plots, produced as described in Schnee et al. (2005), shown here in the center and right panels. The emission-based column densities in Perseus and Ophiuchus are derived from IRAS 60 and 100 μm maps and the extinction is derived from NIR color excesses (Ridge et al. 2006b). The column derived from FIR emission maps is overestimated at low extinctions and underestimated at high extinctions in both this paper and in observations. The 1σ width of the Gaussian fit to the ratio of emission-derived column density and absorption-derived column density are 0.3 in our simulation, 0.3 in Perseus and 0.4 in Ophiuchus, as shown in Figure 3.3.

We are able to reproduce the scatter observed in Perseus between the column density derived from 60 and 100 μm emission maps and the extinction in our simulation of a turbulent molecular cloud. The dust in our simulation does not have variable emission properties, nor is there a population of transiently heated

VSG's. This suggests that any variations in dust properties within Perseus do not dominate the uncertainty in the emission-derived column density, nor does the emission from the VSG's. Instead, we find that in Perseus the scatter is primarily explained by the assumption of isothermal dust along each line of sight. In contrast, the Ophiuchus molecular cloud has a larger emission/absorption derived scatter than can be explained solely by the errors introduced by the assumption of isothermal dust along each line of sight.

We have shown in Schnee et al. (2005) that in order to produce column density maps of nearby molecular clouds from IRAS emission maps, it is necessary to determine both the fraction of 60 μm emission that comes from transiently heated dust grains and the conversion factor (X) from 100 μm optical depth to visual extinction, because both of these quantities vary from place to place. These parameters can be determined by the temperature maps of SFD98 and 2MASS/NICER extinction maps.

3.5 Summary

We have shown that column density estimates from longer wavelength thermal emission maps are less biased and have less uncertainty than estimates made from shorter wavelength maps. In particular, maps of column density derived from 60 and 100 μm emission maps or 100 and 240 μm emission maps systematically overestimate the dust temperature at high extinctions (>1 mag A_V and 4 mag A_V , respectively) and underestimate the column density.

We have also shown that the observed uncertainty in column density derived from IRAS emission maps of Perseus can be fully accounted for by errors introduced by the assumption of isothermal dust along each line of sight through the cloud and uncertainty in the extinction-derived column density. We find no evidence of variable dust emission properties or variations in the fraction of emission at 60 μm from transiently heated VSG's creating significant scatter in column density estimates in Perseus. The observed scatter in the emission/absorption derived column density in Ophiuchus can be largely, but not fully, explained by the assumption of isothermal dust along each line of sight, suggesting that the VSG emission and/or dust properties vary within the Ophiuchus molecular cloud.

Acknowledgements

T. Bethell would like to thank Fabian Heitsch for making available his simulations of MHD turbulence. We would like to thank Ellen Zweibel for her numerous insights and helpful suggestions. The 60/100 μm and NIR extinction maps of Perseus and Ophiuchus analyzed in this paper were created for the COMPLETE Survey of Star-Forming Regions (Goodman 2004; Ridge et al. 2006b). Scott Schnee is supported under a NSF Graduate Research Fellowship. Tom Bethell is partially supported by NSF AST 03-28821 and NASA ATP 04 0114 to U. Wisconsin. This work has been partially supported by the National Science Foundation through award AST-0407172.

Chapter 4

Density and Temperature Structure of TMC-1C from 450 and 850 Micron Maps

Scott Schnee & Alyssa Goodman 2005

The Astrophysical Journal, Volume 624, Issue 1, pp. 254-266

Abstract

We have mapped the central $10' \times 10'$ of the dense core TMC-1C at 450 and 850 μm using SCUBA on the James Clerk Maxwell Telescope. The unusually high quality of the 450 μm map allows us to make a detailed analysis of the temperature and column density profiles of the core. We find that the dust temperature at the center of TMC-1C is ~ 7 K, rising to ~ 11 K at the edges. We discuss the possibility and effects of a variable emissivity spectral index on the derived mass profile.

The low dust temperature of TMC-1C results in a high derived mass for the core, significantly larger than the virial mass estimated from the linewidth of the N_2H^+ transition. This result is valid within a wide range of dust properties and ellipticities of the core. The N_2H^+ spectra, taken with the IRAM 30m telescope, show signs of self-absorption, which provide evidence of sub-sonic infall motions. The derived density profile and infall velocity is compared to the predictions of several popular star formation models, and the Bonnor-Ebert model is the best fit analytic model.

4.1 Introduction

Prestellar cores are self-gravitating condensations in molecular clouds that are much denser and colder than their surrounding medium. These objects (such as L1544 and L1521F) are believed to be on the verge of collapse, and infall motions are not uncommon (Williams et al. 1999; Crapsi et al. 2004). Because prestellar cores are at a critical point on the way to becoming a star, their properties, such as density and temperature distribution, as well as their velocity field, are of particular interest. The density and temperature profiles for prestellar cores are difficult to obtain from molecular line data, because gases can deplete onto the dust grains at the high ($n \gtrsim 10^4 \text{ cm}^{-3}$) densities and low temperatures ($T < 10 \text{ K}$) present in the interiors of cores. A more accurate estimate can be obtained from measurements of the dust emission, which peaks at submillimeter wavelengths and is often optically thin. Observations at multiple submillimeter wavelengths can be used to determine such properties as the temperature, density, emissivity, and spectral index of the dust (Hildebrand 1983). Kinematic information, such as infall, outflow, and rotation, can be determined by molecular line observations of carefully chosen high and low density tracers (Caselli et al. 2002b; Belloche et al. 2002; Di Francesco et al. 2001).

TMC-1C is a starless core in the Taurus molecular cloud complex, at a distance of 140 pc (Kenyon et al. 1994). Taurus is known to be a site of low mass, somewhat isolated star formation. TMC-1C has previously been observed to be a “coherent core,” meaning that its velocity dispersion is constant, at slightly more than the sound speed, over a radius of 0.1 pc (Barranco & Goodman 1998; Goodman et al. 1998). In addition, it shows a velocity gradient consistent with solid body rotation, at $0.3 \text{ km s}^{-1} \text{ pc}^{-1}$ (Goodman et al. 1993). Because TMC-1C is fairly nearby and has interesting kinematics, it is a good candidate starless core for further study.

In this paper we use continuum data taken with SCUBA at 450 and 850 μm to determine the temperature and mass distribution of the dust in TMC-1C, and spectral line maps from the IRAM 30m dish to provide velocity information. In Section 4.5.4 we note how changes in the assumed dust emissivity alter the conclusions of our analysis. In Section 4.5.6 we compare the mass derived from our multiwavelength observations to the mass we would have derived if only 850 μm data had been available to us. In Section 4.5.7, various collapse models for star formation are considered, and their predictions for infall speed and density profile are compared to observations. Finally, we conclude that for a wide range of assumptions, TMC-1C is a collapsing coherent core that is not especially well fit by any of the star formation models that are available.

4.2 Observations

4.2.1 Continuum

We observed a $10' \times 10'$ region of TMC-1C in Taurus with SCUBA (Holland et al. 1999) on the JCMT in exceptionally stable grade 1 weather. We used the standard scan-mapping mode, creating $850 \mu\text{m}$ and $450 \mu\text{m}$ maps simultaneously (Pierce-Price et al. 2000; Bianchi et al. 2000). Three chop throw lengths of $30''$, $44''$, and $68''$ were used in both the right ascension and declination directions. The JCMT has beam widths of $7.5''$ at $450 \mu\text{m}$ and $14''$ at $850 \mu\text{m}$ which subtend diameters of 0.005 and 0.01 pc, respectively, at the distance of Taurus. Pointing during the observations was typically good to $3''$ or better.

The data were reduced using the SCUBA User Reduction Facility (SURF) (Jenness & Lightfoot 1998). The data were flatfielded, extinction corrected using skydips, despiked, baseline corrected, and had sky noise removed. Maps were then made using Emerson Fourier deconvolution (Emerson 1995). The resultant maps were calibrated with the source CRL618, with uncertainties in the calibrator's flux densities of $\sim 3.7\%$ at $850 \mu\text{m}$ and $\sim 12.5\%$ at $450 \mu\text{m}$. The noise level of the $850 \mu\text{m}$ map is 0.009 Jy/beam, and 0.053 Jy/beam in the $450 \mu\text{m}$ map. Note that the scan-mapping mode is insensitive to structures on scales greater than a few times the largest chop throw. The flux maps can be seen in Figure 4.1.

4.2.2 Spectral Line

The 3 mm N_2H^+ (1-0) observations shown in this paper were taken with the IRAM 30m telescope, and will be discussed in more detail in an upcoming paper (Schnee et al. 2006b). A beam sampled map of the inner $\sim 2'$ of TMC-1C was obtained in frequency switching mode with a spectral resolution of 0.06 km s^{-1} . The data were reduced using the CLASS package developed jointly between Observatoire de Grenoble and IRAM. Second order polynomial baselines were subtracted from the data, and the seven hyperfine components of the N_2H^+ (1-0) spectra were fit simultaneously with Gaussians for emission and absorption (Caselli et al. 1995). The properties of the N_2H^+ (1-0) transition at the central position are shown in Table 4.1 and the spectrum at that position is shown in Figure 4.2.

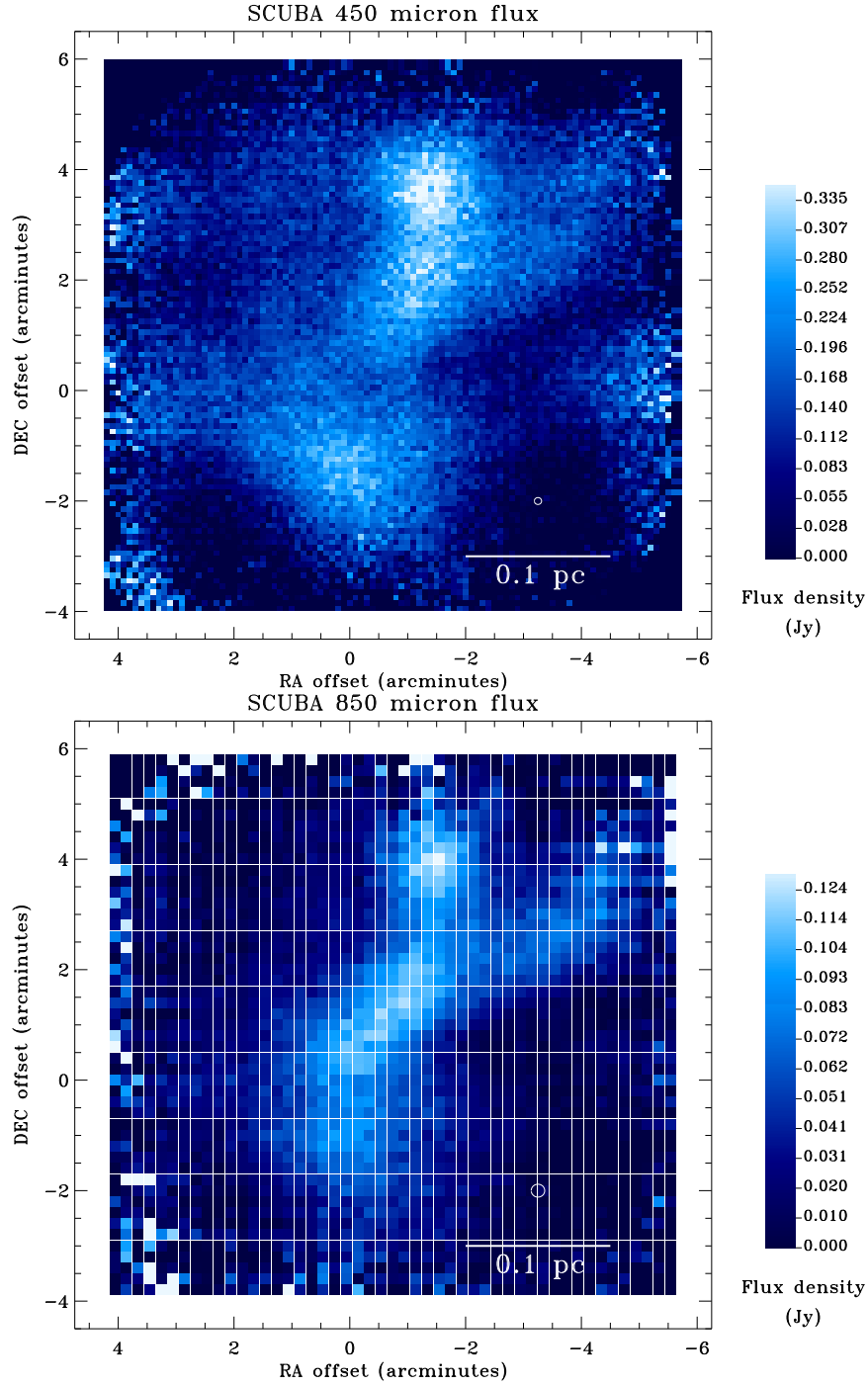


Figure 4.1.— The $450\mu\text{m}$ (top) and $850\mu\text{m}$ (bottom) emission maps of TMC-1C. The SCUBA beam size is displayed in each map. The coordinates of the (0,0) position are RA=4:41:38.8 DEC=+25:59:42 (J2000).

Table 4.1. N_2H^+ Spectrum at (0,0)^a of TMC-1C

Transition	Frequency GHz	Signal / Noise	Noise Kelvin	V_{LSR} km s^{-1}	Line Width km s^{-1}
N_2H^+	93.176	9.8	0.145	-2.787	0.246

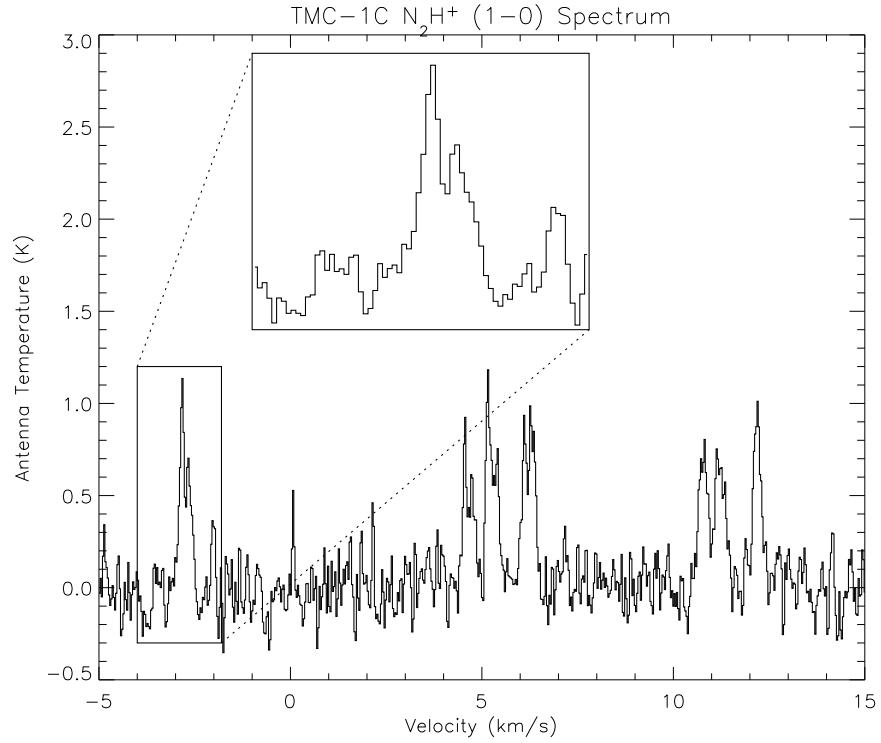
^a(RA,DEC) (J2000) at (0,0) 04:41:38.8 +25:59:42

Figure 4.2.— N_2H^+ (1-0) spectrum from the (0,0) position. Note the seven hyperfine components. The isolated component is shown at $\sim -2.8 \text{ km s}^{-1}$. The velocity scale is only relative to the LSR for the central component.

4.3 Dust Properties

Thermal emission from dust can be used to determine such physical properties as temperature, density, and mass. However, the derivation of these quantities requires knowledge of the somewhat poorly known emission characteristics of the dust grains. In this section we discuss our assumptions and methods to derive the properties of TMC-1C from our sub-mm continuum observations.

4.3.1 Assumed Parameters

The dust is assumed to emit as a modified blackbody, with emissivity parameter $Q = (\lambda/\lambda_0)^{-\beta}$. The flux coming from the dust at a particular wavelength is therefore given by (Mitchell et al. 2001)

$$S_\lambda = \Omega B_\lambda(T_d) \kappa_\lambda \mu m_H N_H \quad (4.1)$$

where

$$B_\lambda(T) = \frac{2hc^2}{\lambda^5} \frac{1}{\exp(hc/\lambda kT) - 1} \quad (4.2)$$

and

$$\kappa_\lambda = \kappa_{1300} \left(\frac{\lambda}{1300 \mu\text{m}} \right)^{-\beta} \quad (4.3)$$

In Equation 4.1, S_λ is the flux density; Ω is the solid angle of the beam; $B_\lambda(T_d)$ is the black body emission from the dust at temperature T_d ; $\kappa_{1300} = 0.005 \text{ cm}^2 \text{ g}^{-1}$ is the emissivity of the dust grains at $1300 \mu\text{m}$ (Andre et al. 1996; Preibisch et al. 1993); m_H is the mass of the hydrogen atom; $\mu = 2.33$ is the mean molecular weight of interstellar material in a molecular cloud, and N_H is the column density of hydrogen nuclei. For a true blackbody $\beta = 0$; for amorphous, layerlattice material $\beta \sim 1$; for metals and crystalline dielectrics $\beta \sim 2$, cf (Henning et al. 1995). We assume the emission is optically thin at both 850 and $450 \mu\text{m}$, which is justified for H_2 column densities less than $\sim 10^{24}$ (~ 500 magnitudes of visual extinction) (Zucconi et al. 2001).

4.3.2 Derivation of Temperature

Because the thermal emission from cold (~ 10 K) dust at 450 and $850 \mu\text{m}$ is both optically thin and near the peak of the modified blackbody spectrum, SCUBA is well-suited to observations of starless cores. A dust color temperature can be

determined from the ratio of fluxes at two wavelengths. At temperatures near 10 K, the blackbody spectrum peaks around $300 \mu\text{m}$, so for data taken at 450 and $850 \mu\text{m}$ the Rayleigh-Jeans approximation to the blackbody law cannot be used. The flux ratio therefore depends on the assumed emissivity spectral index and the temperature (Kramer et al. 2003) as:

$$\frac{S_{450}}{S_{850}} = \left(\frac{850}{450}\right)^{3+\beta} \frac{\exp(17\text{K}/T_{\text{dust}}) - 1}{\exp(32\text{K}/T_{\text{dust}}) - 1} \quad (4.4)$$

where $hc/\lambda k$ is 17 K and 32 K at 850 and $450 \mu\text{m}$ respectively.

In order to derive the dust temperature in TMC-1C, we smoothed both SCUBA maps to the same $14''$ resolution. Because the 450 and $850 \mu\text{m}$ SCUBA maps both have such high signal to noise, we were able to determine the temperature independently at each $14'' \times 14''$ pixel and make a detailed temperature map, assuming a constant value for β throughout the core¹. By estimating a temperature at each point in TMC-1C from our observations, we can calculate self-consistent profiles for column density and mass. A map of the derived dust temperature is shown in Figure 4.3. The derived dust temperatures range from 6 K to 15 K.

4.3.3 Calculation of Extinction

Given the dust color temperature at each position, the column density can be calculated from the observed flux, and from this, the equivalent visual extinction can be estimated. Equation 4.1 can be rearranged to determine the column density from the observed flux and derived temperature.

$$N_H = \frac{S_\lambda}{\Omega B_\lambda(T_d) \kappa_\lambda \mu m_H} \quad (4.5)$$

The equivalent extinction is given by

$$A_V = N_H \frac{E(B - V)}{N_H} \frac{A_V}{E(B - V)} \quad (4.6)$$

$$A_V = 5.3 \times 10^{-22} N_H \quad (4.7)$$

where $N_H/E(B - V) = 5.8 \times 10^{21} \text{ cm}^{-2}$ is the conversion between column density of hydrogen nuclei (for our assumed gas to dust ratio) and the selective absorption, and $R_V = A_V/E(B - V) = 3.1$ is the ratio of total-to-selective extinction (Mathis

¹This restriction is relaxed in Section 4.3.4.

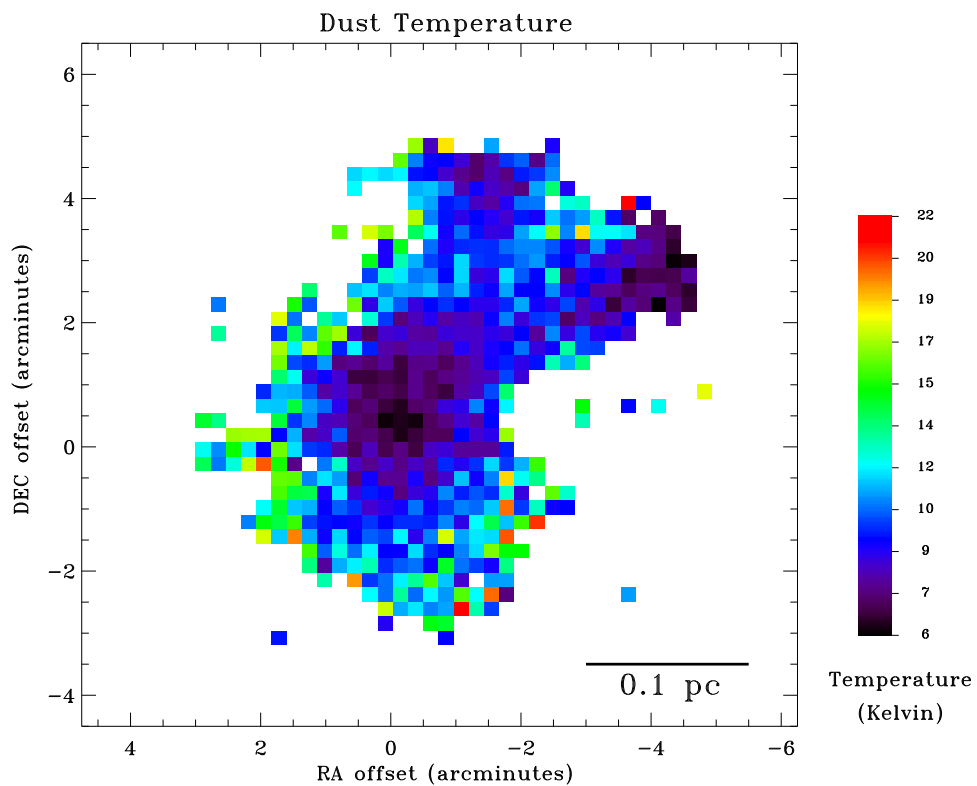


Figure 4.3.— Dust temperature derived from the 450 and 850 μ m SCUBA maps with the choice of $\beta = 1.5$.

1990; Bohlin et al. 1978). Note that this value of R_V assumes a particular “color” for the absorbing dust, which may be different from core to core, or even within a single core. The extinction map created using these assumptions, and the value of κ in Section 4.3.1, is shown in Figure 4.4. The derived extinction reaches a value of ~ 50 mag A_V at the center of the map. A map of the derived column density is shown in Figure 4.4.

4.3.4 Derivation of the Emissivity Spectral Index

Instead of assuming a constant value of β to calculate the temperature map as in Section 4.3.2, one can alternatively calculate the value of the emissivity spectral index at each point in the map by choosing a constant value for the temperature. Using multi-transition spectral line data, Tafalla et al. (2002) find that the core L1544 has a constant *gas* temperature of approximately 10 K (with spatial resolution of ~ 0.03 pc), so experimenting here with calculations involving a constant *dust* temperature is justified. Because the emissivity spectral index appears in the equations used to derive the temperature and mass of a core, knowledge of its variability within a core is clearly valuable to the understanding of the physical properties of TMC-1C and cores in general. β depends on the dust grain size distribution, the composition of the mantle, and the surface area to volume ratio of the dust particles, all of which can vary throughout a core (Ossenkopf & Henning 1994).

The derived emissivity spectral index map for $T = 10$ K at all radii is shown in Figure 4.5. In the central $2'$ (~ 0.08 pc) of the TMC-1C core, the value of β takes values in the physically plausible range $0.5 \leq \beta \leq 2.0$. To self-consistently determine the column density, temperature, and emissivity spectral index of the dust simultaneously, we would need at least one more continuum map at another wavelength. For the remainder of this paper we will assume that β has a constant value and that the dust temperature in TMC-1C is not fixed, unless stated otherwise, although we understand that both quantities are likely to vary throughout the core.

4.3.5 Calculation of Mass

For optically thin emission, Equation 4.1 can be rearranged to convert a measurement of dust emission to mass, so that

$$M = \Omega \mu m_H N_H d^2 = \frac{S_\lambda d^2}{\kappa_\lambda B_\lambda(T_d)} \quad (4.8)$$

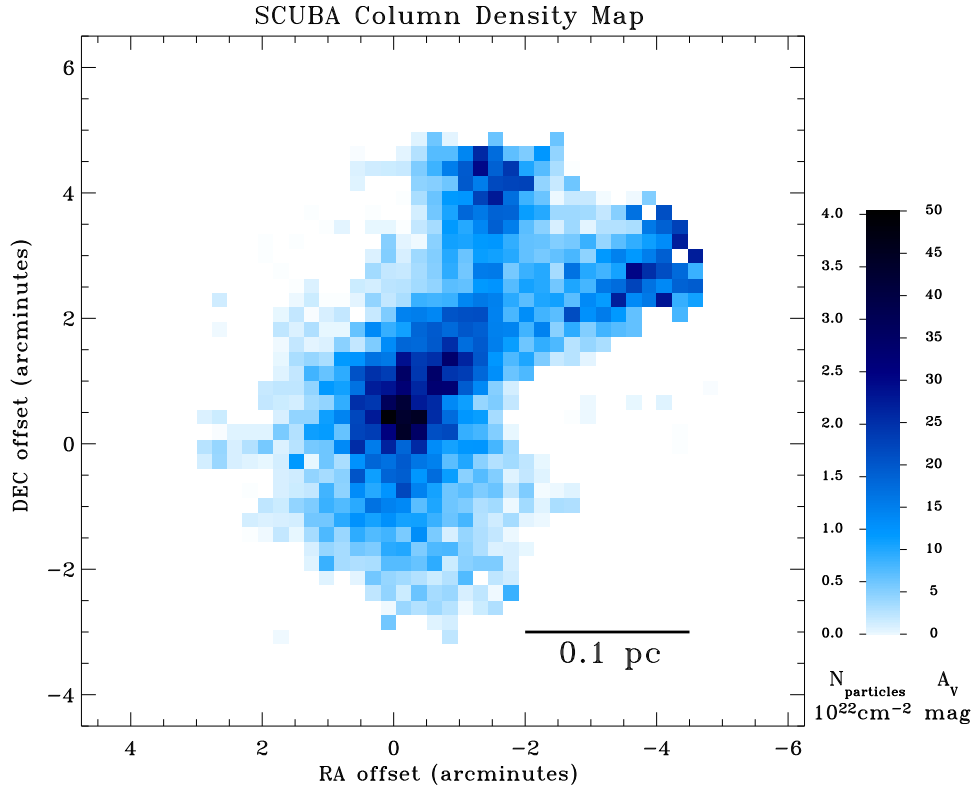


Figure 4.4.— Column density derived from the 450 and 850 μm SCUBA maps with the choice of $\beta = 1.5$. The column density of particles is given by $N_{\text{particles}} = N_{\text{H}}/2.33$, where N_{H} is derived as in Section 4.3.3.

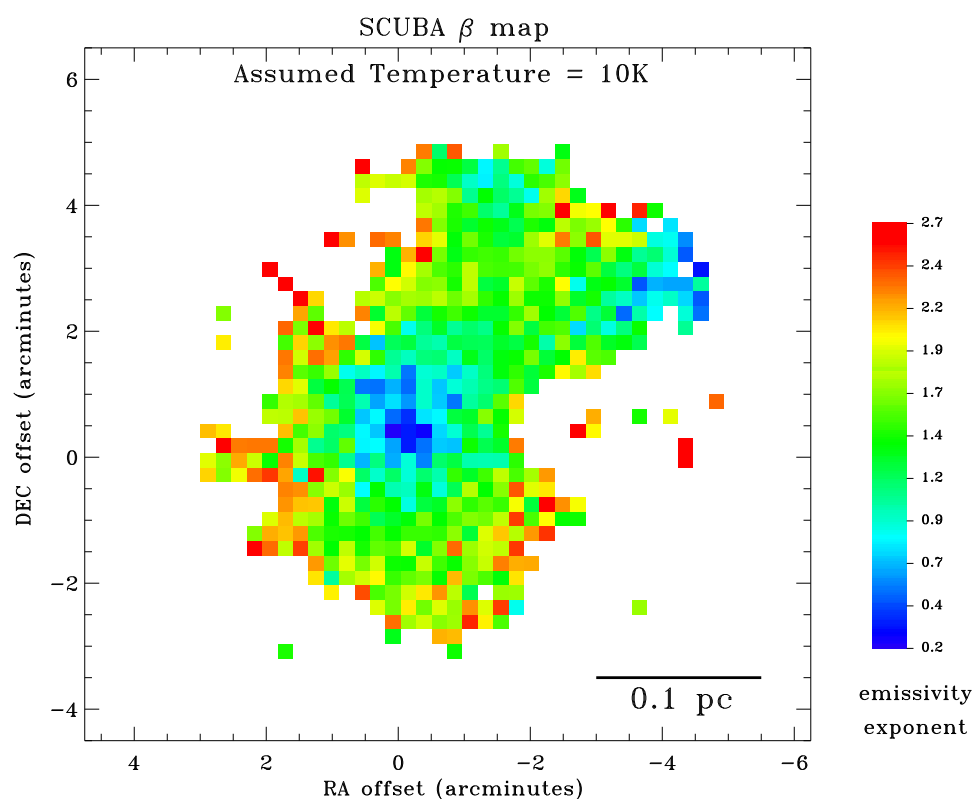


Figure 4.5.— Emissivity Spectral Index (β) of the dust as determined by the 450 and 850 μm SCUBA maps with the assumption that the dust temperature is constant at 10K.

where M is the mass of an emitting volume and d is the distance to it. Using the conversions given above and assuming a distance to Taurus of 140 pc, this equation is equivalent to

$$M = 8.29 \times 10^{-3} S_{450} \left[\exp \left(\frac{32 \text{ K}}{T_d} \right) - 1 \right] \left(\frac{\kappa_{450}}{0.026 \text{ cm}^2 \text{ g}^{-1}} \right)^{-1} \left(\frac{d}{140 \text{ pc}} \right)^2 M_{\odot} \quad (4.9)$$

or

$$M = 0.145 S_{850} \left[\exp \left(\frac{17 \text{ K}}{T_d} \right) - 1 \right] \left(\frac{\kappa_{850}}{0.01 \text{ cm}^2 \text{ g}^{-1}} \right)^{-1} \left(\frac{d}{140 \text{ pc}} \right)^2 M_{\odot} \quad (4.10)$$

The mass contained in each $14'' \times 14''$ pixel is determined by Equations 4.9 and 4.10. Figure 4.6 shows the mass profile calculated by adding the mass in each pixel to annuli concentric around the peak column density. The mass in each pixel is determined using the 850 μm flux in each pixel and either the temperature assigned to each pixel shown in Figure 4.3 (the curve labeled “Actual Temperature Profile”), or a constant temperature assigned to every pixel. The total mass contained within a given radius of the TMC-1C column density peak can be converted into a density profile, assuming a three dimensional geometry, as discussed below.

4.3.6 Temperature and Density Profiles

Under the assumption of spherical symmetry, we can create three dimensional temperature and density profiles from the 850 and 450 μm maps. To make the profiles, we break up the inner $2.2'$ of TMC-1C into $14''$ wide concentric annuli, centered on the position of the extinction peak. The outermost annulus only has flux contributed to it by the outermost spherical shell, and its temperature and density can be calculated as in Sections 4.3.2 and 4.3.5. The next annulus in receives flux from the two outermost spherical shells. After subtracting the flux contributed from the outermost shell, whose temperature and mass have already been calculated, the remaining flux at 450 and 850 μm comes from the second spherical shell, allowing its temperature and density to be derived. In this manner we are able to work our way from the outside of TMC-1C in, finding the temperature and density of each spherical shell. The procedure is very similar to that described in David et al. (2001) for the Hydra A cluster of galaxies.

In Section 4.3.5, the mass was calculated for each element in the map independently of its neighbors by assuming that a single temperature could be assigned to the entire column of material. In this section, instead of dividing the central $2.2'$ of TMC-1C into isothermal cylinders, we break it up into isothermal

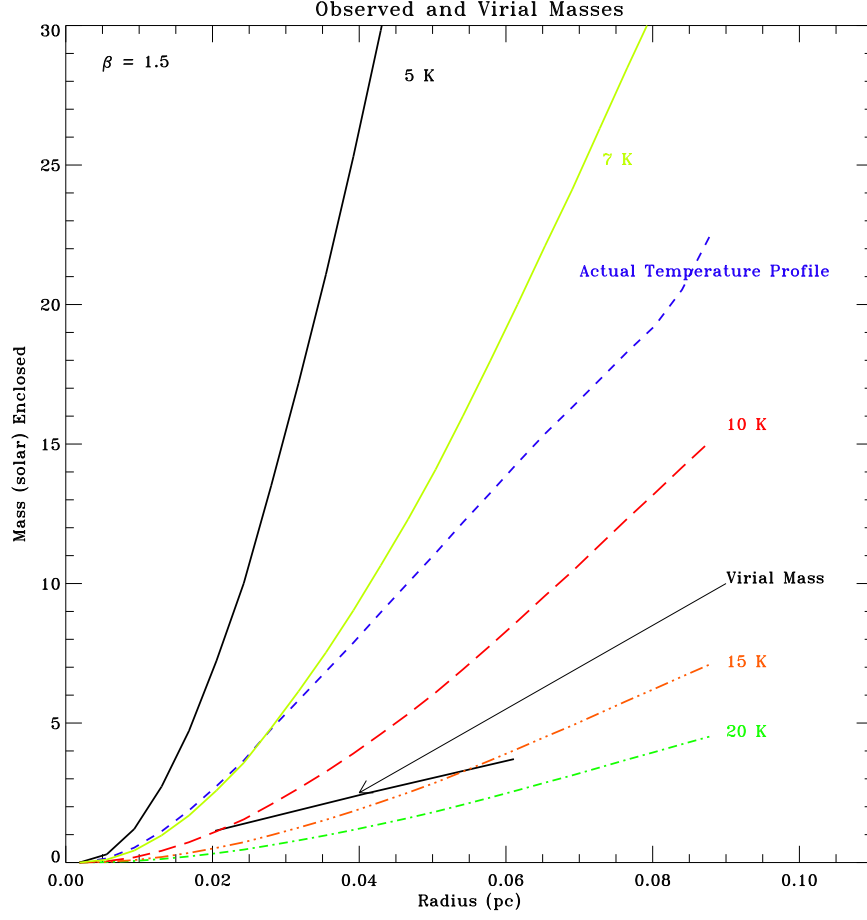


Figure 4.6.— The masses plotted here are those contained within a given radius of the central sub-mm extinction peak. The “virial mass” derived from the N_2H^+ (1-0) line width is plotted (assuming a uniform density profile and constant temperature of 10 K), as is the mass derived from the 850 μm SCUBA map coupled with the “actual temperature profile,” and the masses that would have been derived assuming *various constant temperatures* and the 850 μm data alone.

spherical shells. The temperature and density profiles are fit by broken power laws. Each broken power law is described by five parameters: two coefficients (for normalization), two exponents (the slopes), and the break radius (where the two lines meet). The temperature and density profiles created in this way are shown in Figure 4.7.

The derived temperature profile agrees well with the theoretical temperature profile of an externally heated Bonnor Ebert sphere presented in Gonçalves et al. (2004), as well as the observed dust temperature profile of L183 (Pagani et al. 2004). Outside the break radius, the density profile of TMC-1C derived from the SCUBA data is similar to density profiles derived from N_2H^+ data and continuum dust emission of other starless cores (Table 4.2). Inside the break radius, TMC-1C has a considerably shallower density profile than these other starless cores. The starless cores to which we are comparing TMC-1C did not have their density profiles determined with the same concentric ring algorithm as used here, because researchers lacked the data to make the detailed temperature map that we were able to get from SCUBA. The power law slopes of the density profiles of these other cores can be thought of as isothermal approximations to the “true” density profile. For comparison, the powerlaw fit to the density profile of TMC-1C under the assumption of a constant $T_{\text{dust}} = 10$ K and using only the 850 μm flux is also shown in Figure 4.8, with the broken powerlaw fit shown in Table 4.2.

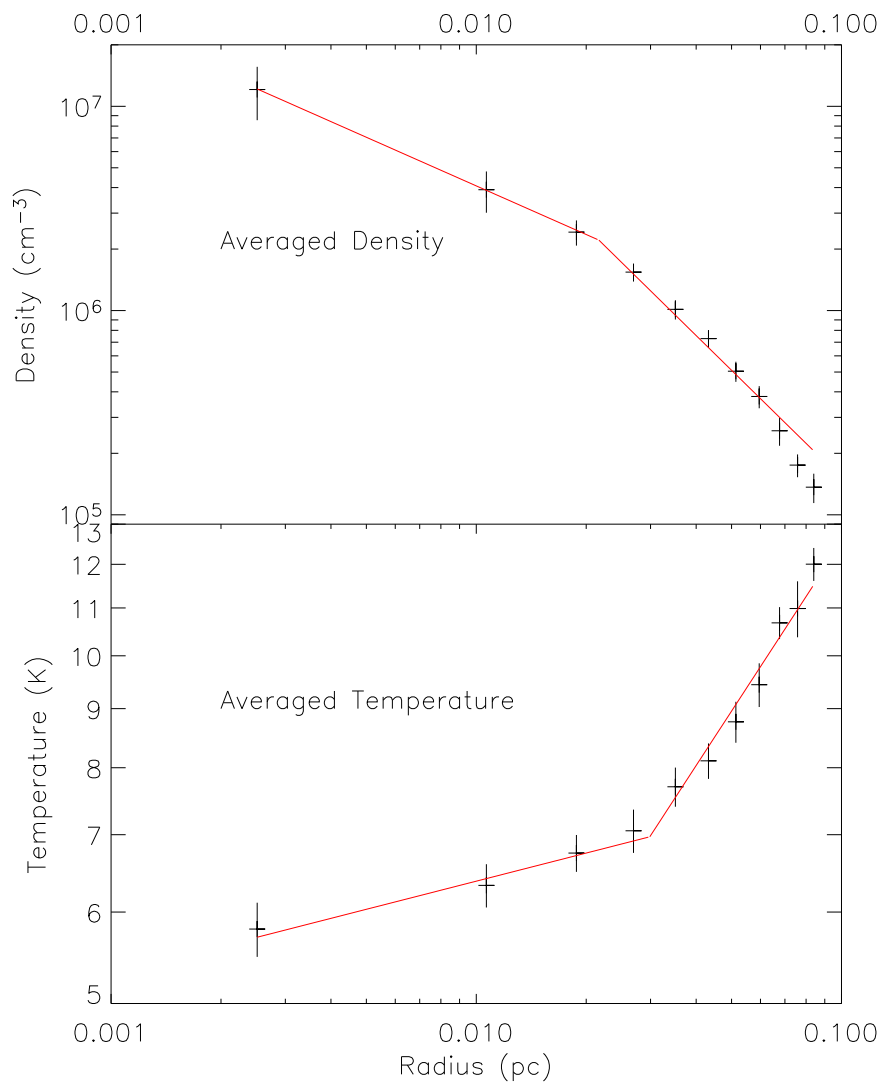


Figure 4.7.— These plots show the dependence of density (top) and temperature (bottom) on radius from the center of TMC-1C, which is assumed to be a sphere. The lines show the best fit broken power law, as described in Section 4.3.6. It is assumed here that $\beta = 1.5$

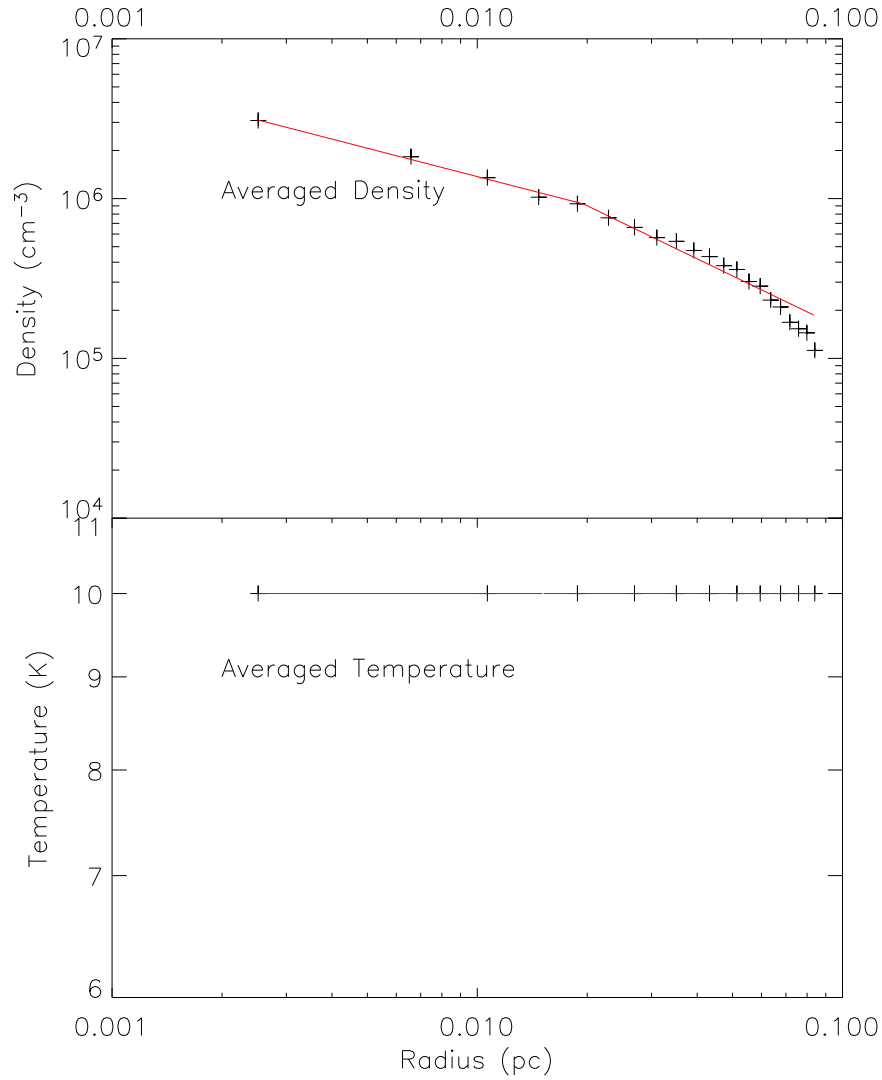


Figure 4.8.— These plots show the dependence of density (top) on radius from the center of TMC-1C, which is assumed to be an isothermal sphere. The density profile is shown in the top panel for comparison with Figure 4.7. The lines show the best fit broken power law, as described in Section 4.3.6. It is assumed here that $\beta = 1.5$

Table 4.2. Density Profiles of Starless Cores

Observation Type	Inner Exponent	Outer Exponent	Break Radius (pc)	Reference
N ₂ H ⁺ starless cores	1.2	2	0.03	1
L1696 sub-millimeter	1.3	2	0.02	2
L1689B sub-millimeter	1.0 - 1.4	2	0.02	3
Sub-millimeter starless cores	1.25	2	0.02	4
TMC-1C sub-millimeter (3D)	0.8 ± 0.1	1.8 ± 0.1	0.02	
TMC-1C sub-millimeter (3D, constant T_{dust})	0.6	1.1	0.02	

References. — (1) (Caselli et al. 2002b); (2) (Ward-Thompson et al. 1999); (3) (Andre et al. 1996); (4) (Ward-Thompson et al. 1994)

4.4 Virial Mass and Infall

The balance between outward turbulent and thermal pressures and inward gravitational pull determines the stability of a dense core. In this section we derive the virial mass from N_2H^+ data and show that for a wide range of density profiles and shapes the virial mass is significantly *lower* than the mass derived from dust emission. The N_2H^+ emission peaks in the same place that the dust column density peaks, so using this line to estimate the virial mass is justified. The N_2H^+ self-absorption profile shows evidence of infall motions, further suggesting the gravitational instability of TMC-1C (Schnee et al. 2006b).

4.4.1 Calculation of the Virial Mass

The virial mass of the inner core of TMC-1C can be estimated from the observed line width of the isolated component of the N_2H^+ spectra. The total velocity dispersion has a non-thermal and a thermal component, given by:

$$\sigma_{TOT}^2 = \sigma_{NT}^2 + \sigma_T^2 \quad (4.11)$$

The thermal velocity dispersion is given by the gas temperature by:

$$\sigma_T^2 = \frac{kT}{\mu_{tracer}} \quad (4.12)$$

The line width depends on the velocity dispersion as:

$$\Delta V = \sqrt{8 \ln 2} \sigma_{TOT} \quad (4.13)$$

Where σ_{TOT} is the total velocity dispersion, σ_{NT} is the non-thermal component of the velocity dispersion, σ_T is the thermal component of the velocity dispersion, k is the Boltzmann constant, T is the gas temperature (assumed to be 10 K, (Tafalla et al. 2002)), μ_{tracer} is the mass of the molecule (N_2H^+ or H_2), and ΔV is the observed line width. Note that the dust temperature is below 10 K throughout most of the TMC-1C core, so the virial mass calculated for a 10 K gas is an upper limit, if the gas and dust temperatures are coupled.

The N_2H^+ spectra were annularly averaged with bins of $20''$, and the line width was then determined as a function of distance from the core's center. The N_2H^+ line width is $\sim 0.25 \text{ km s}^{-1}$, and is very nearly constant at all radii (as expected for

a coherent core). The virial mass of an ellipsoid with a power law density profile determined in this way is

$$M_{\text{vir}} = \frac{5R}{G} \frac{(\Delta v_{\text{tot}}(H_2))^2}{8 \ln 2} \frac{1}{a_1 a_2} \quad (4.14)$$

where Δv_{tot} is the quadratic sum of the 10 K thermal line width of H_2 and the non-thermal line width of N_2H^+ , a_1 is a parameter that depends on the density profile, and a_2 is a parameter that depends on the ellipticity of the core. The virial mass is plotted as a function of radius in Figure 4.6, with the assumptions that the density profile is uniform ($a_1 = 1$) and the core is spherical ($a_2 = 1$). More sophisticated geometric assumptions are discussed in Sections 4.4.1 and 4.4.1.

Dependence on the Density Profile

We have shown in Section 4.3.6 that the density in TMC-1C is not uniform, and our estimate of the virial mass should take this into account. For a given line width, a more centrally condensed cloud will have a lower virial mass than a uniform density cloud (Bertoldi & McKee 1992). This can be parameterized for a power-law density distribution $\rho(r) \propto r^{-k}$

$$a_1 = \frac{(1 - k/3)}{(1 - 2k/5)} \quad (4.15)$$

(Bertoldi & McKee 1992).

The dependence of the virial mass on the density power law is shown in Figure 4.9. For r^{-1} and r^{-2} density distributions, the corrected virial masses are 90% and 60% of the value calculated by Equation 4.15 for a uniform density profile. Thus, the steeper the density profile, the greater the imbalance between the virial mass and the dust derived mass for TMC-1C, making it more unstable.

Dependence on the Shape of the Core

Our estimate of the virial mass also depends on the shape of TMC-1C. It has been shown that many clouds are elliptical in projection, and usually prolate in three dimensions (Myers et al. 1991). Oblate clouds have slightly lower virial masses than a sphere whose radius is determined by the plane-of-sky dimension and a prolate cloud will have a larger virial mass than such a sphere. If the axial ratio, y , is less than 1 (an oblate cloud) then

$$a_2 = \frac{\arcsin(1 - y^2)^{1/2}}{(1 - y^2)^{1/2}} \quad (4.16)$$

If the axial ratio, y , is greater than 1 (a prolate cloud) then

$$a_2 = \frac{\operatorname{arcsinh}(y^2 - 1)^{1/2}}{(y^2 - 1)^{1/2}} \quad (4.17)$$

(Bertoldi & McKee 1992). The dependence of the virial mass on the axial ratio is shown in Figure 4.9. For axial ratios less than 10:1, the correction for the virial mass is less than a factor of ~ 3 . The virial mass as a function of shape and density profile for TMC-1C are shown in Figure 4.10, as are the masses derived from the dust emission for three representative values of β . Notice that to make the virial mass equal to the dust-emission implied mass at 0.06 pc in TMC-1C (see Figure 4.6), a prolate core would need to have an axial ratio of 20:1. This is ruled out by our data, except for the very unlikely case where we are viewing a cigar end-on.

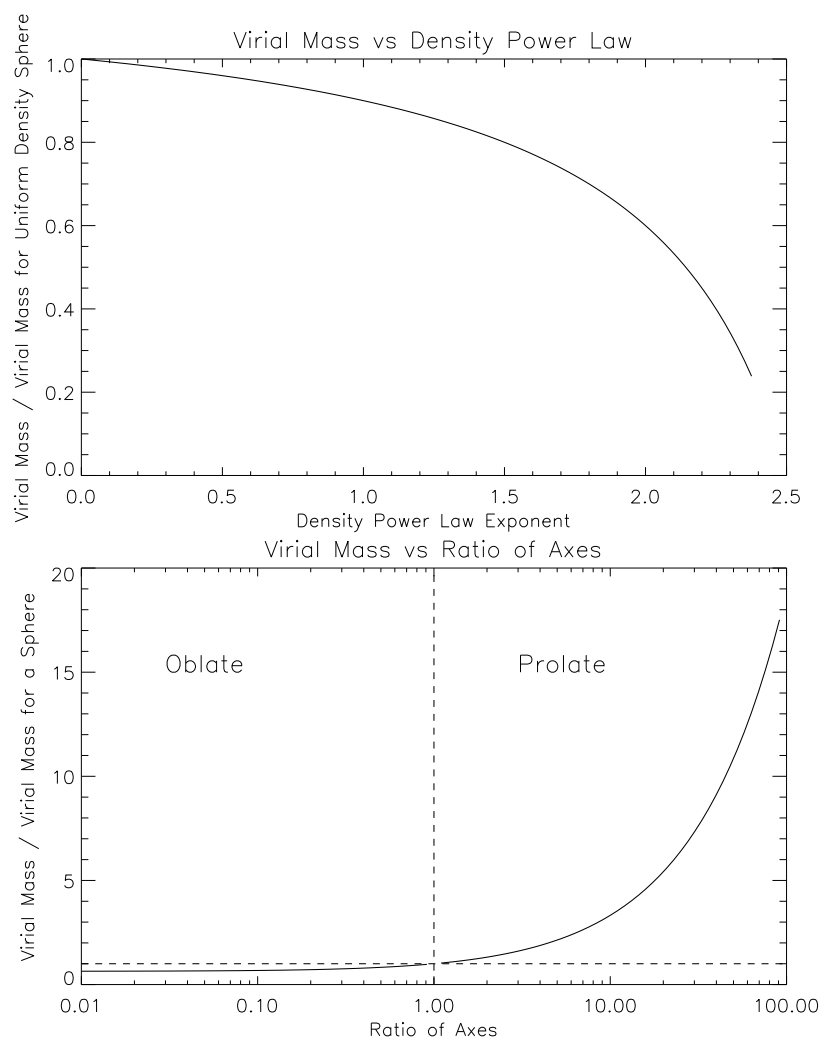


Figure 4.9.— (Top) The dependence of the virial mass on the power law exponent of the density. The virial mass is smaller for more centrally condensed cores. (Bottom) The dependence of the virial mass on the axial ratio of an elliptical core. $x < 1$ is an oblate core, and $x > 1$ is a prolate core. Note that raising the virial mass by a factor of 5 requires a prolate shape with an axial ratio of 20:1 (see Section 4.4.1)

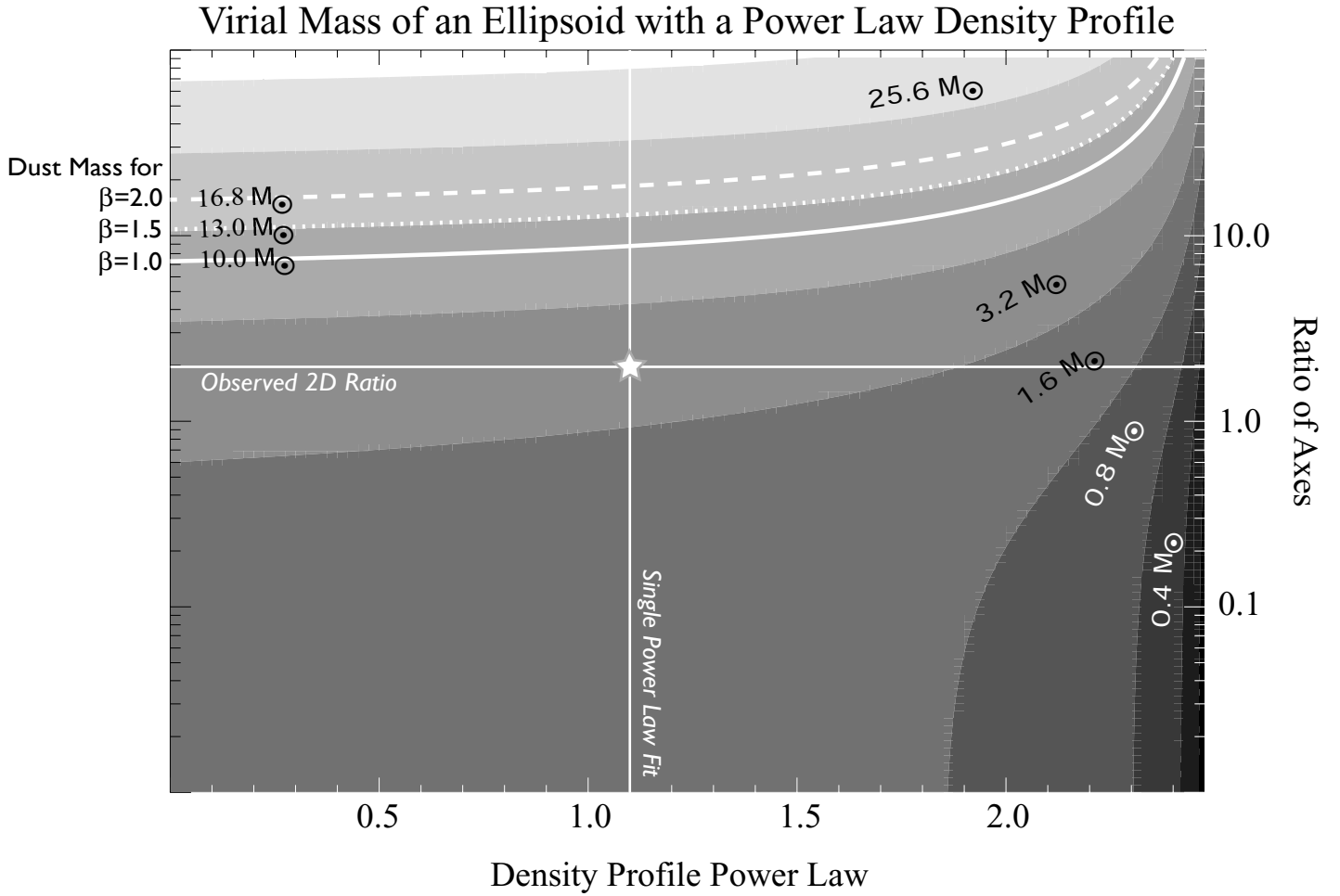


Figure 4.10.— The greyscale shows the dependence of the derived virial mass of TMC-1C contained within the central 0.06 pc of the core on the ellipticity and density power law exponent. The virial mass is calculated with the N_2H^+ linewidth as in Section 4.4.1. The highlighted contours show the mass of TMC-1C contained within the central 0.06 pc of the core derived from dust emission with β taking the values 2.0 (dashed), 1.5 (dotted), and 1.0 (solid). The solid horizontal line shows the approximate prolate axial ratio of TMC-1C as seen in projection. The solid vertical line shows the best fit single power law density profile exponent.

4.4.2 N_2H^+ Self-Absorption

N_2H^+ is typically used as an optically-thin, high-density, low-depletion tracer of the kinematics of the interior of cores (Williams & Myers 1999; Caselli et al. 2002a,b). However, there is some evidence of N_2H^+ self-absorption in dense cores (Caselli et al. 2002b; Williams & Myers 1999). In another paper we will show that N_2H^+ is a better match to the dust emission in TMC-1C than most carbon bearing molecules, which tend to deplete onto dust (Schnee et al. 2006b). In this paper we show evidence of redshifted self-absorption in N_2H^+ at several positions near the peak of the dust emission.

To determine if the splitting of the N_2H^+ hyperfine components is due to self-absorption or two superimposed velocity peaks from different structures along the same line of sight, the seven hyperfine components can be compared with each other to see if the location of the dip is constant amongst them. If this is the case, then kinematics are likely to be creating the non-Gaussian spectra, if not (with the shift increasing with the statistical weight of the component), then self-absorption is probably the cause. The dip in the TMC-1C N_2H^+ spectra does shift with statistical weight in a way consistent with self-absorption, so we believe that the double peaked spectra are not the result of two kinematically distinct clouds. While N_2H^+ self-absorption is uncommon enough to be interesting on its own, we use the N_2H^+ data in this paper to determine infall velocity of material close to the center of the TMC-1C core.

The isolated component of each N_2H^+ spectrum (see Figure 4.2) was fit with two Gaussians (one positive and one negative) to find the approximate velocities for the emission and absorption features, respectively. If the interior of the core is collapsing or flowing toward the center faster than the exterior, then radiative transfer models show that the spectra should have two peaks, with the blue peak higher than the red (Zhou et al. 1993; Myers et al. 1996). Therefore, in an infalling region, the Gaussian fit to emission will be bluer than the Gaussian fit to absorption. In Figure 4.11 we show the histogram of the difference between the emission and absorption velocities for N_2H^+ , where the absorption velocities are nearly all redshifted relative to the emission velocities, indicative of infall. Using the simple two layer radiative transfer model of a contracting cloud developed by Myers et al. (1996), we find that the infall velocity averaged over the central 0.05 pc of TMC-1C is 0.06 km s^{-1} .

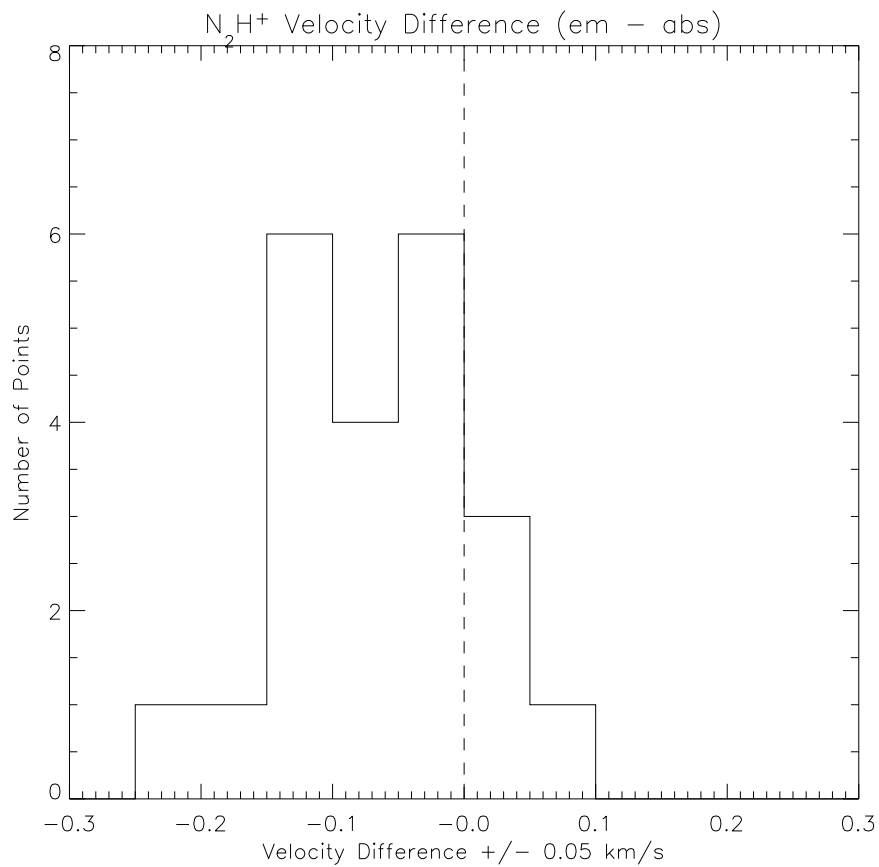


Figure 4.11.— The value of the difference between the velocities of the emission and absorption components of the N₂H⁺ spectra, fit by two Gaussians (see Section 4.4.2).

4.5 Discussion

4.5.1 450 and 850 μm Emission Maps

The 450 and 850 μm maps of TMC-1C look qualitatively different in the lower half of the maps. The 850 μm map has a peak at $(-1', 1')$, though the 450 μm map has no peak there. The 450 μm map peaks at $(0', -1.5')$, where the 850 μm flux is comparatively weak. This suggests that the physical conditions in TMC-1C are different from the pre-protostellar cores L1544 and L1698B, in which the 450 and 850 μm fluxes are well correlated (Shirley et al. 2000).

4.5.2 Temperature Distribution

In order to compare the observed dust temperature in a starless core to theoretical models of externally heated cores, it is necessary to have high quality maps in at least two wavelengths. Our SCUBA maps of TMC-1C provide some of the best available submillimeter data of a starless core. In Figure 4.7 we show that the temperature profile is coldest at the center, with a temperature of ~ 6 K. The temperature rises by ~ 1 K out to 0.03 pc, after which it rises more quickly, to ~ 12 K at a radius of 0.08 pc.

Our observed dust temperature profile is a close match to that shown in Figure 2 of Gonçalves et al. (2004), in both temperature range and shape of the profile. Similarly, our dust temperature profile also matches that in Figure 4b of Evans et al. (2001). Both of these models simulate the temperature profile of externally heated starless cores with Bonnor-Ebert density distributions, which is a reasonable approximation of TMC-1C.

4.5.3 Dependence on β

The parameters describing TMC-1C that we have derived above all assume a constant emissivity spectral index throughout the cloud, although a range of values of β have been tested, between 1.0 and 2.0. We have found that for constant values of β smaller than 1.0, the mass derived from the temperature and the 450 μm flux is not consistent with the mass derived from the temperature and the 850 μm flux. In general, for fits with larger β , the derived mass of the cloud increases and the temperature of the cloud decreases. For a low value of β of 1.0, the virial mass for the inner 0.06 pc of a uniform density sphere is still 2.5 times *less* than the mass

derived from dust emission (see Figure 4.6). So, although the dust derived mass varies strongly with β , the conclusion that the virial mass is smaller than the dust derived mass of TMC-1C is robust (See Figure 4.10).

4.5.4 Dust Emissivity

The emissivity of dust has been measured with a combination of FIR flux maps and NIR extinction maps in the clouds IC 5146 and B68 (Kramer et al. 2003; Bianchi et al. 2003). Both studies find 850 μm fluxes consistent with $\kappa_{850} = 0.01 \text{ cm}^2 \text{ g}^{-1}$, with uncertainties in the range of 30% - 60%. TMC-1C is a starless core similar to B68 and those found in IC 5146, so we estimate that uncertainties in our 450 and 850 μm calibrations (see section 4.2.1) and emissivities result in a derived mass that is accurate to within a factor of 2 for a given emissivity spectral index and dust to gas conversion. The masses we derive from the dust emission are greater than the virial mass by more than a factor of two, so the uncertainty in the dust emissivity can not by itself change the conclusion that TMC-1C should be in a state of collapse. However, a perverse conspiratorial *combination* of β , axial ratio, and κ_ν could still result in a dust mass lower than the N_2H^+ derived virial mass. Figure 4.10 shows contours of the virial mass as a function of ellipticity and density profile, and also plots the mass derived from the 450 and 850 μm fluxes for representative values of β . It is shown that for any density profile and any value of β tested, TMC-1C is gravitationally unstable for a wide range of axial ratios. If TMC-1C has a nearly spherical geometry, then the dust emissivity we use would have to be low by an unlikely factor of ~ 3 -5 to make the virial mass and the dust derived mass approximately equal.

4.5.5 Emissivity Spectral Index

The emissivity spectral index, β , can vary through a core, though it is often treated as a constant in papers on starless cores. By assuming a constant temperature (10 K) and using the 450 μm to 850 μm flux ratio, we have created a map of β (Figure 4.5), in the same way in which the temperature map 4.3 was created. The values of β are closer to zero (i.e. the dust emits more like a blackbody) towards the center of the core than towards the edges. This would be expected if the dust grains are larger at smaller radii in TMC-1C, which might be taken as evidence of grain growth (Testi et al. 2003). On the other hand, it is also plausible that the emissivity spectral index does not change much throughout the core, and instead the temperature of the dust is lower in the center of the TMC-1C than towards the

edges (Zucconi et al. 2001). This would be expected if interstellar radiation is able to heat the exterior of the core, but the extinction is too high in the center to allow for efficient heating there. Note the similarity in the dust temperature map (Figure 4.3) and the emissivity spectral index map (Figure 4.5). The emissivity spectral index for constant $T = 10$ K has values in the physically plausible range of 0.5 to 2.0 (center to edge, respectively), making it hard to call either the constant β or constant T assumption unreasonable. In order to solve for the dust column density, temperature, and emissivity spectral index we would need a third wavelength in our SED.

4.5.6 Mass Estimates With and Without Maps at Multiple Wavelengths

In most SCUBA observations, non-ideal weather degrades the quality of $450\ \mu\text{m}$ data significantly more than the $850\ \mu\text{m}$ data. In such cases, the mass of a core is usually derived from just $850\ \mu\text{m}$ data by assuming that the core is isothermal and assuming a temperature and emissivity spectral index. In TMC-1C, because we can derive a self-consistent temperature map (assuming a value for β) from 850 and $450\ \mu\text{m}$ data, we can also derive the mass as a function of radius without assuming a constant temperature.

Here we compare the mass that we derive from our 450 and $850\ \mu\text{m}$ emission maps with what would ordinarily have been derived from a single wavelength map. The mass that would have been derived from just our $850\ \mu\text{m}$ data and a constant temperature is shown in Figure 4.6 for temperatures of 5, 7, 10, 15, and 20 K. Note that the “true” cumulative mass profile lies somewhere between the 5 K and 10 K constant temperature mass profiles. To constrain this range further, we use the mass profile, $M(r)$, derived from both the 450 and $850\ \mu\text{m}$ fluxes along with the observed $850\ \mu\text{m}$ cumulative flux profile, $F(r)$, to determine a self-consistent temperature profile, $T(r)$, which is a constant temperature within R . This profile answers the question “Given the total $850\ \mu\text{m}$ flux contained within a cylinder of radius r and the mass contained within that radius, what isothermal temperature would one need to assume to make the mass and flux consistent with each other?” The result is shown in Figure 4.12. The values range from 7 K to match the inner 0.02 pc of a $\beta = 2.0$ cloud to 11 K to match the mass out to 0.09 pc of a $\beta = 1.0$ cloud. This tight range on the allowed values for a uniform temperature dust model to match the mass derived from multiwavelength data demonstrates the difficulty of correctly guessing an appropriate temperature for an isothermal core and shows the importance of having multiple wavelength bands of observations to derive it directly.

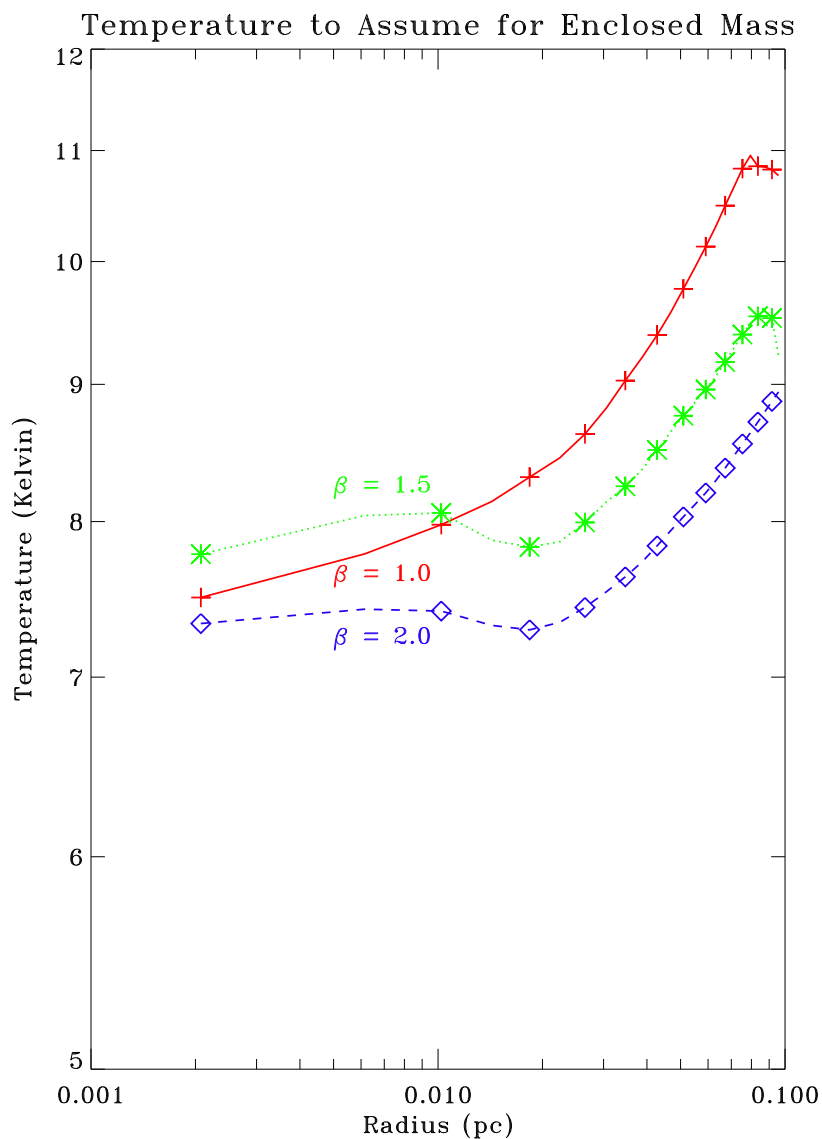


Figure 4.12.— This plot shows the temperature that one would need to assume is constant within radius R in order to correctly derive the mass enclosed within that radius from just the total $850\ \mu\text{m}$ flux within that radius for various values of the emissivity spectral index.

The range of isothermal temperatures typically assumed for cores which do not have multiwavelength data available lies between 30 Kelvin for cores in Orion (Johnstone et al. 2001; Mitchell et al. 2001) and Ophiuchus (Johnstone et al. 2000) to 10 for cold pre-protostellar cores (Shirley et al. 2000). Our analysis of TMC-1C shows that the interior temperature of molecular cloud cores can be significantly colder than these assumed temperatures, as has been recently shown to be the case for other cores as well (Evans et al. 2001). The mass of gas and dust in TMC-1C calculated from the 850 μm flux map for various isothermal cores is plotted in Figure 4.6. If we had assumed that the dust temperature was uniform at 20 K, then the mass derived from the dust emission would be *smaller than the virial mass* for any of the values of β that we considered. A 15 K cloud would have a dust mass nearly equal to the virial mass for $1.0 \leq \beta \leq 2.0$, and a 10 K cloud would have a dust mass considerably higher than the virial mass for all values of β . Because the inferred gravitational stability of a molecular cloud core is highly dependent on the assumed temperature, observations should be made at two or more wavelengths to confidently describe the state of a core.

4.5.7 Observed and Model Profiles

Though we have nowhere required that the resulting temperature, density, or flux profiles of TMC-1C be well fit by powerlaws, for both the temperature and density profiles, broken power laws are good fits to the data². In section 4.4.2 we found the infall velocity implied by the N_2H^+ spectra, without an attempt to explain the physical significance of the fit parameters. In this section we compare the predictions of several popular analytical star formation models with the data in order to predict the evolution of the TMC-1C core. Each model considered is fit to the density shown in Figure 4.7. The fit is done by minimizing the sum of the squared errors between the data values at each radius, and the predicted density at that radius. We have shown that in TMC-1C the inner density profile $n(r) \propto r^{-0.8}$, the outer density profile is $n(r) \propto r^{-1.8}$, and the infall speed is $\sim 0.06 \text{ km s}^{-1}$.

The inside out collapse model of a singular isothermal sphere (Shu 1977) predicts a broken power law density distribution with an r^{-2} profile outside the infall radius, and a profile inside the infall radius asymptotically approaching $r^{-1.5}$. Our observations also show a two-component density distribution, but the inner slope of

²The radius of the innermost point is taken to be one half of the HWHM of the 850 μm beam. Though the location of this point is somewhat arbitrary, its influence on the goodness of fit to the various star formation models is minimal.

the TMC-1C density profile is definitely shallower than predicted by the Shu model. To within the errors (see Table 4.2), the straight-forward inside-out collapse model can be ruled out by the density distribution. In addition, the infall velocity of the inside out collapse is predicted to be around the sound speed ($a = 0.22 \text{ km s}^{-1}$ for 10 K gas), while we have observed an infall speed of only 0.06 km s^{-1} .

The logotrope describes a pressure-truncated, self-gravitating sphere with the equation of state $P/P_c = 1 + A \ln(\rho/\rho_c)$ (McLaughlin & Pudritz 1996). This model predicts a density profile that goes as r^{-1} in the outer parts of cores and much shallower near the center while the core is in equilibrium. Once the cloud begins to contract, an $r^{-1.5}$ profile develops inside the expansion wave. The density profile in TMC-1C outer portions of TMC-1C is considerably steeper than that predicted by the logotropic model, and it is therefore also inconsistent.

In many ambipolar diffusion models (Ciolek & Mouschovias 1994; Basu & Mouschovias 1994), the density of an axisymmetric magnetically regulated cloud can be described by a broken power law. In these models, there is an inner region with a uniform density profile, surrounded by an envelope that has a power law slope ranging from r^{-2} immediately outside the uniform density central region and flattening to a mean $\sim r^{-1.4}$ profile. This qualitatively agrees with our finding for TMC-1C, in that the inner region of the core has a flatter density profile than the outer region, though our derived inner powerlaw slope is significantly shallower than the ambipolar diffusion models predict. Certain ambipolar diffusion models developed to match the conditions (mass, density, rotation, magnetic braking) of the starless core L1544 do a slightly better job of describing TMC-1C than the untailored models. These models predict a steeper profile ($\sim r^{-1.8}$) outside the break radius and a flattened interior profile that match a large portion of the TMC-1C density distribution, but fail to match the inner density point by wide margin (Crutcher et al. 1994; Safier et al. 1997). In the Crutcher model the infall speed is as low as 0.033 km s^{-1} at the boundary of the supercritical core, and as high as 0.133 km s^{-1} near the center ($7 \times 10^{-4} \text{ pc}$). The infall speed in the central arcminute of TMC-1C, as calculated by the N_2H^+ spectra, is roughly 0.06 km s^{-1} , in agreement with this model.

The Larson-Penston model describes the uniform collapse of an isothermal cloud. Like the expansion wave solution of Shu, the density in the outer regions of the cloud goes as r^{-2} , but it has a much flatter profile towards the center. This qualitatively agrees with the observed TMC-1C density profile. The infall velocity in the Larson-Penston model should be $\sim 3.3a$, where a is the sound speed ($a = 0.22 \text{ km s}^{-1}$ for 10 K gas). The TMC-1C infall velocities are far smaller than the $\sim 0.7 \text{ km s}^{-1}$ infall velocity predicted by the Larson-Penston model, and so it too is ruled out.

The Bonnor-Ebert model describes a pressure bounded isothermal sphere, with a density profile that is non-singular at the origin (Ebert 1955; Bonnor 1956). Bonnor-Ebert spheres have a density profile that is close to r^{-2} at large radii, and flattens at smaller radii, similar to the Larson-Penston model (Harvey et al. 2001) and qualitatively in agreement with the TMC-1C density profile. The collapse of a Bonnor-Ebert sphere has been studied numerically by Foster & Chevalier (1993). Once the cloud has begun to collapse, their model predicts an expanding region of supersonic inflow, which asymptotically converges to the Larson-Penston flow. TMC-1C has no evidence of supersonic inflow, so this model fails to describe the core, though a Bonnor-Ebert sphere that is just beginning to collapse would not necessarily be expected to have supersonic infall motions. Furthermore, the density profile of the Bonnor-Ebert sphere is the best fit to the dust-derived density profile for TMC-1C.

A summary of which models can be ruled out, or not, by their predicted density profiles and infall velocities is presented in Table 4.3 and Figure 4.13.

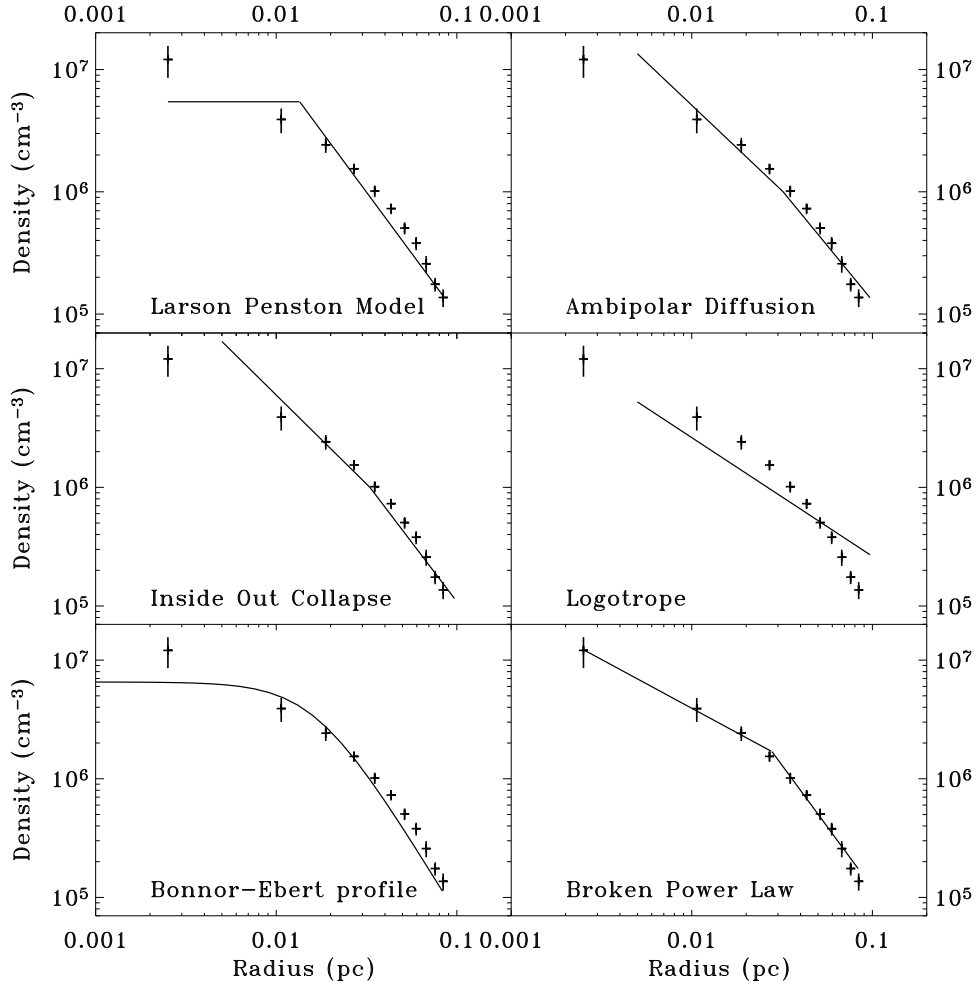


Figure 4.13.— Best fit density profiles for TMC-1C, for various models.

4.6 Summary

4.6.1 450 and 850 μm data

In sub-mm observations, 450 μm data are often degraded by weather far more than 850 μm emission. In this paper we have shown that obtaining high quality 450 μm data, giving us two wavelengths near the thermal peak of TMC-1C's modified blackbody spectrum, is critical to determining the temperature and mass distribution within a pre-stellar core.

4.6.2 Low Temperature

The temperature map shows that TMC-1C has a strong temperature gradient if β is roughly constant, with the inner regions of the core being colder than the outer by roughly a factor of two. This suggests that no point source has formed in TMC-1C to heat the cloud from the inside. The interior temperature of TMC-1C is significantly colder than 10 K for most values of β , and rises to ~ 15 degrees at a radius of 0.1 pc. This temperature range is lower than typically assumed for star forming cores, and leads to a much higher dust and implied gas mass than would have been derived making a “typical” assumption of constant T_{dust} of 15 or 20 K. The temperatures derived for TMC-1C are consistent with theoretical models of pre-protostellar cores heated by an external attenuated radiation field (with or without cosmic rays), which predict cores with a ~ 7 K center heating up to ~ 14 K at the edges (Zucconi et al. 2001; Evans et al. 2001; Galli et al. 2002).

4.6.3 High Mass

The virial mass of TMC-1C has been calculated from the line width of the N_2H^+ transition averaged over several annuli. We show that the total core mass implied by sub-mm dust emission is significantly higher than the virial mass for a wide range of density distributions and axial ratios. The virial mass at a radius of 0.06 pc is shown in Figure 4.10 as a function of the exponent in the density power law and ratio of the axes.

If instead of deriving the temperature from multiwavelength SCUBA data we had used an assumed temperature of 15 K, this conclusion would be far less certain. An assumed constant temperature of 20 K would have led us to conclude that the virial mass is larger than the mass determined from dust emission.

4.6.4 The Effect of Varying Beta

For values of the emissivity spectral index in the range from 1 to 2, the mass of the central 0.06 pc of TMC-1C varies from 9 M_{\odot} to 15 M_{\odot} , as determined by the same method used to create Figure 4.6. Choosing any value of β in this range does not change the conclusion that the dust derived mass is much larger than the virial mass. Furthermore, changing the value of β does not significantly change the shape of the broken power laws that we fit to the temperature and density profile, and therefore does not change our fits to various star formation models. However, using different values of β does change the absolute values of the temperature and density. If β is allowed to vary with radius and if the temperature of TMC-1C is held constant at 10 K throughout the inner 0.06 pc of the core, then the value of β needs to vary by over a factor of ~ 3 to account for observations, increasing towards the edges (see Figure 4.5). In reality, it is likely that β and T_{dust} and N_{dust} all vary with radius, but with only two wavelengths observed, we are forced to hold one quantity fixed to calculate the other two. With observations at a third wavelength, this restriction can be relaxed, and all three quantities (β , T_{dust} , and N_{dust}) can be calculated simultaneously.

4.6.5 Infall Motions Detected

Self-absorbed N_2H^+ spectra show evidence of infall motions of roughly 0.06 $km\ s^{-1}$ over a radius of ~ 0.05 pc. We believe that N_2H^+ is a good tracer of infall in TMC-1C because it is a high density tracer, its shape matches the dust emission near the column density peak, and because it shows no evidence of being significantly depleted. We therefore conclude that the interior of TMC-1C is flowing inwards at about 0.06 $km\ s^{-1}$.

4.6.6 Star Formation Model

TMC-1C is a starless core that is potentially beginning to collapse. Its virial mass is significantly lower than its dust derived mass, and N_2H^+ spectra show signs of sub-sonic infall. The derived density profile behaves qualitatively like that predicted by several star formation models in that it is consistent with an r^{-2} power law outside of its break radius and is shallower interior to the break radius. However, none of the models tested here convincingly match both the density profile and infall velocity that we have measured (see Table 4.3 and Figure 4.13).

A Bonnor-Ebert sphere provides the best fit to our dust-derived density profile, but even for that model the inner point is only barely within the error bars. Do our results mean that all extant detailed models of the collapse of a core into a star are “wrong”? Not completely. The mismatch between theory and observations here is likely caused both by none of the models, on its own, being *exactly* right, *and* remaining assumptions necessary in the data interpretation being imperfect. Perhaps incorporating elements of one theory into another (e.g. ambipolar diffusion in a Bonnor-Ebert sphere) will produce more realistic theories. And, perhaps adding (at least) another wavelength dust map will modify the β , N_{dust} , and T_{dust} distributions (mildly), or other spectral lines tracing material even closer to the dynamical center of cores will reveal (slightly) higher infall speeds. The excellent weather in Hawaii the day we observed TMC-1C has given us some of the tightest constraints yet on the physics of isolated star formation in cores. Now we need to rise to the challenge offered by these fine data.

Acknowledgements

We would like to thank Paola Caselli, Neal Evans, Eric Keto, Charlie Lada, Phil Myers, Ramesh Narayan, and Christopher De Vries for their suggestions, assistance, and insights. We would also like to thank Naomi Ridge for assistance with the manuscript. The James Clerk Maxwell Telescope is operated by The Joint Astronomy Centre on behalf of the Particle Physics and Astronomy Research Council of the United Kingdom, the Netherlands Organisation for Scientific Research, and the National Research Council of Canada.

Table 4.3. Star Formation Models

Model	Density Profile	Infall Velocity
Bonnor Ebert Sphere	not ruled out	not ruled out
Inside Out Collapse	ruled out	ruled out
Larson Penston Model	ruled out	ruled out
Logotrope	ruled out	not ruled out
Ambipolar Diffusion	ruled out	not ruled out

Chapter 5

The Effect of Noise in Dust Emission Maps on the Derivation of Column Density, Temperature and Emissivity Spectral Index

Scott Schnee, Jens Kauffmann, Alyssa Goodman & Frank Bertoldi 2006
submitted to The Astrophysical Journal

Abstract

We have mapped the central $10' \times 10'$ of the dense core TMC-1C at 450, 850 and $1200 \mu\text{m}$ using SCUBA on the James Clerk Maxwell Telescope and MAMBO on the IRAM 30m telescope. We show that although one can, in principle, use images at these wavelengths to map the emissivity spectral index, temperature and column density independently, noise and calibration errors would have to be less than $\sim 2\%$ to accurately derive these three quantities from a set of three emission maps. Because our data are not this free of errors, we use our emission maps to fit the dust temperature and column density assuming a constant value of the emissivity spectral index and explore the effects of noise on the derived physical parameters. We find that the derived extinction values for TMC-1C are large for a starless core ($\sim 80 \text{ mag } A_V$), and the derived temperatures are low ($\sim 6 \text{ K}$) in the densest regions of the core, assuming $\beta = 1.8$.

5.1 Introduction

Efforts to determine the mass and temperature of starless cores from sub-millimeter and millimeter observations are hampered by uncertainties in the emission properties of the dust grains, such as the emissivity spectral index. Although in principle it should be possible to calculate the column density of dust, the emissivity spectral index of the dust, and the dust temperature from observations at three or more wavelengths, in practice this has never been done for a starless core. Such an analysis has been done for circumstellar disks, e.g. (Beckwith & Sargent 1991; Mannings & Emerson 1994; Mathieu et al. 1995). In this paper we explore the levels of uncertainty in the derived dust temperature (T_d), emissivity spectral index (β) and column density (N_H) resulting from datasets of either three or four noisy emission maps at different wavelengths. We then apply this analysis to the starless core TMC-1C.

TMC-1C is a starless core in the Taurus molecular cloud, at an approximate distance of 140 pc (Kenyon et al. 1994). It was shown that TMC-1C is a coherent core, meaning that its velocity dispersion is roughly constant, at slightly more than the sound speed, over a radius of 0.1 pc (Barranco & Goodman 1998; Goodman et al. 1998). The velocity field of TMC-1C shows evidence of solid body rotation, at $0.3 \text{ km s}^{-1} \text{ pc}^{-1}$ (Goodman et al. 1993), and the N_2H^+ spectrum reveals the signature of sub-sonic infall (Schnee & Goodman 2005). The mass derived from 450 and 850 μm maps alone (13 M_\odot) is several times the virial mass, and the density profile is similar to that of a Bonnor-Ebert sphere (Schnee & Goodman 2005).

Here we use data taken with SCUBA (at 450 and 850 μm) and MAMBO (at 1200 μm) to make maps of the dust column density and temperature, and to estimate a constant value for the emissivity spectral index of TMC-1C. Although the high signal to noise at 850 and 1200 μm make this set of maps one of the best yet available for a starless core, we show that the noise is still too high to reliably map variations in the emissivity spectral index of TMC-1C.

5.2 Observations

5.2.1 SCUBA

We observed a $10' \times 10'$ region around TMC-1C using SCUBA (Holland et al. 1999) on the JCMT. Our maps, especially at 450 μm , benefitted from exceptionally stable

grade 1 weather. We used the standard scan-mapping mode, recording the 850 and 450 μm data simultaneously (Pierce-Price et al. 2000; Bianchi et al. 2000). Three chop throw lengths of 30", 44", and 68" were used in both the right ascension and declination directions. The JCMT has FWHM beams of 7.5" at 450 μm and 14" at 850 μm , which subtend diameters of 0.005 and 0.01 pc, respectively, at the distance of Taurus. Pointing during the observations was typically good to 3" or better. The data reduction for the SCUBA data is described by Schnee & Goodman (2005). The absolute flux calibration is uncertain at levels of $\sim 4\%$ at 850 μm and $\sim 12\%$ at 450 μm . The rms noise in the 850 μm map is 8.6 mJy/beam, and 13 mJy/beam in the 450 μm map.

The Emerson2 technique used to reconstruct SCUBA scan maps from its component chop throws introduces false structure that can be removed (Johnstone et al. 2000). To remove this structure, we convolved the SCUBA images (after masking out pixels with $|S| > 5\sigma$) with a Gaussian of FWHM twice the size of the largest chop throw, and subtracted this from the original image, as explained in Reid & Wilson (2005). The resulting image has fluxes nearly identical to the original in regions of high signal to noise, but has fewer bowls of negative emission and other artifacts introduced by chopping and image reconstruction. We only use data from the high signal to noise central region of the maps to estimate the dust properties. We account for the SCUBA error beams by convolving the 850 and 1200 μm maps with the 450 μm PSF, and convolving the 450 and 1200 μm maps with the 850 μm PSF before regridding to a common resolution, as explained in detail in Reid & Wilson (2005).

The original bowls of negative flux in our 450 μm map on either side of region ‘a’ in Figure 5.7 have peak values around -150 mJy, and average values around -75 mJy. We believe that these structures are artifacts of image reconstruction. It is possible that structures of similar magnitude (either positive or negative) might be affecting data elsewhere in the map.

5.2.2 MAMBO

We observed the 1.2 mm continuum emission in November 8, 2002, October 23, 2003, and November 2, 2003 using the 117-channel MAMBO-2 array (Kreysa et al. 1999) at the IRAM 30-meter telescope on Pico Veleta (Spain). The FWHM beam size on the sky was 10".7. The source was mapped on-the-fly, with the telescope subreflector chopping in azimuth by 60" to 70" at a rate of 2 Hz; the total on-target observing time was about 6 hours. The line-of-sight optical depth varied between 0.1 and 0.5. The data were reconstructed using the EKH algorithm in an iterative way

that properly reproduces large-scale emission (Kauffmann et al., in prep.). The flux calibration uncertainty is approximately 10%.

5.3 Solving for physical parameters

In principal, one can use three measured quantities (e.g. the three flux density maps at 450, 850 and 1200 μm) to solve for three unknowns (e.g. maps of the dust temperature, emissivity spectral index, and column density). To compare the fluxes at different wavelengths, the maps must be spatially smoothed to a common resolution of the largest beam, which in our case is $14''$.

The flux density in each map is given by:

$$S_\nu = \Omega B_\nu(T_d) \kappa_\nu \mu m_H N_{H_2}, \quad (5.1)$$

where

$$B_\nu(T_d) = \frac{2h\nu^3}{c^2} \frac{1}{\exp(h\nu/kT_d) - 1} \quad (5.2)$$

and

$$\kappa_\nu = \kappa_{230} \left(\frac{\nu}{230\text{GHz}} \right)^\beta. \quad (5.3)$$

In Equation 5.1, S_ν is the flux density; Ω is the solid angle of the beam; $B_\nu(T_d)$ is the blackbody emission from the dust at temperature T_d ; $\kappa_{230} = 0.009 \text{ cm}^2 \text{ g}^{-1}$ is the emissivity of the dust grains at 230 GHz (Ossenkopf & Henning 1994); m_H is the mass of the hydrogen atom; $\mu = 2.8$ is the mean molecular weight of interstellar material in a molecular cloud per hydrogen molecule, N_{H_2} is the column density of hydrogen molecules, and a gas-to-dust ratio of 100 is assumed. It should be noted that κ_{230} is uncertain by a factor of ~ 2 , and that we assumed that $\kappa_{230} = 0.005$ and $\mu = 2.33$ (which is the mean molecular weight per free particle for an abundance ratio of $N(H)/N(He) = 10$ and negligible metals) in Schnee & Goodman (2005).

The ratio of two fluxes, because of the common beam size, can be simply expressed as:

$$\frac{S_{\nu_1}}{S_{\nu_2}} = \left(\frac{\nu_1}{\nu_2} \right)^{3+\beta} \left(\frac{\exp[h\nu_2/kT_d] - 1}{\exp[h\nu_1/kT_d] - 1} \right) \quad (5.4)$$

The dust temperature can be found independently of the dust emissivity spectral index by taking the difference between the ratio of fluxes, if we assume that each line of sight through the core can be characterized by a single temperature and

emissivity spectral index:

$$\begin{aligned} & \log \left(\frac{S_{450}}{S_{850}} \right) \log \left(\frac{1200 \mu\text{m}}{850 \mu\text{m}} \right) - \\ & \log \left(\frac{S_{850}}{S_{1200}} \right) \log \left(\frac{850 \mu\text{m}}{450 \mu\text{m}} \right) = \\ & \log \left(\frac{\exp [\lambda_T / 850 \mu\text{m}] - 1}{\exp [\lambda_T / 450 \mu\text{m}] - 1} \right) \log \left(\frac{1200 \mu\text{m}}{850 \mu\text{m}} \right) - \\ & \log \left(\frac{\exp [\lambda_T / 1200 \mu\text{m}] - 1}{\exp [\lambda_T / 850 \mu\text{m}] - 1} \right) \log \left(\frac{850 \mu\text{m}}{450 \mu\text{m}} \right), \end{aligned} \quad (5.5)$$

where $\lambda_T = hc/kT_d$.

Once the dust temperature is determined, the emissivity spectral index can be calculated by:

$$\beta = \log \left(\frac{S_{850}}{S_{1200}} \frac{\exp [\lambda_T / 850 \mu\text{m}] - 1}{\exp [\lambda_T / 1200 \mu\text{m}] - 1} \right) / \log \left(\frac{1200 \mu\text{m}}{850 \mu\text{m}} \right) - 3. \quad (5.6)$$

The column density of dust can be derived from the flux at a single wavelength (eg. at 1200 μm), the temperature of the dust and the emissivity spectral index of the dust using Equation 5.1. The equivalent visual extinction can be calculated from the column density N_H using:

$$A_V = N_H R_V \frac{E(B - V)}{N_H} \quad (5.7)$$

where $N_H = 2 \times N_{H_2}$, $N_H/E(B - V) = 5.8 \times 10^{21} \text{ cm}^{-2} \text{ mag}^{-1}$ is the conversion between column density of hydrogen nuclei (for our assumed gas to dust ratio) and the selective absorption, and $R_V = A_V/E(B - V) = 3.1$ is the ratio of total-to-selective extinction (Mathis 1990; Bohlin et al. 1978). Although we use a constant value of R_V , we recognize that this value is uncertain to within a factor of 2, and is just as likely to vary with grain size distribution as β is (McCall 2004).

5.4 Error Analysis

In order to understand how the noise and reconstruction artifacts in our emission maps will effect the accuracy of our derived dust temperature, emissivity spectral index and column density we have run a variety of Monte Carlo simulations. We compare the effects of using maps at three particular wavelengths to solve for all three parameters to using the three measurements to fit for two parameters while assuming a fixed value for the third. We also show the improvements brought about by using a fourth wavelength and fitting for all three physical parameters.

5.4.1 Illustrative Examples

Here we discuss the uncertainties be expected from solving for T_d , β and N_H from three emission maps that have noise or whose calibration is uncertain. To illustrate the method, Figure 5.1 shows the modified blackbody spectrum from dust with $A_V = 50$, $T_d = 10$ K and $\beta = 1.5$. The black dotted line shows the true emission spectrum, with crosses at 450, 850 or 1200 μm , and the blue/red crosses show the flux overestimated/underestimated at one wavelength by 20%. The blue and red curves are the fitted spectra that pass through the one blue/red cross and the two black crosses. It is clear that a 20% error in one measurement creates errors in all three derived parameters that are much larger than 20%. The derived values of T_d , β and N_H are labeled in Figure 5.1. For convenience, we show the derived N_H in units of A_V .

As can be seen from Equation 5.5, noise in any of the three flux maps first translates into uncertainty in the derived temperature. This incorrect value of T_d , along with any noise in the 850 and 1200 μm maps then results in uncertainties in the derived values of β and N_H . From Equation 5.6, one can show that overestimating the temperature will result in an underestimate of β , and underestimating the temperature will result in an overestimate of β . The errors in the derived parameters from incorrectly measuring the flux at one wavelength, while correctly measuring the flux at the other two wavelengths is shown in Figure 5.2. The anti-correlation between T_d and β is clearly seen. Also apparent is that for dust with “core-like” values of β , T_d and N_H , errors in 450 μm flux result in smaller errors in the derived physical parameters than errors at 850 and 1200 μm , which is convenient because the 450 μm maps often suffer from higher levels of noise than maps at 850 and 1200 μm .

5.4.2 Deriving the Physical Parameters

In order to determine the effect of similar levels of noise in all three wavelengths on the three derived physical parameters, we determine the flux at 450, 850 and 1200 μm from dust at $T_d = 10, 15$ and 20 K and $\beta = 1.0, 1.5$ and 2.0. The fluxes are then modified by a multiplicative factor $f = 1.0 + \delta$ where δ is randomly chosen from a normal distribution of mean zero and standard deviation σ , and each flux is modified by a different f . This is repeated 10,000 times for each value of σ between 0 and 0.2. We show the effect of noise in all three wavelengths on the derived column density, temperature and emissivity spectral index in Figure 5.3. At a signal to noise of 20 (5% error), the expected uncertainties in the derived N_H , T_d and β are

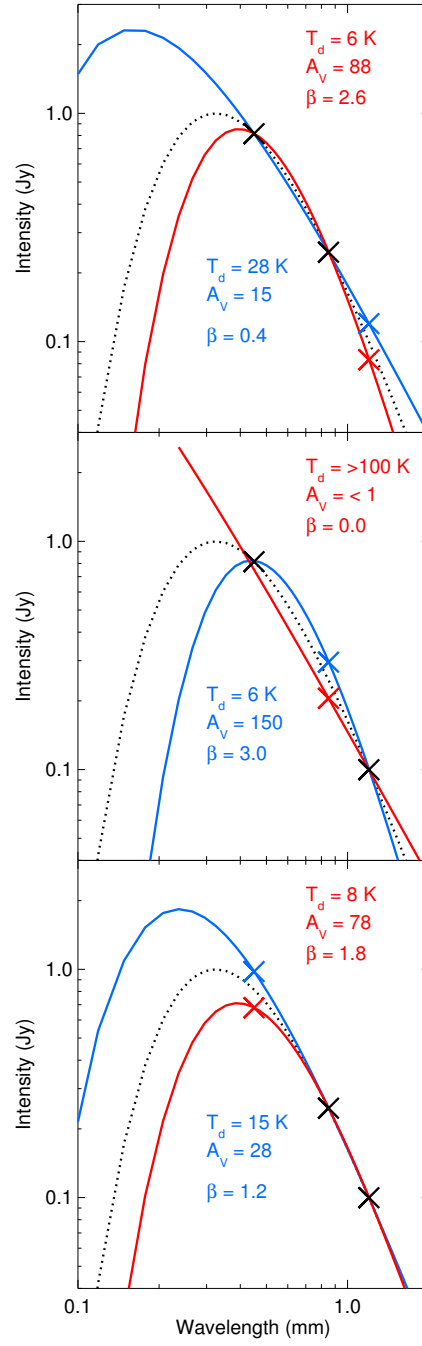


Figure 5.1.— The true and calculated modified blackbody spectra of material with $A_V = 50$, $\beta = 1.5$ and $T_d = 10$ K. The black curve shows the true spectrum, and the black crosses show the flux at 450, 850 or 1200 μm . The blue and red crosses show the flux overestimated or underestimated, respectively, by 20%. The blue and red curves show the spectrum of dust that passes through the blue/red cross and the two black crosses. The dust temperature, emissivity spectral index and column density that would be derived from the three data points are also shown.

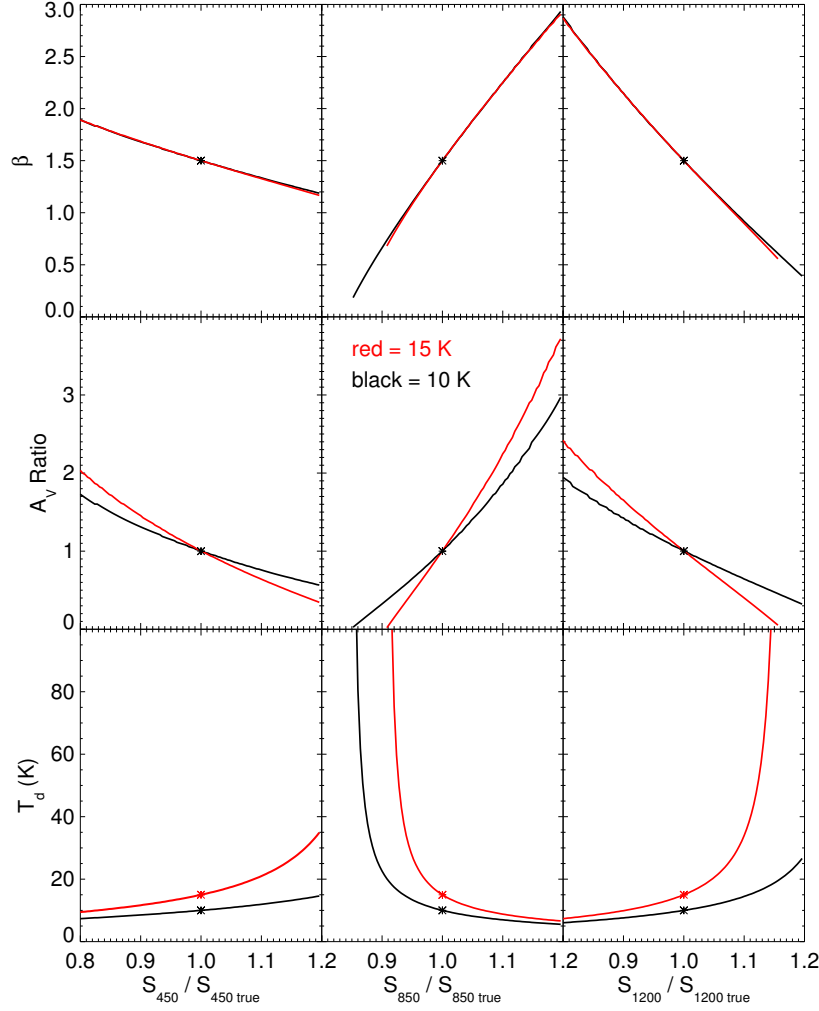


Figure 5.2.— The derived emissivity spectral index (β), the ratio of the derived column density to the true column density and the derived temperature as functions of the ratio of the measured flux to the true flux at one wavelength (450, 850 or 1200 μm), with the other two fluxes measured without error. The black and red curves show the results for dust with $T_d = 10 \text{ K}$ and $T_d = 15 \text{ K}$, respectively. $\beta = 1.5$ in both cases. The curves are cut off where the derived temperature is greater than 100 K.

approximately 50%, 80% and 40%, respectively, for 15 K dust with $\beta = 1.5$. The median values of the derived parameters stay close to the input values at every value of T_d and β tested.

Although even just 5% errors in the measured fluxes at three wavelengths make accurate determinations of three physical parameters impossible, adding a fourth wavelength (for instance, at 350 μm or 2.7 mm) drastically reduces the effects of noise. At least one of the observations should not be on the Rayleigh-Jeans portion of the emission spectrum, or else T_d and N_H will be degenerate in the fit. For dust at $T_d = 10, 15$ and 20 K and $\beta = 1.0, 1.5$ and 2.0 we calculate the flux at 350, 450, 850 and 1200 μm . As before, the fluxes are then modified by a multiplicative factor $f = 1.0 + \delta$, where δ is again a variable randomly chosen from a normal distribution with mean zero and standard deviation σ . This is repeated 10,000 times for each value of σ between 0 and 0.5. We allow σ to be larger than in the previous Monte Carlo simulation because the effects of noise are smaller in this case. For each set of four fluxes, the column density, temperature and emissivity spectral index are fit and the results are shown in Figure 5.4. At a signal to noise of 20 (5% error), the expected errors in the column density, temperature and emissivity spectral index are all on the order of $\sim 1\%$. As the signal to noise gets lower, the median derived temperature and column density decrease, and this effect is larger for warmer cores.

5.4.3 Fixing One Parameter

In the case of a starless core observed at three wavelengths, one can hold one parameter fixed, such as assuming a constant $T_d = 15$ K or $\beta = 1.5$, and use the three flux measurements to fit the remaining two parameters. Figure 5.5 shows the result of using noisy flux measurements to fit the column density and either the dust temperature or the emissivity spectral index of a core with $T_d = 15$ K and $\beta = 1.5$. We show the results for correctly assuming that $\beta = 1.5$ and erroneously assuming that $\beta = 2.0$ or 1.0, as well as for correctly assuming that $T_d = 15$ K and erroneously assuming that $T_d = 10$ or 20 K.

We see that by choosing the correct value of β and fitting the T_d and N_H , noise in the emission maps on the level of 10% result in $\sim 1\%$ uncertainties in the derived temperature and column density. Choosing a value of $\beta = 1.0$, when the proper value is $\beta = 1.5$ results in temperatures that are on average 3 K too high, with a spread of ~ 3 K, and column densities that are high by 8%. Overestimating the emissivity spectral index, by assuming that $\beta = 2.0$, results in temperatures that are on average 2 K too low and column densities that are 5% low.

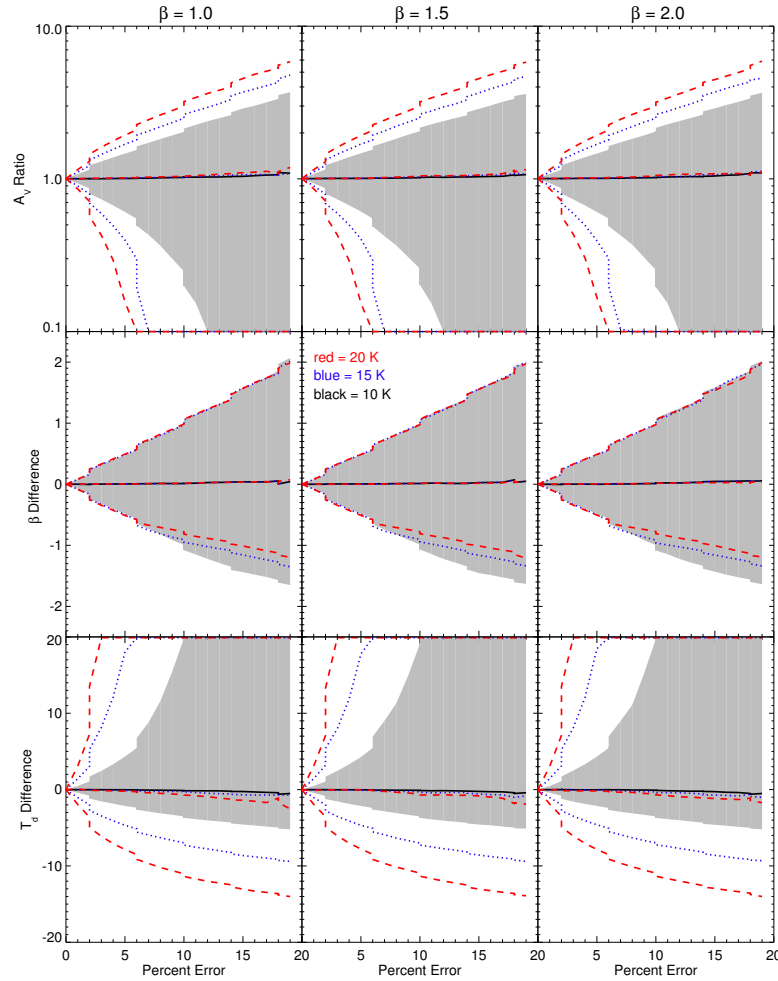


Figure 5.3.— Each panel shows the 1σ spread in the derived column density, temperature or emissivity spectral index as a function of the percent noise in all three flux maps at 450, 850 and 1200 μm . A 5% error in the measured flux corresponds to a signal to noise of 20. The black line shows the median value for the derived parameter, and the greyed area shows the 1σ spread in that parameter for dust at 10 K. The blue (dotted) and red (dashed) lines show the median value and 1σ spread for dust at 15 and 20 K, respectively, and each panel is repeated for emissivity spectral index ($\beta = 1.0, 1.5$ or 2.0). N_H , T_d and β are derived as in Section 5.3. The column density is plotted as the ratio of the derived A_V to the input A_V , and the temperature and emissivity spectral index are plotted as the difference between the derived parameter and the true value.

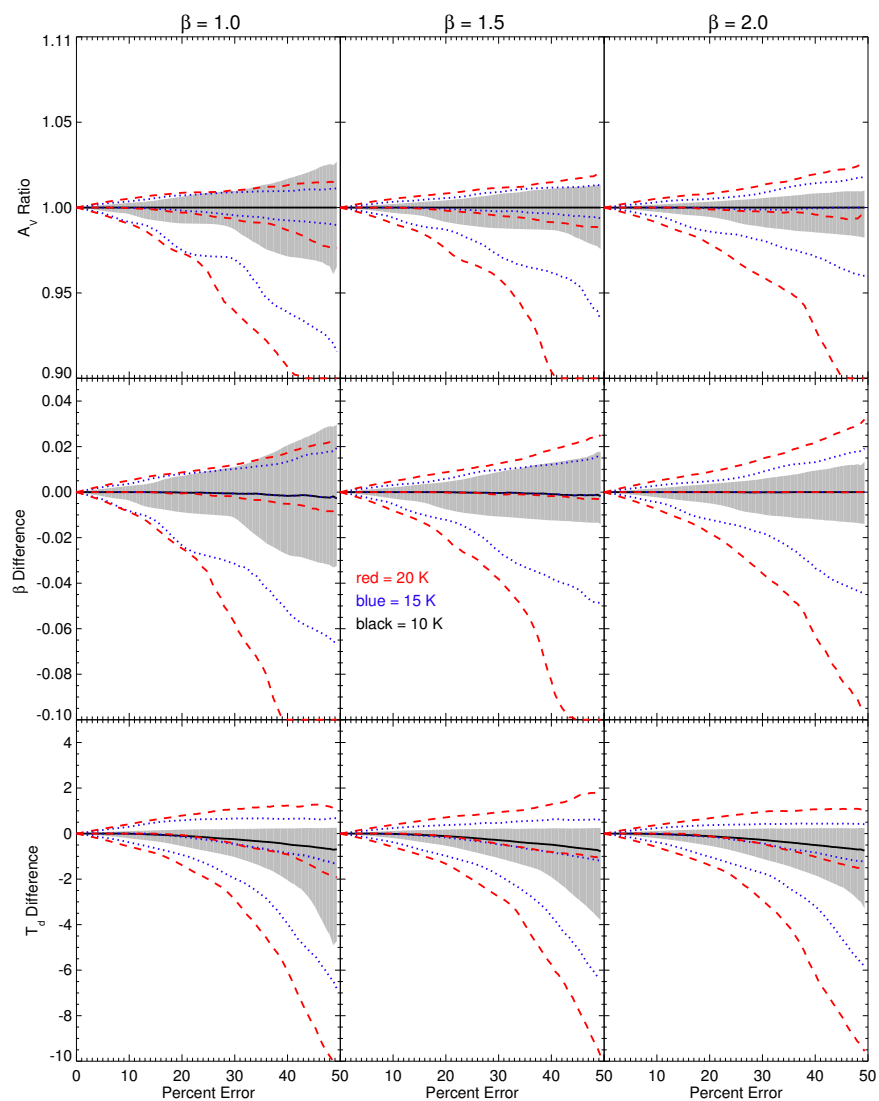


Figure 5.4.— Same as Figure 5.3, except N_H , T_d and β are fit from *four* observations at 350, 450, 850 and 1200 μm .

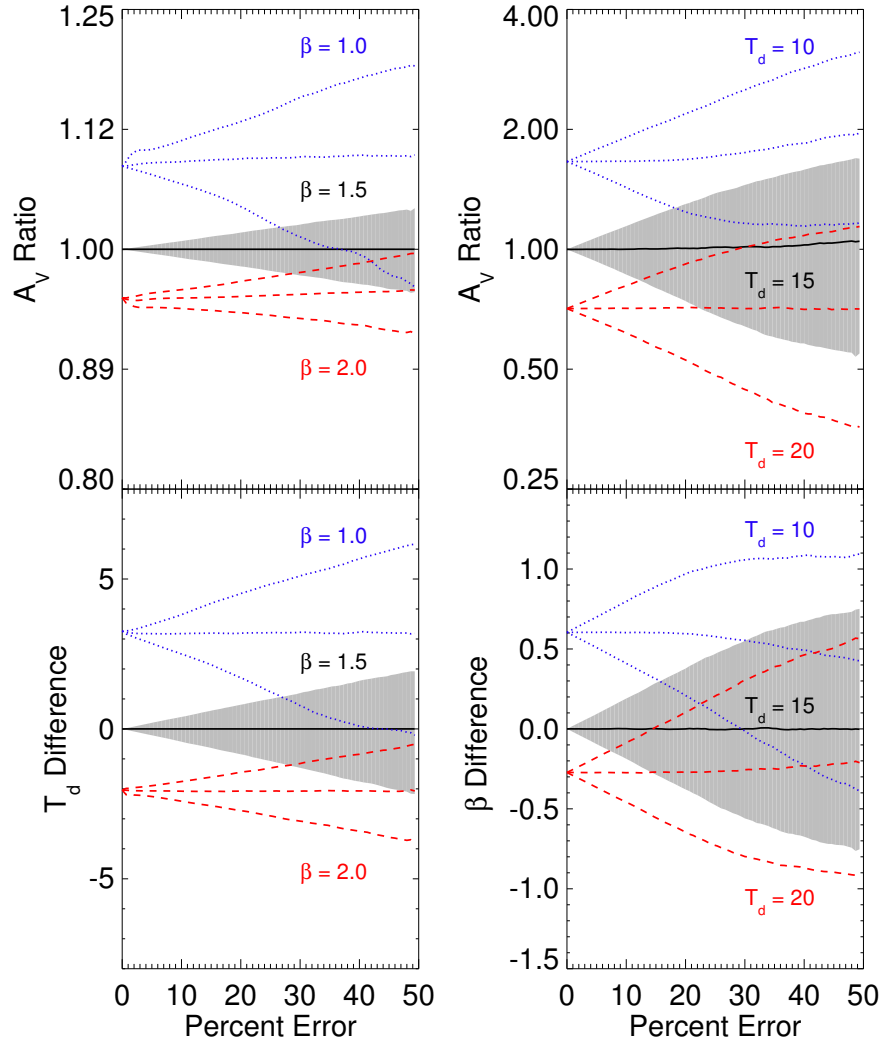


Figure 5.5.— Each panel shows the 1 σ spread in the derived T_d , β and N_H for dust at $T_d = 15$ K and $\beta = 1.5$ from a least squares fit between the predicted and given fluxes at 450, 850 and 1200 μm . The grey area uses the correct assumption that $\beta = 1.5$ or $T_d = 15$, while the blue (dotted) and red (dashed) lines incorrectly assume that $\beta = 1.0$ and $\beta = 2.0$, or $T_d = 10$ and $T_d = 20$, respectively.

Figure 5.5 shows that by choosing the T_d and fitting for the β and N_H , the true values of β and column density are recovered, on average, with an absolute spread of 0.20 in β and a relative spread of 13% in column when the signal to noise ratio is 10. Underestimating the temperature by assuming $T_d = 10$ K when the proper value is $T_d = 15$ K results in an overestimate of the emissivity spectral index by 0.6, on average, and an overestimate of the column density by 70%. Overestimating the temperature by assuming that $T_d = 20$ K results in an underestimate of β by 0.3, on average, and an underestimate of N_H by a factor of 30%.

5.4.4 A Model Core

To illustrate the error analysis presented in Section 5.4, we present here our data on the starless core TMC-1C. The random noise in the emission maps, as measured in regions with faint emission, is found to be 13 mJy/beam, 9 mJy/beam and 3 mJy/beam, which corresponds to S/N values of 21, 14 and 15 at 450, 850 and 1200 μm at the (0,0) position of the emission maps. Calibration uncertainties are $\sim 12\%$, 4% and 10% at 450, 850 and 1200 μm , respectively.

To determine how the random noise and reconstruction artifacts (which are spatially correlated and therefore not truly random) in the observed emission maps affect the derived parameters, we construct synthetic emission maps of a starless core like TMC-1C. The model core has a temperature and column density profile derived from the two dimensional temperature and column density profile of TMC-1C, derived from fitting the 450, 850 and 1200 μm data and assuming a constant $\beta = 1.5$. The model starless core is made of cylindrical shells seen face on with a central temperature of ~ 6 K, rising to ~ 12 K at the edge. The central column density corresponds to ~ 80 magnitudes of visual extinction, falling to an A_V of ~ 20 at the edge. Using the equations in Section 5.3, we derive the resultant emission maps at 450, 850 and 1200 μm , add in Gaussian noise of the same magnitude as the random noise and reconstruction artifacts described above, and from these emission maps derive maps of the column density, temperature and emissivity spectral index. The resultant maps are shown in Figure 5.6.

When we solve for all three physical parameters, we find that the derived β of our model cloud has a median value of 1.5 (which is the input β everywhere in the model) with a standard deviation of 0.7. Given the close correspondence between the input value of β and the median value derived for it, we see that a constant value for the emissivity spectral index can be estimated in this manner. Using this constant value for β everywhere, we can then use our three flux maps to fit the temperature and column density. The resultant maps of our model constructed in this way are

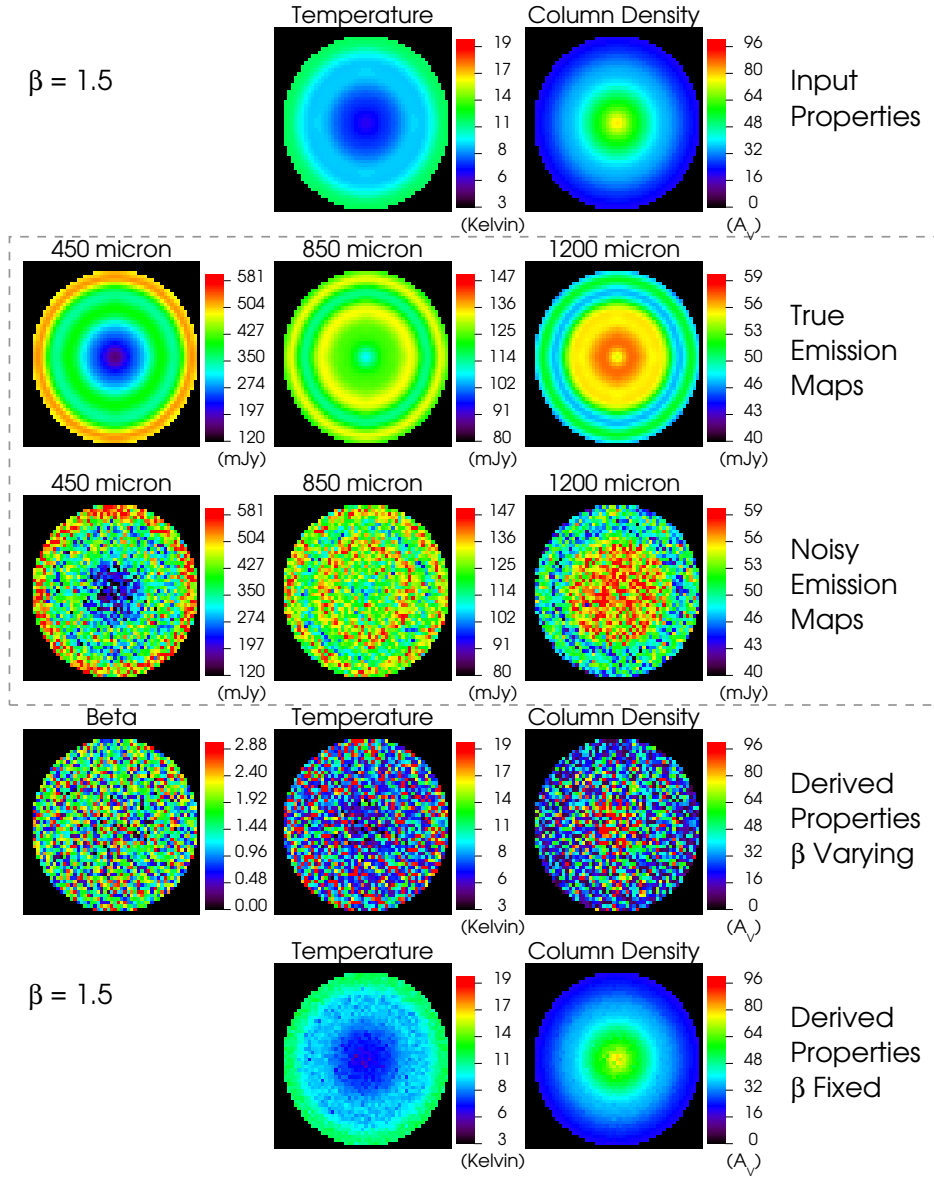


Figure 5.6.— The top row of panels shows the temperature and column density maps of a model starless core similar to the central 2' of TMC-1C. The second row from the top shows the predicted emission maps at 450, 850, and 1200 μm , using a constant $\beta = 1.5$. We then add Gaussian random noise to the emission maps equal to the measured noise in our 450, 850 and 1200 μm maps of TMC-1C (80, 9 and 3 mJy, respectively) and show the resultant fluxes in the third row. Using the altered fluxes, we attempt to solve for β , T_d and N_H at each point in the map, and show the results in the fourth row from the top. If we instead use the value for the emissivity spectral index ($\beta = 1.5$) everywhere and use the altered 450, 850 and 1200 μm fluxes to fit T_d and N_H , we get the maps shown in the bottom row.

shown in Figure 5.6.

5.5 Dust Emission in TMC-1C

5.5.1 Morphology

The observed 450 μm emission map of TMC-1C is qualitatively different from the 1200 μm map. The 450 μm map shows a condensation at (50, -150) (position “a” in Figure 5.7) which is much fainter at 850 μm and nearly absent at 1200 μm . The condensation at (-50, 150) (position “c” in Figure 5.7) is prominent at all wavelengths, while the column density peak at (0, 0) (position “b” in Figure 5.7) is prominent at 850 and 1200 μm , but not apparent at 450 μm .

An emission peak in the longer wavelength maps, but not prominent at 450 μm , can be explained by a cold temperature, as seen at the (0, 0) position. The 450 μm emission peak not seen at 1200 μm can be explained by the dust in that region having a steep spectral index ($\beta \geq 2$).

5.5.2 Derived Parameters

Based on our analysis in Section 5.4.1, calibration uncertainties, reconstruction artifacts and noise in our TMC-1C emission maps prevent us from making accurate maps of dust temperature, emissivity spectral index and column density *simultaneously*, even though this may well be the highest S/N set of such maps of a starless core to date. Figure 5.7 shows the results of an attempt to do so, and as expected the range of temperatures that we see is quite broad ($T_d < 5$ K and $T_d > 25$ K) for a starless core, with a similarly large spread in emissivity spectral index ($\beta < 0$ and $\beta > 2.5$) and column density. Furthermore, the errors and uncertainties in our emission maps create a spurious anti-correlation between the dust temperature and emissivity spectral index, which is also seen in our attempt to derive T_d , β and N_H from our simple model of a cylindrically symmetric starless core, described in Section 5.4.4. Because the noise and errors in our observed emission maps of TMC-1C will drive an anti-correlation between the derived dust temperature and emissivity spectral index even when such a trend does not exist, our results are consistent with a constant value of the emissivity spectral index. However, we cannot rule out a real anti-correlation such as that observed at 200, 260, 360 and 580 μm in the Orion molecular cloud (Dupac et al. 2001) and the M17 star-forming complex (Dupac et al.

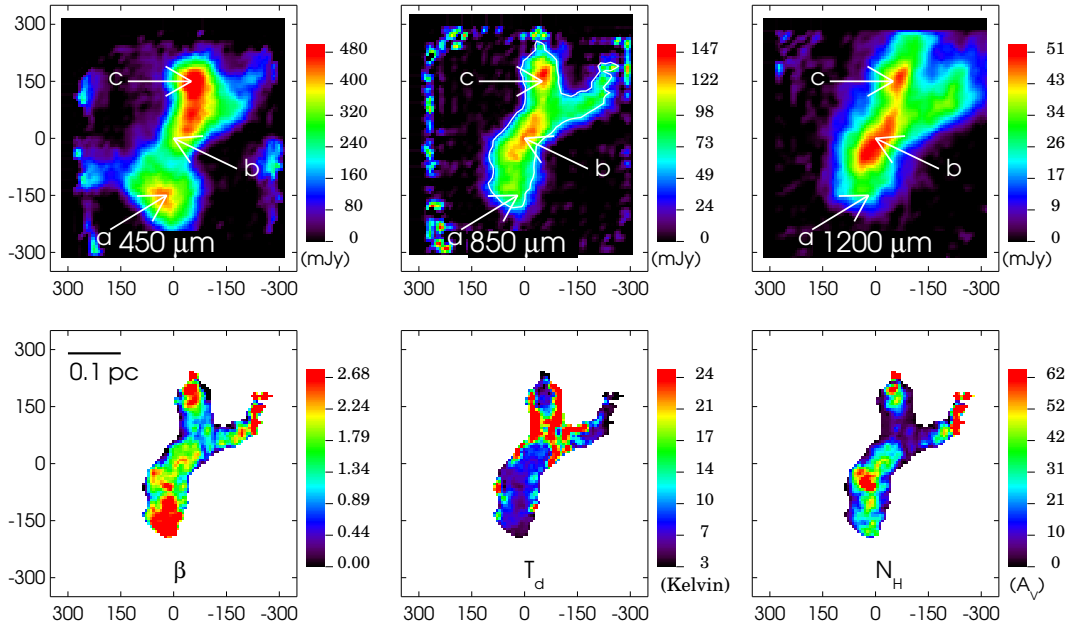


Figure 5.7.— The 450, 850 and 1200 μm emission maps of TMC-1C, along with the derived β , T_d and N_H (expressed in units of A_V for convenience). The fluxes are in units of mJy per $14''$ pixel. The derived parameters are shown within the white 850 μm contour. The (0,0) position is at RA=4:41:35.8 DEC=+26:00:42.5 (J2000). Position 'a' is strong at 450 μm but not at 850 or 1200 μm . Position 'b' is strong at 850 and 1200 μm but not at 450 μm and position 'c' is strong in all three maps.

2002).

Following the method described in Section 5.4.4, we use the three emission maps at 450, 850 and 1200 μm to derive a constant value of $\beta = 1.8 \pm 0.5$ for the portion of TMC-1C located within the white contour of the 850 μm image in Figure 5.7. We derive this value by running 1000 realizations of a Monte Carlo simulation of the observed flux maps in TMC-1C modified by the calibration uncertainties. Using $\beta = 1.8$, we construct dust temperature and column density maps (Figure 5.8) from a fit to the 450, 850 and 1200 μm images. The column density in Figure 5.8 peaks around the maximum of the 850 and 1200 μm emission. The implied visual extinction, calculated as in Section 5.4.3 is quite high, rising above 80 magnitudes in the densest regions. As expected, the regions with the highest column density are also the regions with the lowest dust temperature (Zucconi et al. 2001). By using a constant value of the emissivity spectral index ($\beta = 1.8$), the dust temperature that we derive is nowhere significantly higher than 16 K nor lower than 6 K.

Our derived value of $\beta = 1.8 \pm 0.5$ is somewhat higher than that measured for amorphous carbon grains ($\beta = 1.2$) by Mennella et al. (1998) and is within the range ($\sim 1.2 - 2.5$) measured for silicate grains by Agladze et al. (1996). Dust in interstellar disks are generally observed to have values of $\beta \leq 1$, but with considerable spread (Beckwith & Sargent 1991; Mannings & Emerson 1994). Observations by Stepnik et al. (2003) have shown that $\beta = 1.9 \pm 0.2$ for a dense filament in Taurus, which agrees very well with our estimate of TMC-1C. Graphite and silicate dust grains in the ISM are often assumed to have $\beta = 2$, e.g. (Draine & Lee 1984).

5.5.3 Comparison With Previous Results

The two-dimensional temperature and column density maps of TMC-1C, along with the deprojected three-dimensional temperature and density profiles, have previously been reported in Schnee & Goodman (2005) using only SCUBA 450 and 850 μm data. With the addition of the MAMBO 1200 μm map, we are better able to constrain the temperature and density and estimate the emissivity spectral index. The value of the emissivity spectral index that we estimate here ($\beta = 1.8$) is higher than assumed in Schnee & Goodman (2005) ($\beta = 1.5$) and the value that we use for κ_{230} is assumed to be larger in this paper than in Schnee & Goodman (2005), so the temperatures that we derive are somewhat lower and the densities are lower. We choose here to use the dust opacity appropriate for dust grains with thin ice mantles, evolved in a dense (10^6 cm^{-3}) region for 10^5 years derived in Ossenkopf & Henning (1994) because this is the consensus value settled upon by the *Spitzer* Legacy Project, “From Molecular Cloud Cores to Planet Forming Disks” (Evans

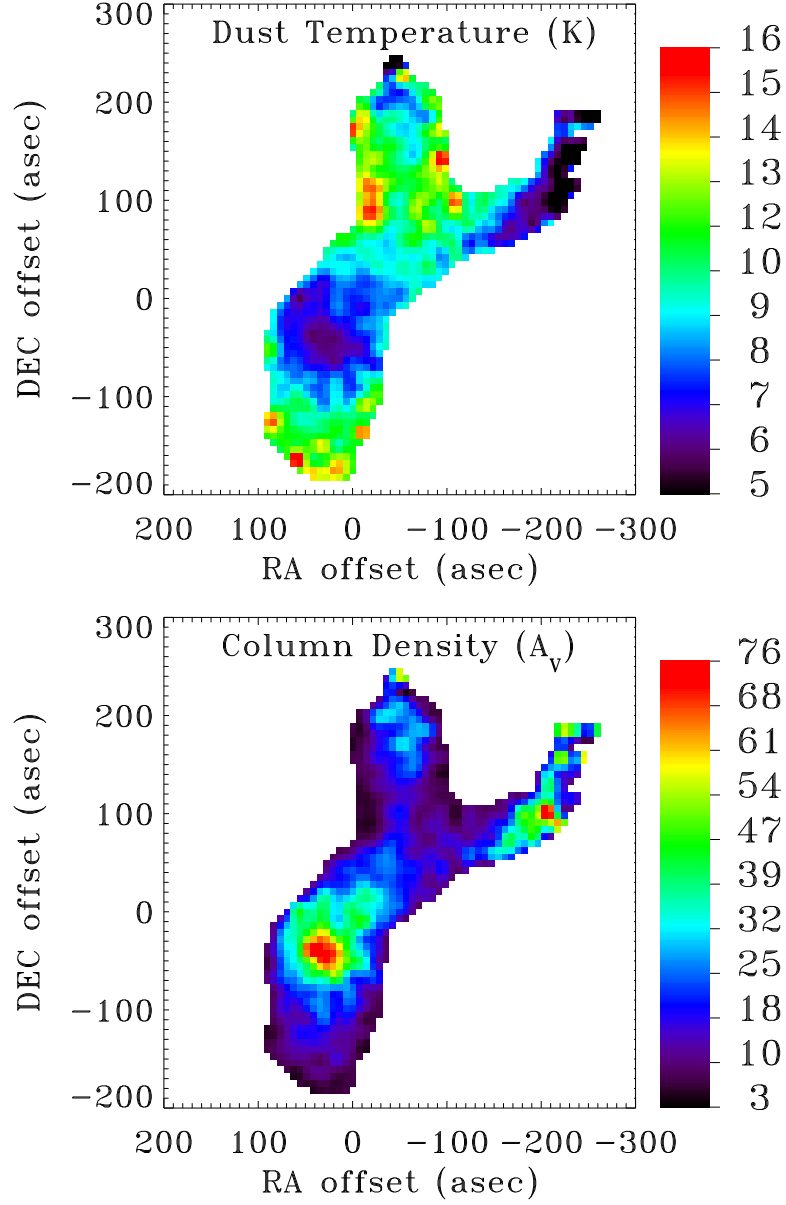


Figure 5.8.— The TMC-1C dust color temperature (top) and column density (bottom), derived from a fit to the 450, 850 and 1200 μm emission maps, assuming that the emissivity spectral index is constant at $\beta = 1.8$.

et al. 2003), which will make comparisons with other c2d cores easier in the future. The mass that we derive for TMC-1C, within a radius of 0.06 pc from the column density peak is $6 M_{\odot}$, as compared with $13 M_{\odot}$ in Schnee & Goodman (2005). However, even this new dust-derived mass is higher than the virial mass derived from TMC-1C N_2H^+ observations.

The deprojected three dimensional temperature and density profiles, constructed assuming spherical symmetry, are shown in Figure 5.9, along with the profiles calculated using only the 450 and 850 μm data and assuming that $\beta = 1.5$ and $\kappa_{230} = 0.005$, as in Schnee & Goodman (2005). The dust temperature profile that we derive is not much changed from that derived in Schnee & Goodman (2005), and is thus still consistent with the dust temperature profiles predicted for externally heated starless cores with Bonnor-Ebert density distributions calculated by Evans et al. (2001); Gonçalves et al. (2004); Stamatellos et al. (2004). A Bonnor-Ebert profile is a good fit to the TMC-1C density profile at radii greater than 0.004 pc, but as in Schnee & Goodman (2005), the density we derive for the innermost point is significantly higher than predicted by a Bonnor-Ebert model. The density profile, shown in Figure 5.9, is consistent with a broken powerlaw, with $n(r) \propto r^{-0.5}$ inside 0.035 pc and $n(r) \propto r^{-2.0}$ outside 0.035 pc. This is considerably flatter than the density profile derived using only the 450 and 850 μm data and $\beta = 1.5$, which have powerlaw exponents of -0.8 and -3.1 inside and outside the break radius, respectively (also shown in Figure 5.9). In Schnee & Goodman (2005) we report inner and outer powerlaw exponents of -0.8 and -1.8, also using just the 450 and 850 μm data and $\beta = 1.5$, but using a slightly different position as the center of the nested spherical shells.

5.6 Summary

We have used SCUBA data at 450 and 850 μm and MAMBO data at 1200 μm to create maps of the dust temperature and column density in TMC-1C, improving the results presented in Schnee & Goodman (2005). In addition, we are able to estimate the emissivity spectral index, finding a value of $\beta = 1.8 \pm 0.5$, based on calibration uncertainties. In addition, our analysis shows that noise and calibration errors in maps at 450, 850 and 1200 μm would have to be less than $\sim 2\%$ to accurately measure the dust temperature, emissivity spectral index and column density from three emission maps. Although such low levels noise and calibration uncertainties are not achievable with the current generation of bolometers, we show that the dust temperature, emissivity spectral index and column density can be accurately

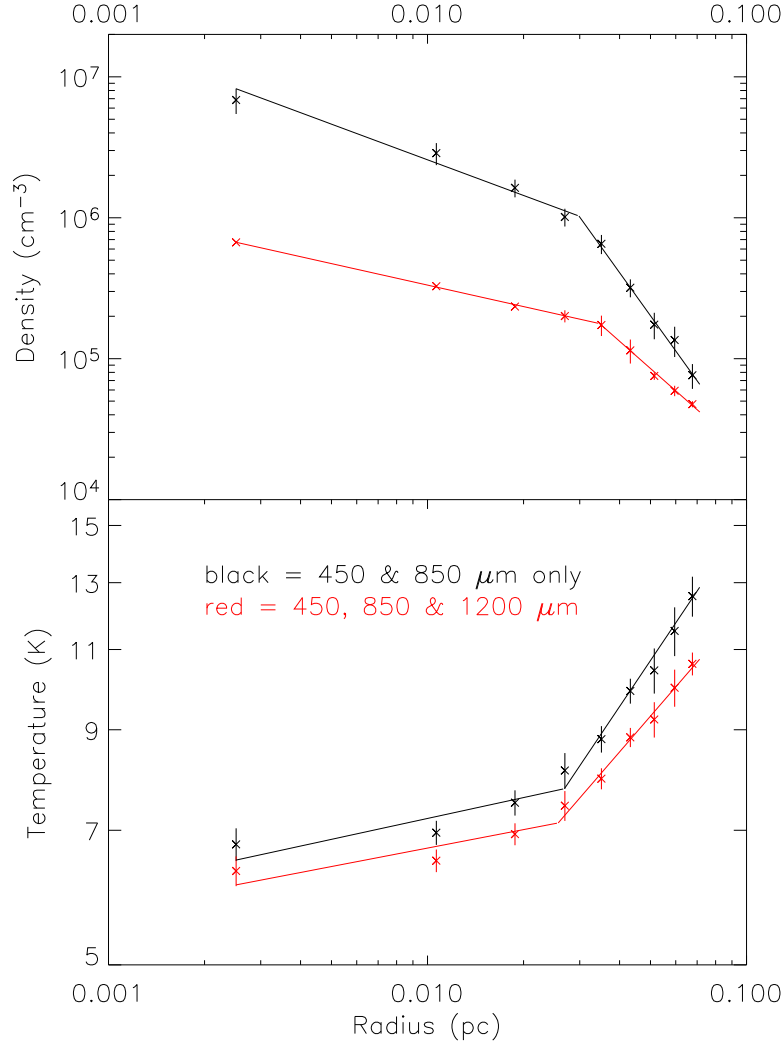


Figure 5.9.— The density (top) and temperature (bottom) profiles of TMC-1C. The points in red are determined by a fit to the 450, 850 and 1200 μm data, assuming $\beta = 1.8$ and $\kappa_{230} = 0.009$ and the black points are determined using only the 450 and 850 μm data assuming $\beta = 1.5$ and $\kappa_{230} = 0.005$, as in Schnee & Goodman (2005). In both cases, we assume that the central 2 arcminute radius of TMC-1C can be modeled as nested spherical shells of uniform density and temperature.

mapped if they are fitted at four wavelengths, for instance by including the $350\ \mu\text{m}$ SHARCII waveband. The next generation detector on the JCMT, SCUBA-2, will not need to sky-chop, allowing more large-scale structure to be visible, improved calibration and fewer image artifacts, making more accurate determinations of dust properties in cores possible.

Chapter 6

Chemistry and Velocity Gradients in TMC-1C

Scott Schnee, Paola Caselli, Alyssa Goodman, Hector Arce, Joseph Barranco, Javier Ballesteros-Paredes & Kishore Kuchibhotla

To be submitted to The Astrophysical Journal

Abstract

Using the IRAM 30m telescope, we have mapped the starless core TMC-1C in a variety of high and low density tracers. We calculate the column density implied by the gas measurements and compare those values with the column density implied by dust continuum measurements at 450, 850 and 1200 μm . Every molecular species that we observe, including $\text{N}_2\text{H}^+(1-0)$, shows evidence of depletion. The linewidths that we derive are constant across the core, neither rising nor falling with radius. The C^{18}O , C^{17}O and C^{34}S linewidths are significantly higher than the N_2H^+ linewidths, which are roughly twice the thermal linewidth. The velocity field in TMC-1C, while ordered, is inconsistent with previous claims of rotation.

6.1 Introduction

Dense starless cores in nearby low-mass star-forming regions such as Taurus represent the simplest areas in which to study the initial conditions of star formation. The dominant component of starless cores, H_2 , is largely invisible in the quiescent

interstellar medium, so astronomers typically rely on spectral line maps of trace molecules and continuum observations of the thermal emission from dust to derive their kinematics and physical state. Previous studies of starless cores in Taurus, as well as other nearby star-forming regions, have shown that the relative abundance of many molecules varies significantly between the warmer, less dense envelopes and the colder, denser interiors. For instance, Caselli et al. (1999); Tafalla et al. (2004) have shown that molecules such as C^{17}O , C^{18}O , C^{34}S , and CS are largely absent from the cores L1544, L1498 and L1517B at densities larger than a few 10^4 cm^{-3} , while N_2H^+ and ammonia are preferentially seen at high densities. The chemical variations within a starless core is likely the result of certain molecules freezing onto the surface of dust grains at high densities and low temperatures and the chemical interaction of molecules with each other.

In order to disentangle the information that can be gleaned from a combination of gas and dust observations of a dense core, we have mapped TMC-1C at three continuum wavelengths (Schnee et al. 2006c) and seven molecular lines. TMC-1C is a starless core in the Taurus molecular cloud, with a distance estimated at 140 pc (Kenyon et al. 1994). In a previous study, we have shown that TMC-1C has a mass of $6 M_\odot$ within a radius of 0.06 pc from the column density peak, which is a factor of two larger than the virial mass derived from the $\text{N}_2\text{H}^+(1-0)$ line width, and we have shown that there is evidence for sub-sonic infall (Schnee & Goodman 2005) as well as solid body rotation at a rate of $0.3 \text{ km s}^{-1} \text{ pc}^{-1}$ (Goodman et al. 1993). TMC-1C is a coherent core with a roughly constant velocity dispersion, slightly higher than the sound speed, over a radius of 0.1 pc (Barranco & Goodman 1998; Goodman et al. 1998). Using SCUBA and MAMBO bolometer maps of TMC-1C at 450, 850 and $1200 \mu\text{m}$, we have mapped the dust temperature and column density (Schnee et al. 2006c).

In this paper we investigate the depletion of various molecules in TMC-1C as a function of both dust column density and dust temperature. We also analyze the line widths of each molecular species and map the local line-of-sight velocity gradients from each set of spectral lines.

6.2 Observations

6.2.1 Continuum

We observed a $10' \times 10'$ region around TMC-1C using SCUBA (Holland et al. 1999) on the JCMT at 450 and $850 \mu\text{m}$. We used the standard scan-mapping mode,

recording 450 and 850 μm data simultaneously (Pierce-Price et al. 2000; Bianchi et al. 2000). Chop throws of 30'', 44'' and 68'' were used in both the right ascension and declination directions. The resolution at 450 and 850 μm is 7.5'' and 14'' respectively. The absolute flux calibration at 450 and 850 μm is $\sim 12\%$ and $\sim 4\%$. The noise in the 450 and 850 μm maps are 13 and 9 mJy/beam. The data reduction is described in detail in Schnee et al. (2006c).

We used the MAMBO-2 array (Kreysa et al. 1999) on the IRAM 30-meter telescope on Pico Veleta (Spain) to map TMC-1C at 1200 μm . The MAMBO beam size is $10''.7$. The source was mapped on-the-fly, chopping in azimuth by 60'' to 70'' at a rate of 2 Hz. The absolute flux calibration is uncertain to $\sim 10\%$, and the noise in the 1200 μm map is 3 mJy/beam. The data reduction is described in detail in Kauffmann et al. (in prep.).

6.2.2 Spectral Line

We observed TMC-1C using the IRAM 30-meter telescope in November 1998, making spectral line maps of the $\text{C}^{17}\text{O}(1-0)$, $\text{C}^{17}\text{O}(2-1)$, $\text{C}^{18}\text{O}(2-1)$, $\text{C}^{34}\text{S}(2-1)$, $\text{DCO}^+(2-1)$, $\text{DCO}^+(3-2)$, $\text{N}_2\text{H}^+(1-0)$ transitions. The inner 2' of TMC-1C were observed with 20'' spacing in frequency-switching mode, and outside of this radius the data were collected with 40'' sampling. The data were reduced using the CLASS package, with second-order polynomial baselines subtracted from the spectra. The system temperatures, velocity resolution, beam size and beam efficiencies are listed in Table 6.1. The spectra taken at the peak of the dust column density map are shown in Figure 6.1. The integrated intensity, velocity, line width and RMS noise for each transition is given in Table 6.2.

6.3 Results and Analysis

6.3.1 Column Densities

To derive the column density of gas from each molecule, we assume that the emission is optically thin and that all rotation levels are characterized by the same excitation temperature T_{ex} . In this case the total column density of a linear molecule is given by:

Table 6.1. Observing Parameters of IRAM Spectra

Transition	T_{sys} Kelvin	Spectral Resolution km s^{-1}	FWHM arcseconds	B_{eff}	Frequency ^a GHz	VLSR km s^{-1}
C ¹⁷ O(1-0)	353	0.052	18.4	0.6620	112.3592837	5.2
C ¹⁷ O(2-1)	1893	0.052	9.2	0.4006	224.7143850	5.2
C ¹⁸ O(2-1)	1050	0.053	9.4	0.4107	219.5603541	5.2
C ³⁴ S(2-1)	202	0.061	21.4	0.7206	96.4129495	5.2
DCO ⁺ (2-1)	479	0.041	14.3	0.5425	144.0773190	5.2
DCO ⁺ (3-2)	622	0.054	9.5	0.4158	216.1126045	5.2
N ₂ H ⁺ (1-0)	185	0.031	22.1	0.7319	93.1737000	5.2

^aAll frequencies taken from the Leiden Atomic and Molecular Database (Schöier et al. 2005)

Table 6.2. Fit Line Parameters at Dust Peak

Transition	VLSR km s^{-1}	$\int \text{Tdv}$ K km s^{-1}	FWHM km s^{-1}	rms K	f_D ^a
C ¹⁷ O(1-0)	5.33 ± 0.03	0.370 ± 0.07	0.446 ± 0.11	0.089	4.6
C ¹⁷ O(2-1)	5.49 ± 0.01	0.707 ± 0.05	0.426 ± 0.04	0.144	1.5
C ¹⁸ O(2-1)	5.15 ± 0.01	2.700 ± 0.05	0.471 ± 0.01	0.250	1.6
C ³⁴ S(2-1)	5.26 ± 0.04	0.174 ± 0.03	0.497 ± 0.10	0.092	40
DCO ⁺ (2-1)	5.14 ± 0.01	0.280 ± 0.03	0.164 ± 0.02	0.204	17
DCO ⁺ (3-2)	5.25 ± 0.02	0.340 ± 0.04	0.263 ± 0.04	0.179	17
N ₂ H ⁺ (1-0)	5.21 ± 0.01	0.202 ± 0.03	0.193 ± 0.03	0.104	1.9

^aDepletion from dust-derived $N_{H_2} = 1.2 \times 10^{23}$, N_{tot} and X_{can}

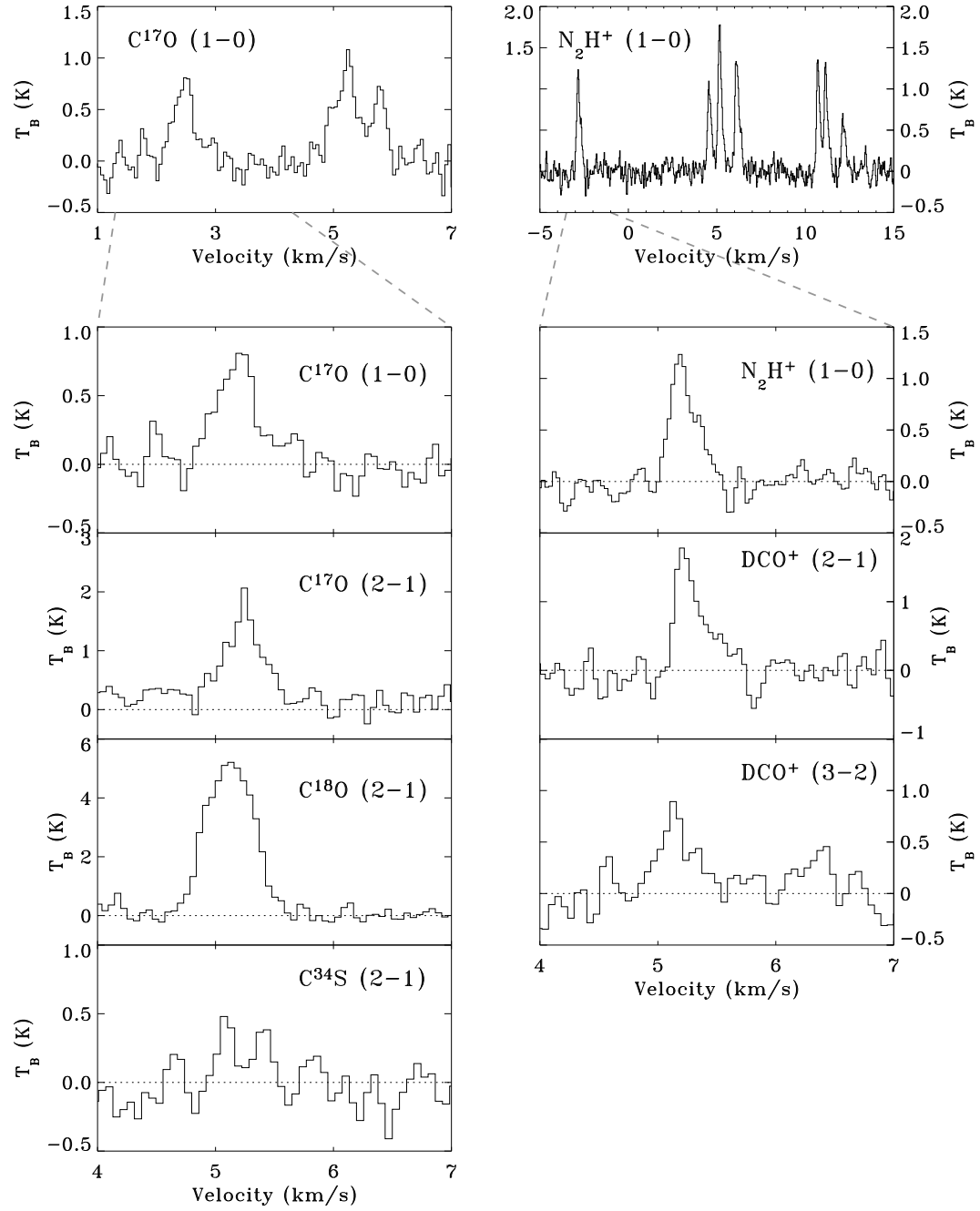


Figure 6.1.— The spectra taken at the (0,20) position, which is the peak of the dust emission map.

$$N_{tot} = \frac{8\pi W}{\lambda^3 A} \frac{g_l}{g_u} \frac{1}{J_\nu(T_{ex}) - J_\nu(T_{bg})} \frac{1}{1 - \exp(-h\nu/kT_{ex})} \frac{Q_{rot}}{g_l \exp(-E_l/kT_{ex})} \quad (6.1)$$

where λ and ν are the wavelength and frequency of the transition, k is the Boltzmann constant, h is the Planck constant, A is the Einstein coefficient, g_l and g_u are the statistical weights of the lower and upper levels, $J_\nu(T_{ex})$ and $J_\nu(T_{bg})$ are the equivalent Rayleigh-Jeans excitation and background temperatures, W is the integrated intensity of the line and Q_{rot} (the partition function) and E_l (the energy of the lower level) are given by:

$$Q_{rot} = \sum_{J=0}^{\infty} (2J+1) \exp(-E_J/kT) \quad (6.2)$$

and

$$E_J = J(J+1)hB \quad (6.3)$$

and B is the rotational constant (see Table 2.4 for the values of the constants).

Equation 6.1 is true only in the case of optically thin emission, but we can see in Figure 6.1 that the $N_2H^+(1-0)$ emission at the dust peak shows signs of self-absorption. To correct for this, for those spectra with sufficient signal to noise ($S/N > 3$ for the most optically thin hyperfine component), the integrated $N_2H^+(1-0)$ intensity that we assign to each pixel is the integrated intensity of the most optically thin hyperfine component divided by the statistical weight of that component ($1/27$). As long as the total optical depth in the $N_2H^+(1-0)$ transition is less than 27, this procedure will prevent us from underestimating the N_2H^+ column density. Based on hyperfine fits to the $C^{17}O(1-0)$ transition and a comparison of the relative strengths of the three components, we see that the $C^{17}O(1-0)$ emission is optically thin throughout TMC-1C. Although the noise is generally too high in the $C^{17}O(2-1)$ data to make indisputable hyperfine fits, the results of such an attempt suggest that the $C^{17}O(2-1)$ lines are also optically thin, which is expected for thin $C^{17}O(1-0)$ emission and temperatures of ~ 10 K. In order to estimate the optical depth of the $C^{18}O(2-1)$ lines, we compare the integrated intensity of $C^{18}O(2-1)$ to that of $C^{17}O(2-1)$. If both lines are thin, then the observed ratio should be equal to the cosmic abundance ratio, $[^{18}O]/[^{17}O] = 3.65$ (Wilson & Rood 1994; Penzias 1981). We observe that the ratio of the integrated intensities $R_{18,17} = 2.3 \pm 0.9$, which corresponds to an optical depth of the $C^{18}O(2-1)$ line of $\tau_{18} \simeq 1.5$ (Caselli et al. 2002c; Kramer et al. 1999). The observed ratio, $R_{18,17}$ is independent of the column density derived from dust emission.

To derive the column density and the temperature of the dust in TMC-1C,

we use our SCUBA and MAMBO maps at 450, 850 and 1200 μm . The continuum emission is given by:

$$S_\nu = \Omega B_\nu(T_d) \kappa_\nu \mu m_H N_{H_2}, \quad (6.4)$$

where

$$B_\nu(T_d) = \frac{2h\nu^3}{c^2} \frac{1}{\exp(h\nu/kT_d) - 1} \quad (6.5)$$

and

$$\kappa_\nu = \kappa_{230} \left(\frac{\nu}{230 \text{ GHz}} \right)^\beta. \quad (6.6)$$

In Equation 6.4, S_ν is the flux density; Ω is the solid angle of the beam; $B_\nu(T_d)$ is the blackbody emission from the dust at temperature T_d ; $\kappa_{230} = 0.009 \text{ cm}^2 \text{ g}^{-1}$ is the emissivity of the dust grains at 230 GHz (Ossenkopf & Henning 1994); m_H is the mass of the hydrogen atom; $\mu = 2.8$ is the mean molecular weight of interstellar material in a molecular cloud per hydrogen molecule, N_{H_2} is the column density of hydrogen molecules and we assume a dust to gas ratio of 100. We assume that $\beta = 1.8$, as explained in Schnee et al. (2006c).

We smooth the flux maps to 20'', which is the spacing between IRAM observations in the center of TMC-1C. At each position, we make a non-linear least squares fit for the dust temperature and column density such that the difference between the predicted and observed 450, 850 and 1200 μm observations is minimized. The errors associated with such a fitting procedure are demonstrated in Schnee et al. (2006c). The dust column density and temperature maps are shown in Figure 6.2.

6.3.2 Molecular Depletion

By comparing the integrated intensity maps of $\text{C}^{18}\text{O}(2-1)$ and $\text{N}_2\text{H}^+(1-0)$ in TMC-1C with the H_2 column density, shown in Figure 6.3, we see that at the location of the dust column density peak the $\text{C}^{18}\text{O}(2-1)$ emission is not peaked at all. The $\text{N}_2\text{H}^+(1-0)$ emission peaks in a ridge around the dust column density maximum, not at the peak, but in general N_2H^+ traces the dust better than the C^{18}O emission does. By inspection, we see that there is evidence for depletion and/or self-absorption in the high and low density tracers in TMC-1C, which we quantify and compare to similar cores below.

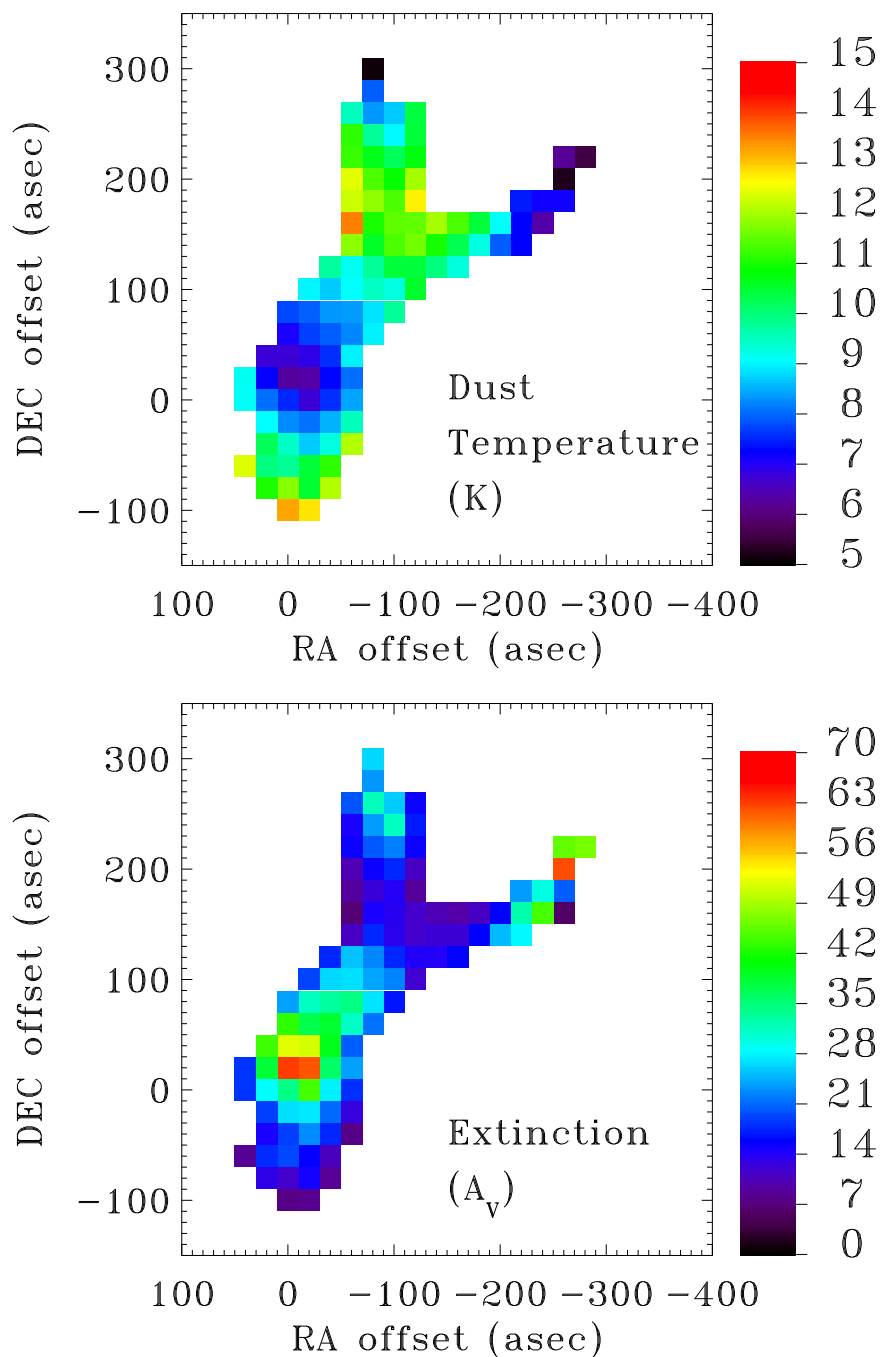


Figure 6.2.— The dust-derived temperature (top) and implied visual extinction (bottom) of TMC-1C, centered on the same (0,0) position as the gas measurements, from Schnee et al. (2006c).

Table 6.3. Molecular Transition Constants

Transition	A ^a s^{-1}	B ^{b,c} GHz	g_l	g_u	X_{can} n/n_{H_2}
C ¹⁷ O(1-0)	6.697E-8	56.179990	1	3	4.7×10^{-8d}
C ¹⁷ O(2-1)	6.425E-7	***	3	5	***
C ¹⁸ O(2-1)	6.011E-7	54.891420	3	5	1.7×10^{-7e}
C ³⁴ S(2-1)	1.600E-5	24.103548	3	5	1.3×10^{-10f}
DCO ⁺ (2-1)	2.136E-4	36.01976	3	5	2.8×10^{-10g}
DCO ⁺ (3-2)	7.722E-4	***	5	7	***
N ₂ H ⁺ (1-0)	3.628E-5	46.586867	1	3	1.6×10^{-10h}

^aEinstein A coefficients are taken from the Leiden Atomic and Molecular Database (Schöier et al. 2005)

^b(Caselli et al. 2002c)

^c(Gottlieb et al. 2003)

^d(Crapsi et al. 2004)

^e(Goldsmith et al. 1997)

^f(Tafalla et al. 2002)

^g(Lee et al. 2003)

^h(Tafalla et al. 2004)

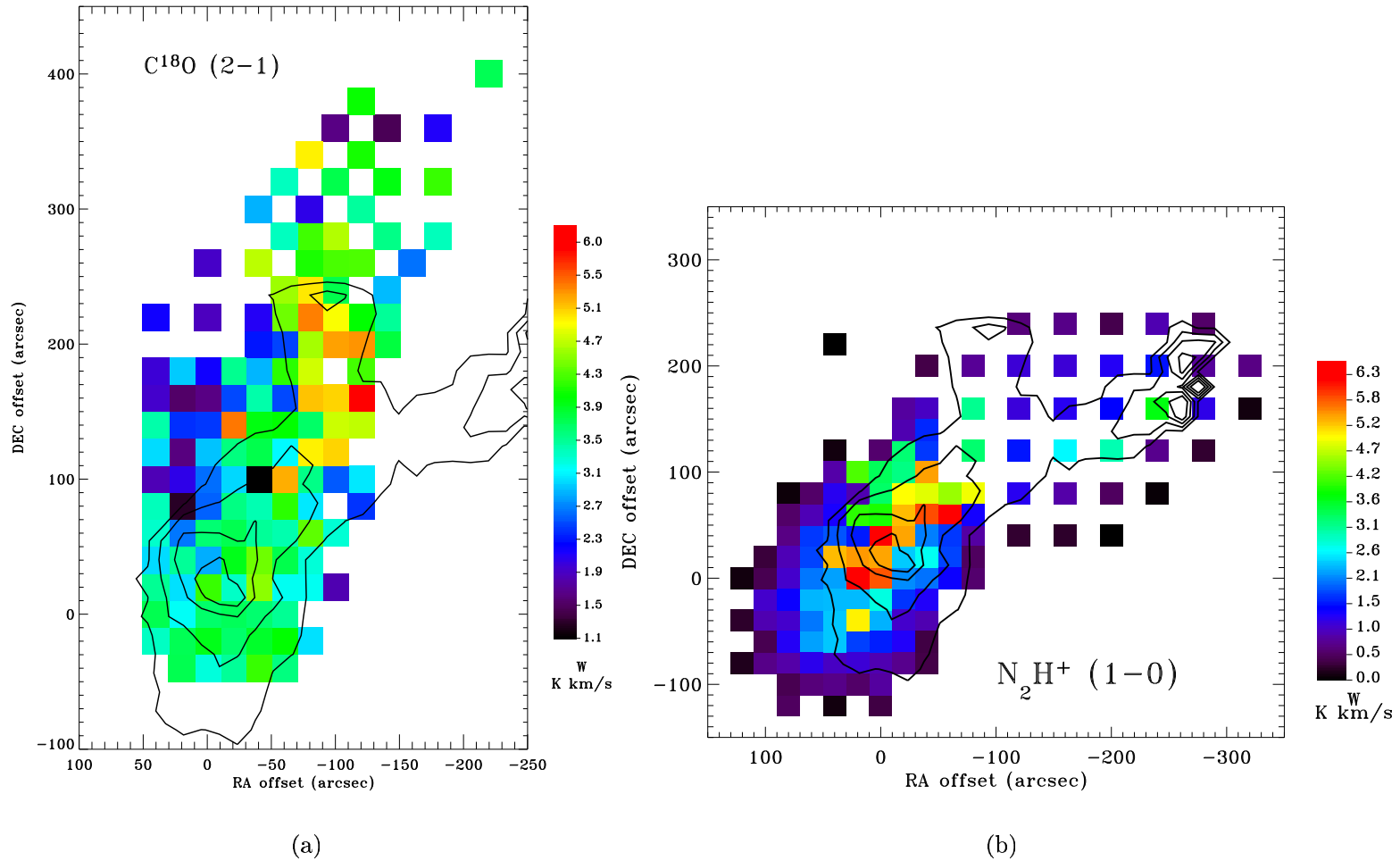


Figure 6.3.— The integrated intensity maps of $\text{C}^{18}\text{O}(2-1)$ and $\text{N}_2\text{H}^+(1-0)$ are plotted. The N_2H^+ integrated intensity in pixels with high signal to noise ($S/N > 3$) has been calculated from the thinnest hyperfine component to avoid the effects of self-absorption. The $\text{C}^{18}\text{O}(2-1)$ emission is corrected for self absorption assuming that $\tau = 1.5$. The contours show the visual extinction derived from the dust emission, at levels of $A_V = 10, 25, 40, 55$.

Previous molecular line observations of starless cores such as L1512, L1544, L1498 and L1517B, consistently show that CO and its isotopologues are significantly depleted, e.g. (Lee et al. 2003; Tafalla et al. 2004). However, other molecules such as DCO⁺ and N₂H⁺ are sometimes seen to trace the dust emission quite well, e.g. (Benson et al. 1998; Tafalla et al. 2004), while other studies have shown these molecules freezing out onto dust grains in the central regions of the cores, e.g. (Bergin et al. 2002; Caselli et al. 2002b). In order to measure the depletion in TMC-1C, we define the depletion factor of species i :

$$f_D(i) = X_{can}(i) \frac{N(H_2)_{dust}}{N(i)} \quad (6.7)$$

where X_{can} is the ratio of the molecular species to H₂ (see Table 6.3), $N(H_2)_{dust}$ is the column density of molecular hydrogen as derived from dust emission, and $N(i)$ is the column density of the molecular species as derived in Section 6.3.1, (Crapsi et al. 2004). The column density of N₂H⁺ is corrected for self-absorption by using the integrated intensity of the thinnest component and dividing by that component's statistical weight. The C¹⁸O column density is corrected for self-absorption by $\tau_{18}/(1 - \exp(-\tau_{18}))$, as in Lee et al. (2003).

The derived depletion factors for each molecule in each position with high signal to noise ($S/N > 3$) are plotted against the dust-derived column density in Figure 6.4. For each transition in each molecule the depletion factor increases with higher column density and lower dust temperature. The depletion in TMC-1C of the high-density tracers DCO⁺ and N₂H⁺ has been seen in other dense cores, such as L1544 and B68 (Bergin et al. 2002; Caselli et al. 2002b) and the class 0 protostar IRAM 04191+1522 (Belloche & André 2004), but for the first time a clear depletion gradient for N₂H⁺ is found. Crapsi et al. (2004) find a linear relationship between C¹⁸O depletion and dust derived column density in the starless core L1521F, which is seen in TMC-1C in both C¹⁷O and C¹⁸O.

Because of the anti-correlation between dust temperature and column density, we expect that there will also be an anti-correlation between the depletion factor, f_D , and dust temperature. Figure 6.5 shows the depletion factor for each molecule plotted against the line-of-sight averaged dust temperature. As expected, the depletion is highest in the low temperature regions though the lower signal to noise in C³⁴S and DCO⁺ make this somewhat harder to see. The anti-correlation between the depletion factor and dust temperature has also been seen by Kramer et al. (1999) in IC5146 with the tracer C¹⁸O, though in TMC-1C the temperatures are somewhat lower.

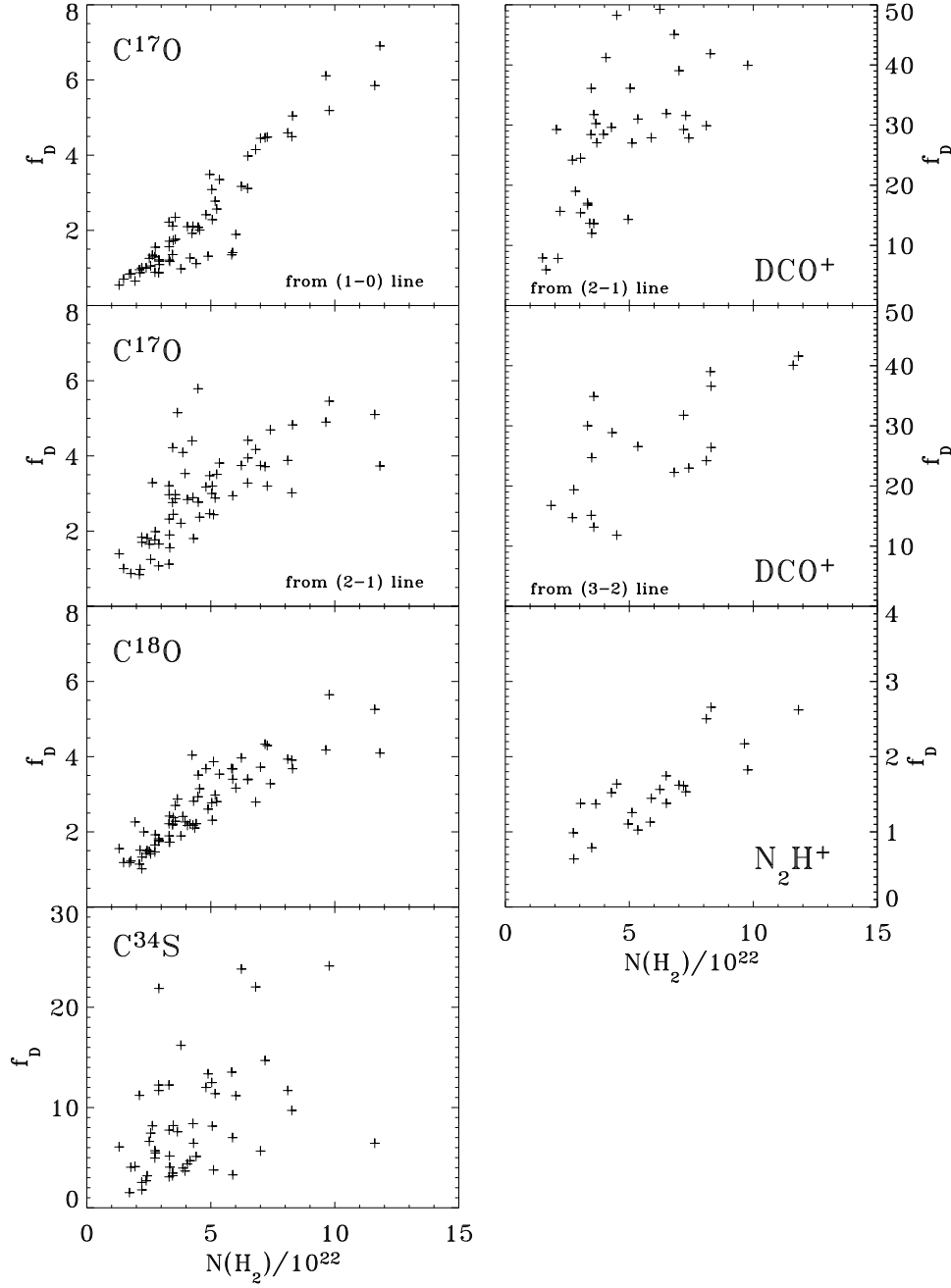


Figure 6.4.— The depletion factor for each molecular transition observed with the IRAM 30m plotted against the column density derived from dust emission maps at 450, 850 and 1200 μm . The N_2H^+ column density in pixels with high signal to noise ($\text{S/N} > 3$) has been calculated from the thinnest hyperfine component to avoid the effects of self-absorption. The C^{18}O column density has been calculated assuming that $\tau_{18} = 1.5$.

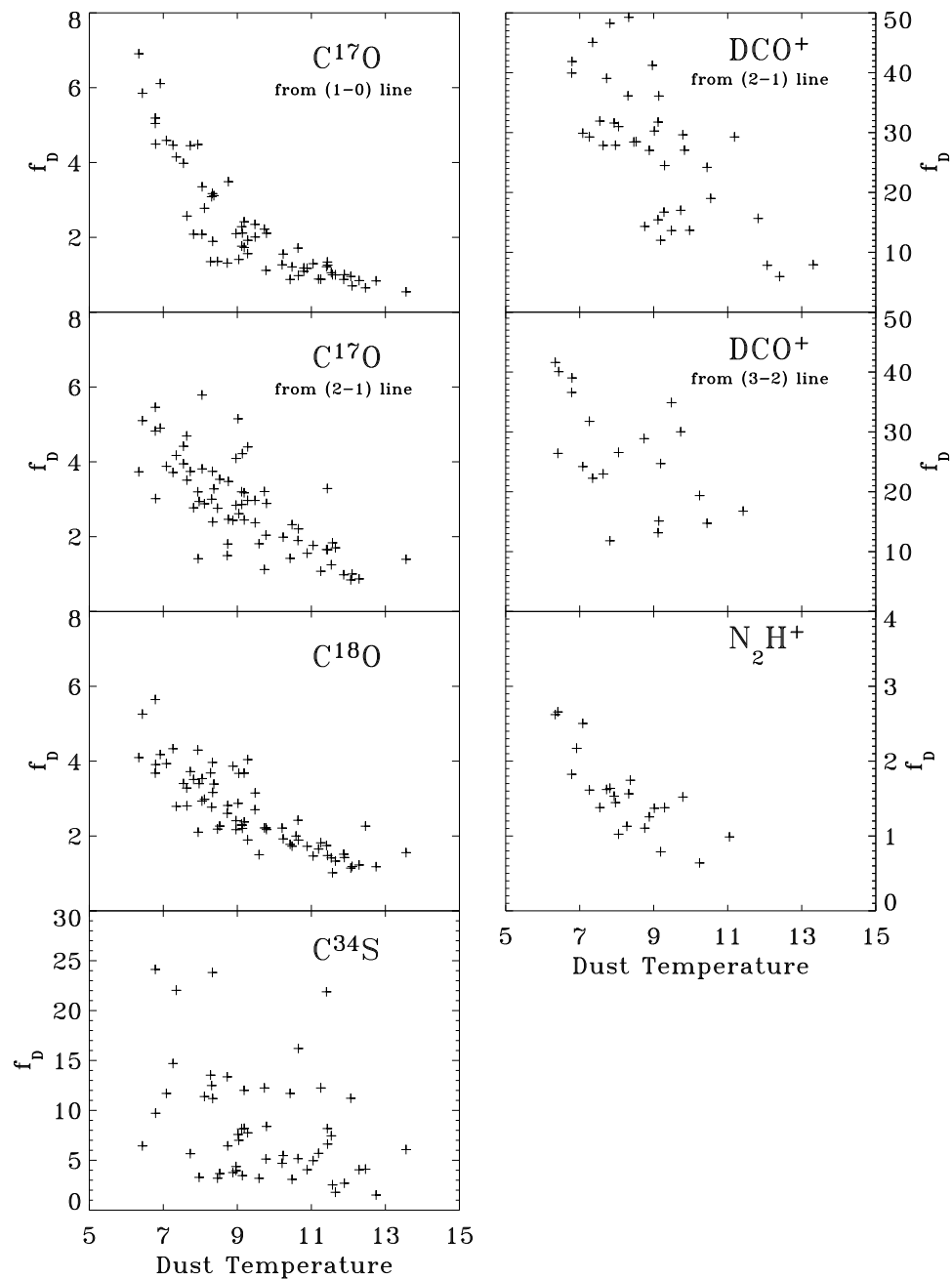


Figure 6.5.— Same as Figure 6.4, except that the depletion factor is plotted against the derived dust temperature.

6.3.3 Line Widths

Ammonia observations of TMC-1C have shown that it is a coherent core, having a constant line width across the core at a value slightly higher than the thermal line width (Barranco & Goodman 1998). Outside of the coherence radius (~ 0.1 pc), the line widths are expected to increase due to undissipated turbulent broadening (Goodman et al. 1998). Although this picture seems to be the case for the majority of starless cores surveyed in N_2H^+ and N_2D^+ by Crapsi et al. (2005), the cores most similar to TMC-1C (L1544 and L1521F) and L694-2, show that the line width increases towards the center.

Our N_2H^+ observations of TMC-1C show that the line width remains constant, at a value ~ 2 times higher than the thermal line width, over the entire core (see Figure 6.6), though the dispersion in the N_2H^+ line width is very large. This result is in agreement with the NH_3 observations of TMC-1C, and is not consistent with the decreasing N_2H^+ and N_2D^+ linewidths at larger radii seen in L1544 and L1521F, which in other important ways closely resemble TMC-1C. The line widths that we measure in C^{17}O and C^{18}O are larger than the N_2H^+ linewidths throughout TMC-1C, which contrasts with the results seen in C^{18}O and N_2H^+ in B68 (Lada et al. 2003).

In order to compare the thermal and non-thermal line widths in TMC-1C, we assume that the gas temperature is equal to the dust-derived temperature and use the formulae:

$$\Delta v_{thermal} = \sqrt{\left(\frac{8 \ln(2) k T_d}{\mu m_H} \right)} \quad (6.8)$$

$$\Delta v_{non-thermal} = \sqrt{(\Delta v_{observed})^2 - (\Delta v_{thermal})^2} \quad (6.9)$$

where μ is the molecular weight of the species and m_H is the mass of hydrogen. The assumption that the gas and dust temperatures are coupled is justified where the density is higher than $\sim 3 \times 10^4$, which is true for the entire region of TMC-1C for which we have data (Galli et al. 2002; Schnee et al. 2006c).

Figure 6.7 shows the ratio of the thermal line width to the non-thermal line width at the position of the dust column density peak. Although C^{17}O , C^{18}O , DCO^+ and N_2H^+ all have similar molecular weights, they have significantly different values for the line width ratios. The thermal line width is much smaller than the non-thermal line width for the molecules C^{17}O and C^{18}O , while the ratio is closer to unity for DCO^+ and N_2H^+ . This suggests that the isotopologues of CO are tracing material at larger distances from the center, with a larger turbulent

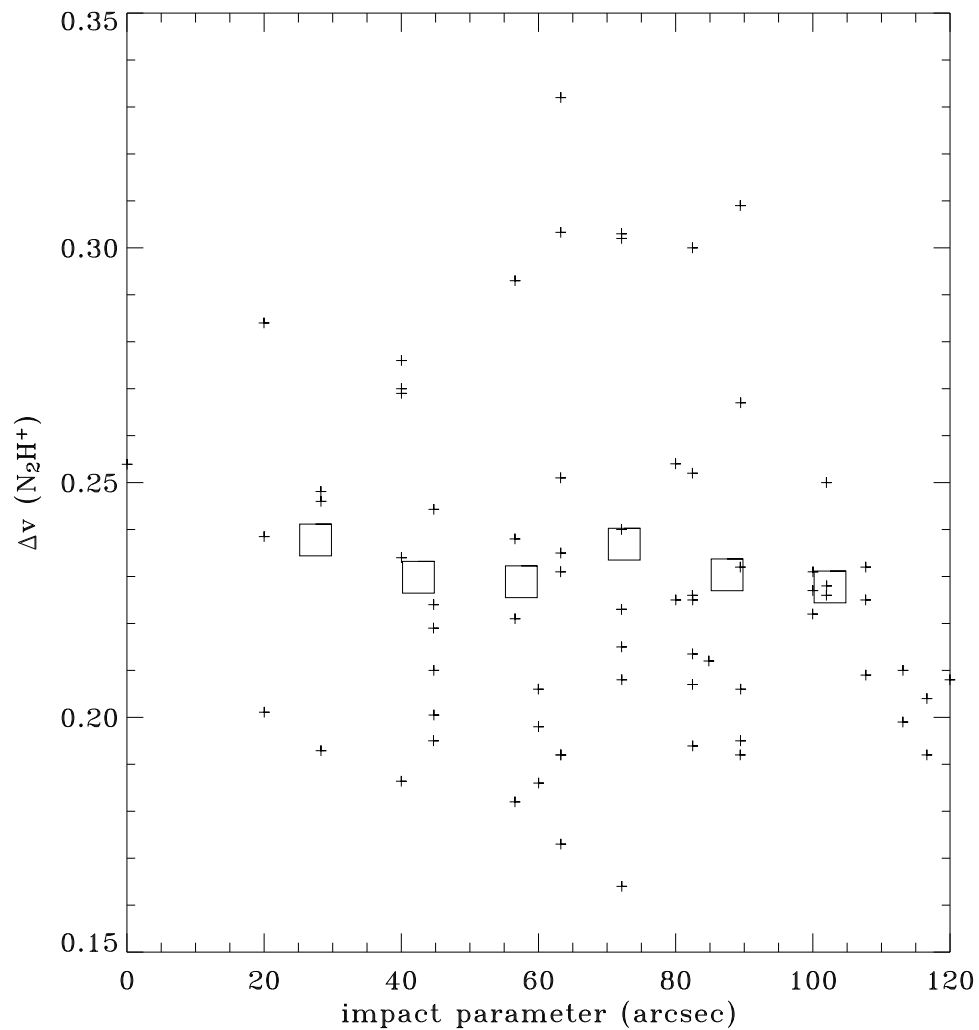


Figure 6.6.— $\text{N}_2\text{H}^+(1-0)$ line width (in km s^{-1}) vs. distance from the peak of the dust column density map. The crosses show the values at each position in the map with $S/N > 3$, and the large squares are averages of the data with $15''$ bins.

line width, than are DCO^+ and N_2H^+ , which presumably are tracing the higher density material closer to the center of TMC-1C. Although the $\text{C}^{18}\text{O}(2-1)$ transition is slightly thick, the line width measured is nearly identical to that derived for the thin $\text{C}^{17}\text{O}(2-1)$ transition shown in Figure 6.7. For each transition observed, we see no clear correlation between the observed line width and the thermal line width (and therefore with temperature, column density and distance from the peak column density). As in the study of depletion, the lower signal to noise in $\text{C}^{34}\text{S}(2-1)$, $\text{DCO}^+(2-1)$ and $\text{DCO}^+(3-2)$ make any possible trends between Δv and $\Delta v_{\text{thermal}}$ more difficult to determine.

6.3.4 Velocity Gradients

In order to study the velocity field of TMC-1C, we fit the $\text{C}^{17}\text{O}(2-1)$, $\text{C}^{18}\text{O}(2-1)$, $\text{C}^{34}\text{S}(2-1)$, $\text{DCO}^+(2-1)$ and $\text{DCO}^+(3-2)$ spectra with a Gaussian and assign the centroid velocity to each pixel. The velocity of the $\text{C}^{17}\text{O}(1-0)$ and $\text{N}_2\text{H}^+(1-0)$ velocities are determined by hyperfine spectral fits because the transitions have multiple components. For those N_2H^+ spectra that show evidence of self-absorption, the velocity is derived from a Gaussian fit to the thinnest component. The velocity gradient at each position is calculated by fitting the velocity of that point and its nearby neighbors to the function:

$$v_{l_{sr}} = v_o + \frac{dv}{ds}\Delta\alpha \cos \theta + \frac{dv}{ds}\Delta\delta \sin \theta \quad (6.10)$$

where v_o is the bulk motion along the line of sight, $\Delta\alpha$ and $\Delta\delta$ are RA and DEC offsets from the position of the central pixel, dv/ds is the magnitude of the velocity gradient in the plane of the sky, and θ is direction of the velocity gradient. The fit to the velocity gradient at each position is done as in Goodman et al. (1993).

Ammonia observations of TMC-1C have suggested that there is a velocity gradient of $0.3 \text{ km s}^{-1} \text{ pc}^{-1}$ (Goodman et al. 1993). The velocity field that we measure in TMC-1C has spatial resolution three times greater than the ammonia study, and reveals a pattern more complicated than that of solid body or differential rotation. The velocity fields measured by $\text{C}^{17}\text{O}(1-0)$, $\text{C}^{17}\text{O}(2-1)$ and $\text{C}^{18}\text{O}(2-1)$ are shown in Figure 6.8. Although there is a region that closely resembles the velocity field expected from rotation (gradient arrows of approximately equal length pointing in the same direction), the measured velocities vary from blue to red to blue along a NW - SE axis. The $\text{DCO}^+(2-1)$ and $\text{N}_2\text{H}^+(1-0)$ velocity fields (shown in Figure 6.9) also follow the same blue to red to blue pattern along the NW - SE axis, but the observations cover a somewhat different area than the CO observations, which

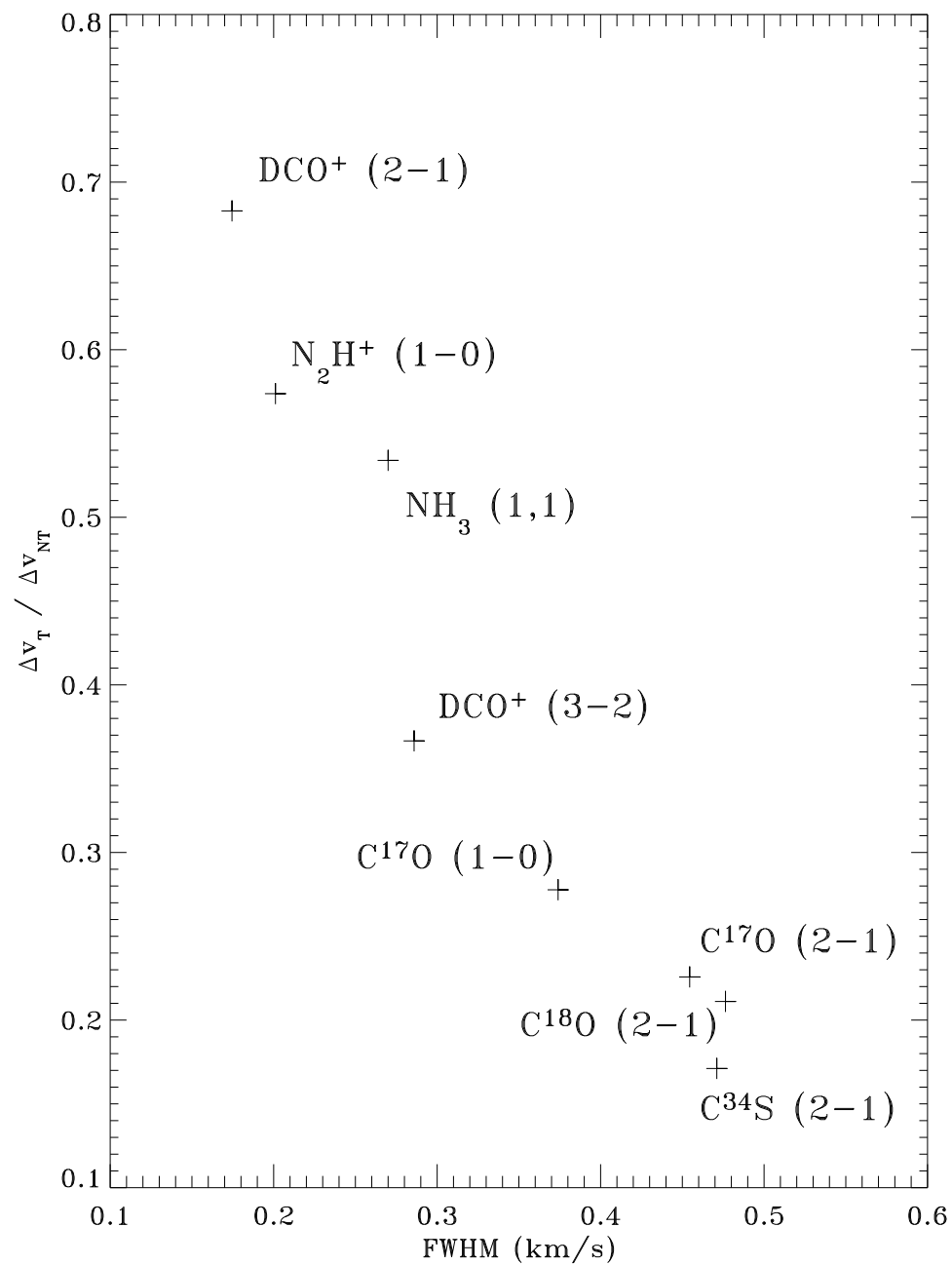


Figure 6.7.— The ratio of the thermal line width to the non-thermal line width from IRAM 30m spectra at the dust emission peak. The thermal line width is calculated from the dust temperature derived from dust emission maps at 450, 850 and 1200 μ m. The NH₃ intrinsic line width is taken from Barranco & Goodman (1998).

complicates making a direct comparison. Taken as a whole, it is clear that there is an ordered velocity field in TMC-1C, and that the low density CO tracers see a similar velocity field to the high density DCO^+ and N_2H^+ measurements. However, we are unable to confirm the rotation reported in Goodman et al. (1993). The direction and magnitude of the velocity gradient in the region that resembles solid body rotation is shown in Figure 6.10 for each tracer.

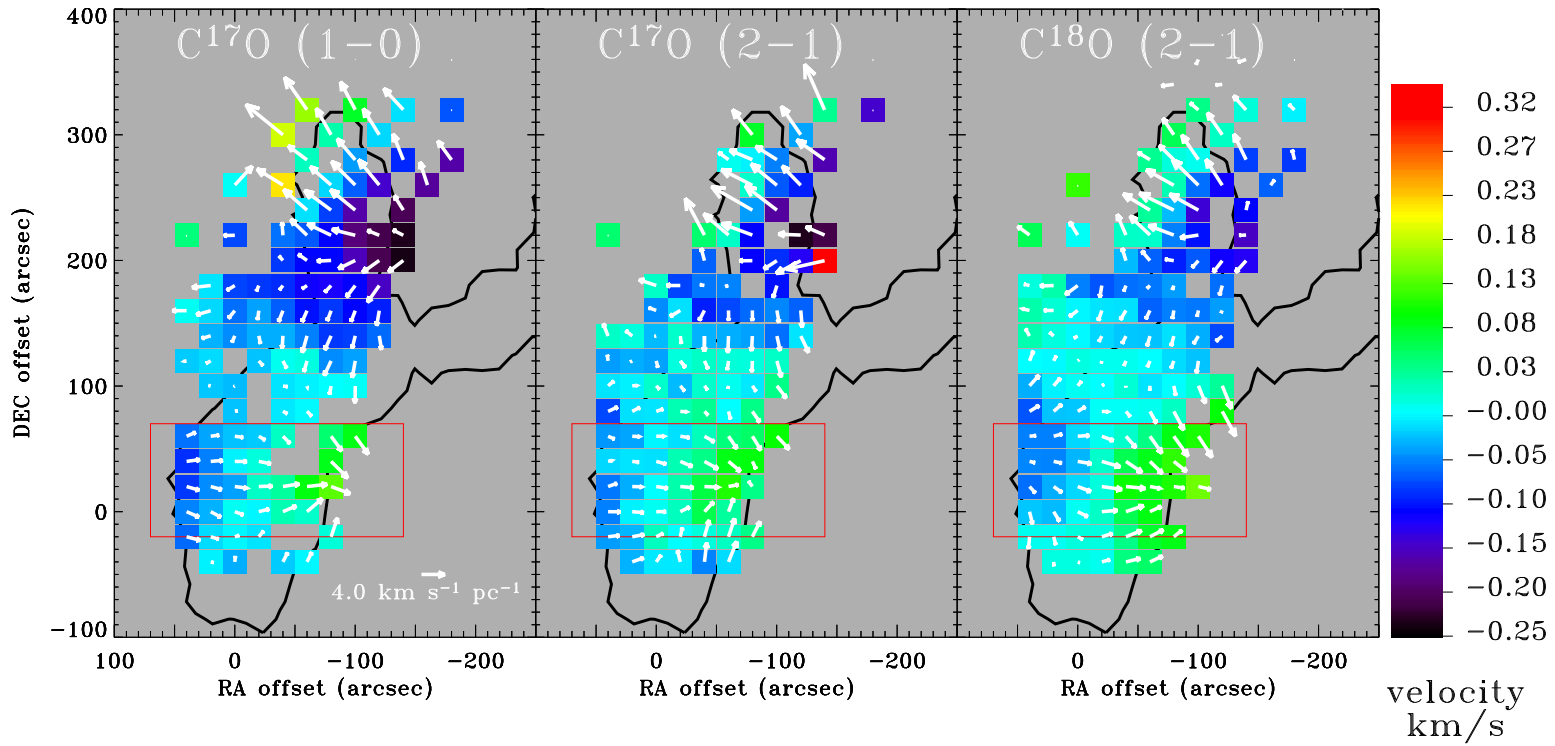


Figure 6.8.— The velocity field for $\text{C}^{17}\text{O}(1-0)$, $\text{C}^{17}\text{O}(2-1)$ and $\text{C}^{18}\text{O}(2-1)$. The light grey filled area is the $A_V = 10$ contour, and the arrows show the direction and magnitude of the line-of-sight velocity gradient, pointing from blue to red. The red box encloses a region with a velocity gradient similar to that of rotation. In each map the velocity shown is the difference between the measured VLSR and the velocity at the (0,0) position.

6.4 Summary

Every molecule that we observe (C^{17}O , C^{18}O , C^{34}S , DCO^+ and N_2H^+) shows increasing depletion as A_V increases and T_d decreases. The integrated intensity map of $\text{C}^{18}\text{O}(2-1)$ shows no enhancement towards the dust peak, and $\text{N}_2\text{H}^+(1-0)$ peaks in a ridge around the dust peak. The amount of CO depletion that we observe is similar to that of L1544 and L1521F (Crapsi et al. 2004), and like L1544 and the dark globule B68 there is evidence of N_2H^+ depletion (Caselli et al. 2002b; Bergin et al. 2002).

The line widths in every species are uncorrelated with dust temperature, column density, and distance from the peak of the dust maps. In particular, the $\text{N}_2\text{H}^+(1-0)$ line width is constant across the core, which is consistent with previous NH_3 measurements (Barranco & Goodman 1998), but inconsistent with N_2H^+ and N_2D^+ observations of L1544 and L1521F (Crapsi et al. 2005). The increase in line width with radius seen in C^{18}O and N_2H^+ in B68 is not seen in TMC-1C, and unlike B68, the C^{18}O line width is significantly larger than the N_2H^+ line width throughout TMC-1C (Lada et al. 2003).

The velocity field that we see in TMC-1C is ordered, but does not show the global signs of rotation that were seen in NH_3 observations at arcminute resolution in Goodman et al. (1993). Nevertheless, one portion of TMC-1C does have a velocity field very much like that created by solid body rotation in the tracers $\text{C}^{17}\text{O}(1-0)$, $\text{C}^{17}\text{O}(2-1)$ and $\text{C}^{18}\text{O}(2-1)$.

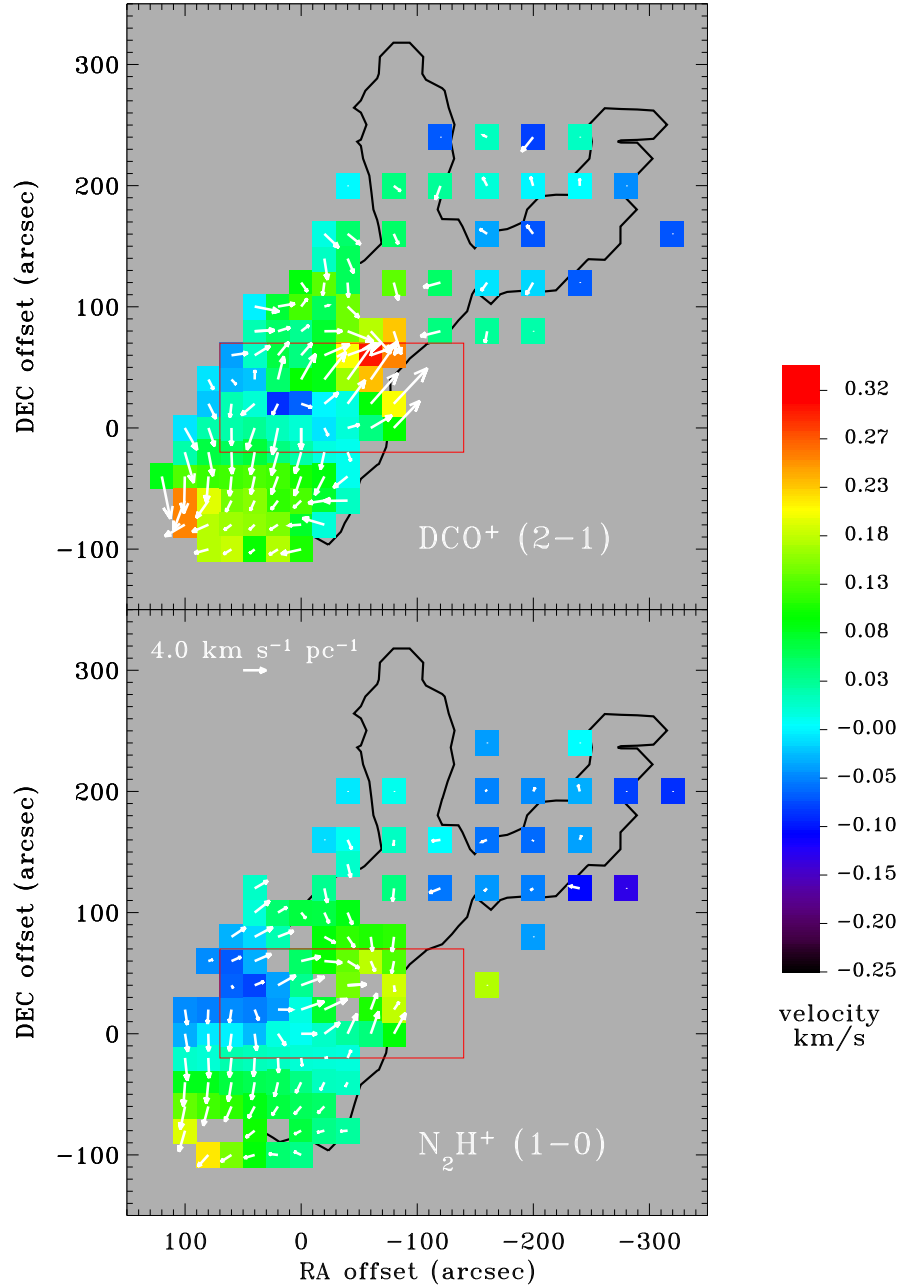


Figure 6.9.— The velocity field for $\text{DCO}^+(2-1)$ and $\text{N}_2\text{H}^+(1-0)$ in TMC-1C. The light grey filled area is the $A_V = 10$ contour, and the arrows show the direction and magnitude of the line-of-sight velocity gradient, pointing from blue to red. The red box encloses a region with a velocity gradient in isotopologues of CO that looks similar to that of rotation, but looks quite dissimilar in DCO^+ and N_2H^+ . In each map the velocity shown is the difference between the measured VLSR and the velocity at the (0,0) position.

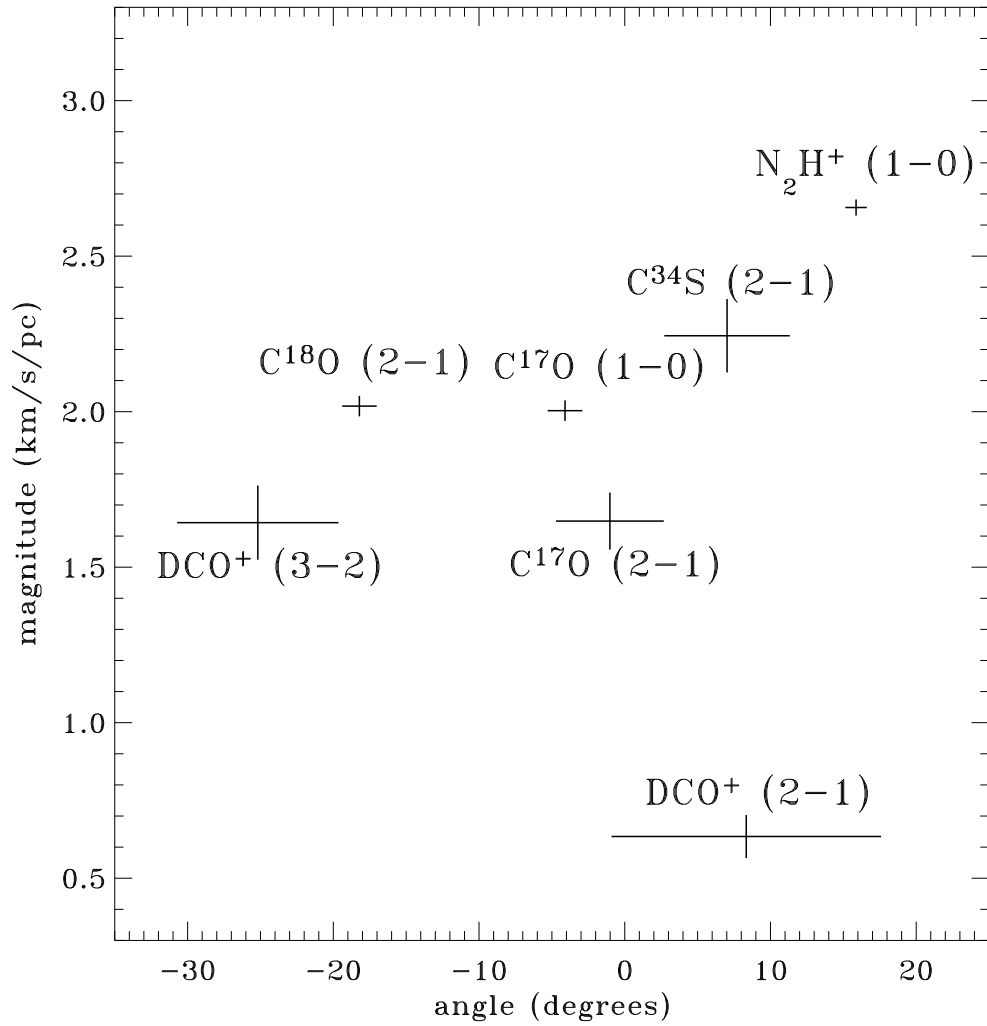


Figure 6.10.— The overall velocity gradient (direction North of East and magnitude) for each tracer in the region bounded by $-140 < \text{RA}_{\text{offset}} < 70$ and $-20 < \text{DEC}_{\text{offset}} < 70$.

Chapter 7

Conclusions

7.1 Summary

In this thesis we have described multi-wavelength analyses of nearby molecular clouds and a starless core. In the spirit of the COMPLETE Survey of Star Forming Regions, it is the coordinated aspect of our observations that allow us to better understand these objects.

In Chapter 2 we combined far-infrared observations of the emission from dust with near-infrared and optical extinction maps to determine the dust column density and temperature. Previous work in this field has not benefitted from having extinction maps covering the entirety of molecular clouds, and the fortuitous release of improved reprocessing of the IRAS all-sky maps has allowed us to make important contributions to the general body of knowledge of dust in molecular clouds. We have shown that the conversion from $100\ \mu\text{m}$ optical depth to A_V varies by roughly a factor of two between the Perseus, Ophiuchus and Serpens molecular clouds. Even within Perseus we see variations of the conversion factor on the order of 10%.

In Chapter 3 we show that most of the scatter that we see between IRAS emission-derived column density and near-infrared absorption-derived column density can be attributed to the necessary, but false, assumption that all of the dust along each line of sight through molecular clouds can be characterized by a single temperature. The effect of the isothermal dust assumption becomes less significant as one observes at longer wavelengths. Because most of the scatter in the two methods of determining column density in Perseus can be explained by the assumption of isothermal dust, we suggest that dust emission properties and the percentage of $60\ \mu\text{m}$ emission coming from stochastically heated very small

dust grains (VSG's) must be relatively constant throughout the molecular cloud. In Ophiuchus, the isothermal dust assumption alone is insufficient to explain the observed scatter between emission-derived column density and absorption-derived column density.

For those astronomers who think of dust only as a screen through which the objects they are interested in studying must be observed, our work implies that estimating the reddening and dimming effects of dust in molecular clouds on the light emitted from background objects from far-infrared emission maps is dicey at best. Although longer wavelength emission maps are less biased by variations in temperature along the line of sight, these maps have lower resolution than their shorter wavelength counterparts. Systematic variations in the conversion between far-infrared optical depth to reddening and extinction will also complicate studies of objects behind molecular clouds.

For those interested in the structure of molecular clouds, our results present a different set of complexities to be dealt with. For instance, if dust emission and/or absorption properties change between and within molecular clouds, then how can one derive dust temperatures, column densities and cloud masses? Furthermore, in Chapter 2 we showed that we can derive reasonable column densities and dust temperatures from IRAS emission maps that globally agree with near-infrared extinction maps and the dust temperature maps of Schlegel et al. (1998) by assuming that for each molecular cloud a constant fraction of the $60\ \mu\text{m}$ flux can be attributed to VSG's. That this should be a reasonable assumption for extinctions ranging between $0.2 < A_V < 10$ implies that VSG's are heated (and therefore not effectively shielded) even in regions of relatively high extinction. It seems likely that the three dimensional structure of molecular clouds is quite porous and has a complicated line-of-sight temperature gradient (Schnee et al. 2006a; Myers & Khersonsky 1995).

Chapters 4, 5 and 6 describe our observations of the starless core TMC-1C in both the continuum and in spectral lines. Our original goal was to determine the velocity field of TMC-1C to check previous, lower resolution, results suggesting that it exhibits solid body rotation. However, it quickly became apparent that because of depletion and self-absorption, the spectral line data needed to be put in context with the results from dust emission. Using only our measurements of the $\text{N}_2\text{H}^+(1-0)$ line and continuum maps at 450 and $850\ \mu\text{m}$, we began our analysis of the core, bringing up several important points. Because we had high S/N observations at two wavelengths, we were able to show that TMC-1C is colder than many starless cores are assumed to be, though the temperature profile actually agrees remarkably well with predictions from numerical models (Stamatellos et al. 2004; Evans et al. 2001; Zucconi et al. 2001). The low derived dust temperature implies a mass that is

several times higher than we would have guessed from just our 850 μm map and the common assumption of isothermality throughout the core. The mass that we derived is significantly higher than the N_2H^+ -derived virial mass, suggesting that TMC-1C should be unstable to collapse. The $\text{N}_2\text{H}^+(1-0)$ line profiles are consistent with sub-sonic infall, in nice agreement with our virial mass argument. By combining the density profile derived from dust emission with the infall speed derived from spectral line data, we show that TMC-1C can be successfully modelled as a contracting Bonnor-Ebert sphere, and that it can not be modelled as well by other popular star formation scenarios.

One source of uncertainty in our first analysis of TMC-1C was the unknown emissivity spectral index, which characterizes the deviation of the dust emission spectrum from that of a blackbody. In Chapter 4 we suggested that by observing TMC-1C at a third wavelength, we could use our three emission maps to solve simultaneously for the dust temperature, emissivity spectral index, and column density. Through a stroke of good fortune, TMC-1C was one of the isolated cores observed at 1200 μm as part of the Spitzer Legacy Project “From Molecular Cores to Planet Forming Disks” (c2d), and we were able to collaborate with members of the c2d team to combine our bolometer data with theirs. In Chapter 5, we show that even the best signal to noise data currently available make deriving maps of three dust parameters from observations at three wavelengths impractical. Instead, we derive a single, constant, value of the emissivity spectral index for TMC-1C and re-derive the temperature and density profiles originally presented in Chapter 4. In addition, we predict that with a fourth emission map, for instance at 350 μm , we could construct an accurate emissivity spectral index map of TMC-1C with currently achievable levels of noise.

Using our dust temperature and column density maps, along with spectral line maps of TMC-1C in a variety of high and low-density tracers, we are finally able to return to our original project. In Chapter 6, we show that every molecule observed is depleted, and that the amount of depletion is correlated with column density and anti-correlated with dust temperature. Although neither result is unexpected, our depletion maps show a clearer gradient in the depletion than any other starless core. The velocity field that we observe is very similar from tracer to tracer, suggesting that depletion is not significantly affecting the observed line-of-sight velocities. However, we do not see evidence of simple solid body or differential rotation, although the velocity field is obviously ordered.

7.2 Future Work

Our study of the far-infrared emission from dust in molecular clouds has suffered from the lack of high-resolution data above $\sim 100 \mu\text{m}$, where the emission is expected to be entirely from large dust grains in thermal equilibrium. We have already begun a new analysis using the recently released $160 \mu\text{m}$ maps of five nearby star-forming regions constructed by c2d using the Spitzer Space Telescope, and in the future we hope to incorporate the ASTRO-F all-sky maps. Using these maps and comparing the observations with models, we hope to better constrain the amount of scatter between emission-derived and absorption-derived column density that comes from the assumption of isothermal dust along the line of sight, and the amount that can be attributed to variable dust emission and absorption properties.

We hope to follow up on the emission from VSG's as a function of A_V using observations in the far-infrared, shortward of $100 \mu\text{m}$, by both Spitzer and ASTRO-F in order to constrain the degree of porosity of molecular clouds. These observations, coupled with numerical simulations, may allow us to determine aspects of the three dimensional structure of molecular clouds.

Using the COMPLETE ^{13}CO maps, we intend to derive an optimal method for turning CO emission into column density maps. Our study will be an improvement over those done in the past in terms of resolution of the CO data, coverage of the CO data, and the ability to correlate the data with the near-infrared extinction maps also generated by COMPLETE.

Mapping TMC-1C at $350 \mu\text{m}$ with SHARC-II at the CSO, mentioned in Chapter 5, would allow us to make independent maps of the dust temperature, emissivity spectral index and column density. In order to better understand the dust emission properties of starless cores, it would be very useful to survey a larger number of objects in nearby molecular clouds to see how β varies within and between cores. Such a survey could take advantage of the new bolometers on APEX and the JCMT, and would also benefit from those on the CSO and the IRAM 30m.

References

- Abergel, A., Boulanger, F., Mizuno, A., & Fukui, Y. 1994, *ApJ*, 423, L59
- Agladze, N. I., Sievers, A. J., Jones, S. A., Burlitch, J. M., & Beckwith, S. V. W. 1996, *ApJ*, 462, 1026
- Alves, J. F., Lada, C. J., & Lada, E. A. 2001, *Nature*, 409, 159
- Andersson, B.-G., Wannier, P. G., Moriarty-Schieven, G. H., & Bakker, E. J. 2000, *AJ*, 119, 1325
- Andre, P., Ward-Thompson, D., & Motte, F. 1996, *A&A*, 314, 625
- Arce, H. G. & Goodman, A. A. 1999a, *ApJ*, 517, 264
- . 1999b, *ApJ*, 512, L135
- Barranco, J. A. & Goodman, A. A. 1998, *ApJ*, 504, 207
- Basu, S. & Mouschovias, T. C. 1994, *ApJ*, 432, 720
- Beckwith, S. V. W. & Sargent, A. I. 1991, *ApJ*, 381, 250
- Belloche, A. & André, P. 2004, *A&A*, 419, L35
- Belloche, A., André, P., Despois, D., & Blinder, S. 2002, *A&A*, 393, 927
- Benson, P. J., Caselli, P., & Myers, P. C. 1998, *ApJ*, 506, 743
- Bergin, E. A., Alves, J., Huard, T., & Lada, C. J. 2002, *ApJ*, 570, L101
- Bernard, J. P., Boulanger, F., & Puget, J. L. 1993, *A&A*, 277, 609
- Bertoldi, F. & McKee, C. F. 1992, *ApJ*, 395, 140
- Bethell, T. J., Zweibel, E. G., Heitsch, F., & Mathis, J. S. 2004, *ApJ*, 610, 801

- Bianchi, S., Davies, J. I., Alton, P. B., Gerin, M., & Casoli, F. 2000, *A&A*, 353, L13
- Bianchi, S., Gonçalves, J., Albrecht, M., Caselli, P., Chini, R., Galli, D., & Walmsley, M. 2003, *A&A*, 399, L43
- Bohlin, R. C., Savage, B. D., & Drake, J. F. 1978, *ApJ*, 224, 132
- Bonnor, W. B. 1956, *MNRAS*, 116, 351
- Boss, A. P. & Myhill, E. A. 1995, *ApJ*, 451, 218
- Boulanger, F., Bronfman, L., Dame, T. M., & Thaddeus, P. 1998, *A&A*, 332, 273
- Burstein, D. & Heiles, C. 1978, *ApJ*, 225, 40
- Cambrésy, L. 1999, *A&A*, 345, 965
- Cambrésy, L., Boulanger, F., Lagache, G., & Stepnik, B. 2001, *A&A*, 375, 999
- Cambrésy, L., Jarrett, T. H., & Beichman, C. A. 2005, *A&A*, 435, 131
- Caselli, P., Benson, P. J., Myers, P. C., & Tafalla, M. 2002a, *ApJ*, 572, 238
- Caselli, P., Myers, P. C., & Thaddeus, P. 1995, *ApJ*, 455, L77+
- Caselli, P., Walmsley, C. M., Tafalla, M., Dore, L., & Myers, P. C. 1999, *ApJ*, 523, L165
- Caselli, P., Walmsley, C. M., Zucconi, A., Tafalla, M., Dore, L., & Myers, P. C. 2002b, *ApJ*, 565, 331
- . 2002c, *ApJ*, 565, 344
- Ciolek, G. E. & Mouschovias, T. C. 1994, *ApJ*, 425, 142
- Crapsi, A., Caselli, P., Walmsley, C. M., Myers, P. C., Tafalla, M., Lee, C. W., & Bourke, T. L. 2005, *ApJ*, 619, 379
- Crapsi, A., Caselli, P., Walmsley, C. M., Tafalla, M., Lee, C. W., Bourke, T. L., & Myers, P. C. 2004, *A&A*, 420, 957
- Crutcher, R. M., Mouschovias, T. C., Troland, T. H., & Ciolek, G. E. 1994, *ApJ*, 427, 839

- David, L. P., Nulsen, P. E. J., McNamara, B. R., Forman, W., Jones, C., Ponman, T., Robertson, B., & Wise, M. 2001, *ApJ*, 557, 546
- del Burgo, C., Laureijs, R. J., Ábrahám, P., & Kiss, C. 2003, *MNRAS*, 346, 403
- Desert, F.-X., Boulanger, F., & Puget, J. L. 1990, *A&A*, 237, 215
- Di Francesco, J., Myers, P. C., Wilner, D. J., Ohashi, N., & Mardones, D. 2001, *ApJ*, 562, 770
- di G. Sigalotti, L. & Klapp, J. 1996, *MNRAS*, 281, 449
- Draine, B. T. 2003, *ARA&A*, 41, 241
- Draine, B. T. & Lee, H. M. 1984, *ApJ*, 285, 89
- Dupac, X., Bernard, J.-P., Boudet, N., Giard, M., Lamarre, J.-M., Mény, C., Pajot, F., Ristorcelli, I., Serra, G., Stepnik, B., & Torre, J.-P. 2003, *A&A*, 404, L11
- Dupac, X., Giard, M., Bernard, J.-P., Boudet, N., Lamarre, J.-M., Mény, C., Pajot, F., Pointecouteau, É., Ristorcelli, I., Serra, G., Stepnik, B., & Torre, J.-P. 2002, *A&A*, 392, 691
- Dupac, X., Giard, M., Bernard, J.-P., Lamarre, J.-M., Mény, C., Pajot, F., Ristorcelli, I., Serra, G., & Torre, J.-P. 2001, *ApJ*, 553, 604
- Ebert, R. 1955, *Zeitschrift fur Astrophysik*, 37, 217
- Emerson, D. T. 1995, in *ASP Conf. Ser. 75: Multi-Feed Systems for Radio Telescopes*, ed. D. T. Emerson & J. M. Payne, 309–+
- Enoch, M. L., Young, K. E., Glenn, J., Evans, II, N. J., Golwala, S., Sargent, A. I., Harvey, P., Aguirre, J., Goldin, A., Haig, D., Huard, T. L., Lange, A., Laurent, G., Maloney, P., Maukopf, P., Rossinot, P., & Sayers, J. 2006, *ApJ*, 638, 293
- Evans, II, N. J., Allen, L. E., Blake, G. A., Boogert, A. C. A., Bourke, T., Harvey, P. M., Kessler, J. E., Koerner, D. W., Lee, C. W., Mundy, L. G., Myers, P. C., Padgett, D. L., Pontoppidan, K., Sargent, A. I., Stapelfeldt, K. R., van Dishoeck, E. F., Young, C. H., & Young, K. E. 2003, *PASP*, 115, 965

- Evans, II, N. J., Rawlings, J. M. C., Shirley, Y. L., & Mundy, L. G. 2001, *ApJ*, 557, 193
- Fiedler, R., Pauls, T., Johnston, K. J., & Dennison, B. 1994, *ApJ*, 430, 595
- Foster, P. N. & Chevalier, R. A. 1993, *ApJ*, 416, 303
- Galli, D., Walmsley, M., & Gonçalves, J. 2002, *A&A*, 394, 275
- Goldsmith, P. F., Bergin, E. A., & Lis, D. C. 1997, *ApJ*, 491, 615
- Gonçalves, J., Galli, D., & Walmsley, M. 2004, *A&A*, 415, 617
- Goodman, A. A. 2004, in *ASP Conf. Ser. 323: Star Formation in the Interstellar Medium: In Honor of David Hollenbach*, ed. D. Johnstone, F. C. Adams, D. N. C. Lin, D. A. Neufeld, & E. C. Ostriker, 171–+
- Goodman, A. A., Barranco, J. A., Wilner, D. J., & Heyer, M. H. 1998, *ApJ*, 504, 223
- Goodman, A. A., Benson, P. J., Fuller, G. A., & Myers, P. C. 1993, *ApJ*, 406, 528
- Gottlieb, C. A., Myers, P. C., & Thaddeus, P. 2003, *ApJ*, 588, 655
- Harvey, D. W. A., Wilner, D. J., Lada, C. J., Myers, P. C., Alves, J. F., & Chen, H. 2001, *ApJ*, 563, 903
- Heitsch, F., Zweibel, E. G., Mac Low, M.-M., Li, P., & Norman, M. L. 2001, *ApJ*, 561, 800
- Henning, T., Michel, B., & Stognienko, R. 1995, *Planet. Space Sci.*, 43, 1333
- Hildebrand, R. H. 1983, *QJRAS*, 24, 267
- Holland, W. S., Robson, E. I., Gear, W. K., Cunningham, C. R., Lightfoot, J. F., Jenness, T., Ivison, R. J., Stevens, J. A., Ade, P. A. R., Griffin, M. J., Duncan, W. D., Murphy, J. A., & Naylor, D. A. 1999, *MNRAS*, 303, 659
- Jarrett, T. H., Dickman, R. L., & Herbst, W. 1989, *ApJ*, 345, 881
- Jenness, T. & Lightfoot, J. F. 1998, in *ASP Conf. Ser. 145: Astronomical Data Analysis Software and Systems VII*, ed. R. Albrecht, R. N. Hook, & H. A. Bushouse, 216–+
- Johnstone, D., Di Francesco, J., & Kirk, H. 2004, *ApJ*, 611, L45

- Johnstone, D., Fich, M., Mitchell, G. F., & Moriarty-Schieven, G. 2001, *ApJ*, 559, 307
- Johnstone, D., Wilson, C. D., Moriarty-Schieven, G., Joncas, G., Smith, G., Gregersen, E., & Fich, M. 2000, *ApJ*, 545, 327
- Jones, T. J., Hyland, A. R., & Bailey, J. 1984, *ApJ*, 282, 675
- Kenyon, S. J., Dobrzycka, D., & Hartmann, L. 1994, *AJ*, 108, 1872
- Kramer, C., Alves, J., Lada, C. J., Lada, E. A., Sievers, A., Ungerechts, H., & Walmsley, C. M. 1999, *A&A*, 342, 257
- Kramer, C., Richer, J., Mookerjee, B., Alves, J., & Lada, C. 2003, *A&A*, 399, 1073
- Kreysa, E., Gemünd, H.-P., Gromke, J., Haslam, C. G. T., Reichertz, L., Haller, E. E., Beeman, J. W., Hansen, V., Sievers, A., & Zylka, R. 1999, *Infrared Physics and Technology*, 40, 191
- Lada, C. J., Alves, J., & Lada, E. A. 1999, *ApJ*, 512, 250
- Lada, C. J., Bergin, E. A., Alves, J. F., & Huard, T. L. 2003, *ApJ*, 586, 286
- Lada, C. J., Lada, E. A., Clemens, D. P., & Bally, J. 1994, *ApJ*, 429, 694
- Lagache, G., Abergel, A., Boulanger, F., & Puget, J.-L. 1998, *A&A*, 333, 709
- Langer, W. D., Wilson, R. W., Goldsmith, P. F., & Beichman, C. A. 1989, *ApJ*, 337, 355
- Laureijs, R. J., Clark, F. O., & Prusti, T. 1991, *ApJ*, 372, 185
- Lee, C. W., Myers, P. C., & Plume, R. 2004, *ApJS*, 153, 523
- Lee, C. W., Myers, P. C., & Tafalla, M. 1999, *ApJ*, 526, 788
- . 2001, *ApJS*, 136, 703
- Lee, J.-E., Evans, II, N. J., Shirley, Y. L., & Tatematsu, K. 2003, *ApJ*, 583, 789
- Li, A. & Draine, B. T. 2001, *ApJ*, 550, L213
- Lombardi, M. & Alves, J. 2001, *A&A*, 377, 1023
- Mannings, V. & Emerson, J. P. 1994, *MNRAS*, 267, 361

- Mathieu, R. D., Adams, F. C., Fuller, G. A., Jensen, E. L. N., Koerner, D. W., & Sargent, A. I. 1995, *AJ*, 109, 2655
- Mathis, J. S. 1990, *ARA&A*, 28, 37
- Mathis, J. S., Mezger, P. G., & Panagia, N. 1983, *A&A*, 128, 212
- Mathis, J. S., Rumpl, W., & Nordsieck, K. H. 1977, *ApJ*, 217, 425
- McCall, M. L. 2004, *AJ*, 128, 2144
- McLaughlin, D. E. & Pudritz, R. E. 1996, *ApJ*, 469, 194
- Mennella, V., Brucato, J. R., Colangeli, L., Palumbo, P., Rotundi, A., & Bussoletti, E. 1998, *ApJ*, 496, 1058
- Mitchell, G. F., Johnstone, D., Moriarty-Schieven, G., Fich, M., & Tothill, N. F. H. 2001, *ApJ*, 556, 215
- Miville-Deschênes, M.-A. & Lagache, G. 2005, *ApJS*, 157, 302
- Monet, D. 1996, *Bulletin of the American Astronomical Society*, 28, 905
- Myers, P. C., Fuller, G. A., Goodman, A. A., & Benson, P. J. 1991, *ApJ*, 376, 561
- Myers, P. C. & Goodman, A. A. 1988a, *ApJ*, 326, L27
- . 1988b, *ApJ*, 329, 392
- Myers, P. C. & Khersonsky, V. K. 1995, *ApJ*, 442, 186
- Myers, P. C., Mardones, D., Tafalla, M., Williams, J. P., & Wilner, D. J. 1996, *ApJ*, 465, L133+
- Nagata, H., Shibai, H., Takeuchi, T. T., & Onaka, T. 2002, *PASJ*, 54, 695
- Nelder, J. & Mead, R. 1965, *Computer Journal*, 7, 308
- Ossenkopf, V. & Henning, T. 1994, *A&A*, 291, 943
- Pagani, L., Bacmann, A., Motte, F., Cambr sy, L., Fich, M., Lagache, G., Miville-Desch nes, M.-A., Pardo, J.-R., & Apponi, A. J. 2004, *A&A*, 417, 605
- Pauls, T. & Schwartz, P. R. 1989, *LNP Vol. 331: The Physics and Chemistry of Interstellar Molecular Clouds - mm and Sub-mm Observations in Astrophysics*, 331, 225

- Penzias, A. A. 1981, *ApJ*, 249, 518
- Pierce-Price, D., Richer, J. S., Greaves, J. S., Holland, W. S., Jenness, T., Lasenby, A. N., White, G. J., Matthews, H. E., Ward-Thompson, D., Dent, W. R. F., Zylka, R., Mezger, P., Hasegawa, T., Oka, T., Omont, A., & Gilmore, G. 2000, *ApJ*, 545, L121
- Preibisch, T., Ossenkopf, V., Yorke, H. W., & Henning, T. 1993, *A&A*, 279, 577
- Reid, M. A. & Wilson, C. D. 2005, *ApJ*, 625, 891
- Ridge, N., Schnee, S., Goodman, A., & Foster, J. 2006a, *ApJ*, 643, 932
- Ridge, N. A., Di Francesco, J., Kirk, H., Li, D., Goodman, A. A., Alves, J. F., Arce, H. G., Borkin, M. A., Caselli, P., Foster, J. B., Heyer, M. H., Johnstone, D., Kosslyn, D. A., Lombardi, M., Pineda, J. E., Schnee, S. L., & Tafalla, M. 2006b, *AJ*, 131, 2921
- Safier, P. N., McKee, C. F., & Stahler, S. W. 1997, *ApJ*, 485, 660
- Schlegel, D. J., Finkbeiner, D. P., & Davis, M. 1998, *ApJ*, 500, 525
- Schnee, S., Bethell, T., & Goodman, A. 2006a, *ApJ*, 640, L47
- Schnee, S., Caselli, P., Goodman, A., Arce, H., Barranco, J., Ballesteros-Paredes, J., & Kuchibhotla, K. 2006b, *ApJ*, to be submitted
- Schnee, S. & Goodman, A. 2005, *ApJ*, 624, 254
- Schnee, S., Kauffmann, J., Goodman, A., & Bertoldi, F. 2006c, *ApJ*, submitted
- Schnee, S. L., Ridge, N. A., Goodman, A. A., & Li, J. G. 2005, *ApJ*, 634, 442
- Schöier, F. L., van der Tak, F. F. S., van Dishoeck, E. F., & Black, J. H. 2005, *A&A*, 432, 369
- Shirley, Y. L., Evans, II, N. J., Rawlings, J. M. C., & Gregersen, E. M. 2000, *ApJS*, 131, 249
- Shu, F. H. 1977, *ApJ*, 214, 488
- Stamatellos, D., Whitworth, A. P., André, P., & Ward-Thompson, D. 2004, *A&A*, 420, 1009

- Stepnik, B., Abergel, A., Bernard, J.-P., Boulanger, F., Cambr sy, L., Giard, M., Jones, A. P., Lagache, G., Lamarre, J.-M., Meny, C., Pajot, F., Le Peintre, F., Ristorcelli, I., Serra, G., & Torre, J.-P. 2003, *A&A*, 398, 551
- Tafalla, M., Mardones, D., Myers, P. C., Caselli, P., Bachiller, R., & Benson, P. J. 1998, *ApJ*, 504, 900
- Tafalla, M., Myers, P. C., Caselli, P., & Walmsley, C. M. 2004, *Ap&SS*, 292, 347
- Tafalla, M., Myers, P. C., Caselli, P., Walmsley, C. M., & Comito, C. 2002, *ApJ*, 569, 815
- Testi, L., Natta, A., Shepherd, D. S., & Wilner, D. J. 2003, *A&A*, 403, 323
- van Dishoeck, E. F., Glassgold, A. E., Guelin, M., Jaffe, D. T., Neufeld, D. A., Tielens, A. G. G. M., & Walmsley, C. M. 1992, in *IAU Symp. 150: Astrochemistry of Cosmic Phenomena*, ed. P. D. Singh, 285–+
- Ward-Thompson, D., Motte, F., & Andre, P. 1999, *MNRAS*, 305, 143
- Ward-Thompson, D., Scott, P. F., Hills, R. E., & Andre, P. 1994, *MNRAS*, 268, 276
- Williams, J. P. & Myers, P. C. 1999, *ApJ*, 511, 208
- Williams, J. P., Myers, P. C., Wilner, D. J., & di Francesco, J. 1999, *ApJ*, 513, L61
- Wilson, T. L. & Rood, R. 1994, *ARA&A*, 32, 191
- Wood, D. O. S., Myers, P. C., & Daugherty, D. A. 1994, *ApJS*, 95, 457
- Zhou, S., Evans, II, N. J., Koempe, C., & Walmsley, C. M. 1993, *ApJ*, 404, 232
- Zucconi, A., Walmsley, C. M., & Galli, D. 2001, *A&A*, 376, 650